UNIVERSITY OF CALIFORNIA

Santa Barbara

Laser Spectroscopy and Photodynamics of Alternative Nucleobases and Organic Dyes

A dissertation submitted in partial satisfaction of the

requirements for the degree Doctor of Philosophy

in Chemistry

by

Jacob Alan Berenbeim

Committee in charge:

Professor Mattanjah de Vries, Chair

Professor Steve Buratto

Professor Michael Gordon

Professor Martin Moskovits

December 2017

The dissertation of Jacob Alan Berenbeim is approved.

_____

Steve Buratto

_____

Michael Gordon

_____

Martin Moskovits

_____

Mattanjah de Vries, Committee Chair

October 2017

Laser Spectroscopy and Photodynamics of Alternative Nucleobases and Organic Dyes

by

Jacob Alan Berenbeim

ACKNOWLEDGEMENTS

To my wife Amy thank you for your endless support and for inspiring me to match your own relentless drive towards reaching our goals. To my parents and my brothers Eli and Gabe thank you for your love and visits to Santa Barbara, CA. To my advisor Mattanjah and my lab mates thank you for the incredible opportunity to share ideas and play puppets with the fabric of space. And to my cat Lola, you're a good cat.

VITA OF JACOB ALAN BERENBEIM
October 2017

EDUCATION

University of California, Santa Barbara CA — Fall 2017
PhD, Physical Chemistry
Advisor: Prof. Mattanjah S. de Vries

University of Puget Sound, Tacoma WA — 2009
BS, Chemistry
Advisor: Prof. Daniel Burgard

LABORATORY TECHNIQUES

Photophysics by UV/VIS and IR pulsed laser spectroscopy, optical alignment, oa-TOF mass spectrometry (multiphoton ionization, MALDI, ESI+), molecular beam high vacuum apparatus, high voltage electronics, molecular computational modeling with Gaussian, data acquisition with LabView, and data manipulation with Mathematica and Origin

RESEARCH EXPERIENCE

Graduate Student Researcher — 2012-2017
- Time dependent (transient) photo relaxation of organic molecules, including PAHs and aromatic biological molecules.
- Molecular beam action spectroscopy with TOF detection and laser desorption laser ionization.
- Developed thermal AFM desorption technique as a mass transport technique with sub-micron crater resolution.
- Forensic bio-marker analysis in Archaeometry.
- Extensive maintenance of homebuilt and commercial laboratory equipment: pulsed lasers, high vacuum systems, molecular beam time-of-flight ms, HV power supplies, digital and analogue timing devices.
- Computational modeling with Gaussian software and LabView, Mathmatica, Origin, and Excel software experience.

Undergraduate Student Researcher — 2008-2009
- Spectroscopic remote sensing of marine vessel gaseous emissions.

PROFESSIONAL EXPERIENCE

Mass Spectrometry Facility Assistant, University of California, Santa Babara — 2017
- Maintenance, training, and operating user facility which includes GC/MS, MALDI, and electrospray oa-TOF.

GC Analyst, Accutest Laboratories, Denver, CO — 2010-2011
- GC and GC/MS analysis of waste water, dissolved gases, and soil extracts.

PUBLICATIONS

1. **Berenbeim, J.A.**, Boldissar, S., Owens, S., Haggmart, M., Gate, G., Schmidt Patterson, C.M., de Vries, M.S., "Molecular Mechanisms of the Photostability of Common Madder Chromophores Alizarin and Purpurin and Hydroxy-Substituted Anthraquinones" (Manuscript in Preparation)

2. **Berenbeim, J.A.**, Siouri, F., Boldissar, S., Gate, G., Haggmark, M., Aboulache, B., Cohen, T., de Vries, M.S., "Excited State Dynamics of Isocytosine; a Hybrid Case of Canonical Nucleobase Photodynamics" J. Phys. Chem. Lett. 2017

3. Siouri, F., Boldissar, S., **Berenbeim, J.A.**, de Vries, M.S., "Excited State Dynamics of 6-Thioguanine" J. Phys. Chem. 2017.

4. Owens, S., **Berenbeim, J.A.**, Ligare, M., Gulian, L., Siouri, F., Boldissar, S., Tyson-Smith, S., Wilson, G., Ford, A., De Vries, M.S., "Direct Analysis of Xanthine Stimulants in Archaeological Vessels by laser desorption REMPI" Anal. Chem. 2017.

5. Owens, S. C., **Berenbeim, J. A.**, Patterson, C. S., Dillon, E. P., de Vries, M.S., "Sub-Micron Proximal Probe Thermal Desorption and Laser Mass Spectrometry on Painting Cross-Sections." Anal. Methods, 2014

6. Burgard, D. A., Bria, C.R.M., **Berenbeim, J. A.**, "Remote Sensing of Emissions from In-Use Small Engine Marine Vessels." Environ. Sci. Technol. 2011, 45, 2894-2901.

RECENT PRESENTATIONS AND POSTER SESSIONS

1. **Berenbeim, J.A.**, Boldissar, S., Owens, S., Schmidt Patterson, C.M., de Vries, M.S., "Please No Flash Photography or: How Come Our Red Pigments Are Fading?" poster presented at the 2017 Gaseous Ions GRS and GRC, Ventura, CA 2017

2. **Berenbeim, J.A.**, "Molecular Mechanisms of the Photostability of Natural Red Dyes" oral presentation Chemical Sciences Student Seminar, UCSB, Santa Barbara, CA 2016

3. **Berenbeim, J.A.**, Owens, S., Siouri, F., Boldissar, S., Dillion, E., Brauer, J., Schmidt Patterson, C.M., de Vries, M.S., "AFM-Sampling-L2MS on Painting Cross-Sections" poster presented at the 251st ACS National Meeting, San Diego, CA 2016

4. Owens, S., **Berenbeim, J.A.**, "A Study of Painting Cross-Sections by Nanometer-Scale Proximal Probe Thermal Desorption Coupled with Laser Mass Spectrometry" poster presented at the GRC - Scientific Methods in Cultural Heritage Research. Newry, ME 2014

FELLOWSHIPS

Partnership in International Research & Education on Electron Chemistry & Catalysis at Interfaces (NSF PIRE-ECCI) Fellowship Recipient under host Prof. Xueming Yang at the Dalian Institute of Chemical Physics, Dalian, China 2014-2015

ABSTRACT

Laser Spectroscopy and Photodynamics of Alternative Nucleobases and Organic Dyes

by

Jacob Alan Berenbeim

Herein I've compiled the published work and laboratory-operation notes done on organic chromophore's interaction with and characterization by laser light. All experimental work is performed by resonant excitation multiphoton ionization (REMPI) on cold, neutral, and isolated molecules in a molecular beam. REMPI is a spectroscopic technique which allows us to probe a coherent population of structurally specific molecules and to probe their dynamic response to electronic stimulation. Our primary concern is whether a correlation between molecular form (nucleobases and derivatives absorbing UV light) or function (dye molecules absorbing visible light) exists with the energetic descent pathway(s) taken after irradiation. These experiments aim to be absolutely reproducible with respect to sampling the excited state population in time (Δt) with some absorption energy (ΔE). These relaxation paths are complex and our measurement of them is representative of a probabilistic summation.

The characterization of a molecule by IR radiation is common by today's standards, however, for our molecules (i.e. cold, neutral, and isolated) which are prepared in a molecular beam we are in the position to compare with state of the art computation. This allows for a higher certainty when identifying, and later comparing multiple, forms (e.g.

tautomers, conformers) of a molecule within our beam. This type of analysis is invaluable when differentiating alternative nucleobase structures in the chapters on *Isocytosine* (Chapter 1.1) and *6-thioguanine* (Chapter 1.2). Additionally, I emphasize the opportunity to compare our results with theory because state-of-the-art does not imply accuracy. The ability to measure the effects of intramolecular hydrogen bonding on -OH stretches within different bonding environments such as neighboring a carbonyl or hydroxyl group, or the anti-cooperation of multiple intramolecular hydrogen bonds about a mutual hydrogen bond acceptor, all relative to a free -OH stretch is explored in the *Anthraquinone Dyes* (Chapter 2.1) where the current published level of DFT fails to predict the ground state structure and anharmonic and/or ab initio methods are too costly.

Of great interest is relaxation pathways of a chromophore after photo excitation. The deactivation pathways a molecule takes, be them radiative or non-radiative, have severe implications on the form and function of that molecule. Moreover, these paths are often defined by competing processes which branch and become more complex. Here I continue to expand on the photostability centered hypothesis of prebiotic chemistry; the aromaticity of genetic molecules leave them prone to harsh UV absorption in an ozoneless prebiotic environment, however, a predisposition to convert electronic to ground state vibrational energy (heat) on an ultrafast timescale seems to support the prevalence of our canonical bases A, T, G, C, U. The numerous derivatized or alternative nucleobase alternatives often get trapped in longer lived excited state time windows allowing for reactive chemistry. The work on *isocytosine* (Chapter 1.1) presents us with a possible hybrid nucleobase, exciting both in letting us understand the unique photostability of biological (keto) G and as a possible xeno or pre-RNA/DNA nucleobase due to its ultrafast relaxation. Secondly, *6-*

thioguanine (Chapter 1.2) converts with near unity to a long lived dark state and due to the thio←oxo guanine substitution this intersystem crossing happens at an abnormally high rate. Both *isocytosine* and *6-thioguanine* are attractive to us for their fundamental photo properties, but also to a wider research base due to their biological uptake and therefore prospective use as synthetic bio-monomers and in pharmaceuticals as immunosuppressant's (specifically *6-thioguanine* which as a group of thiopurines and pyrimidines cause secondary cancers, e.g. skin cancer). The work on *anthraquinone dyes* (Chapter 2.1) was an effort to understand the photostability of these molecules within their historically usage in cultural heritage materials. We focus on the most famous and molecularly simple hydroxyanthraquinones, namely alizarin and purpurin. The concern is that even though these select organic dyes are photostable their natural origin is inhomogeneous so their degradation is unpredictable over many years and makes cultural heritage preservation and restoration difficult. I present a case study that can help us predict relative photo stabilities based on a key structural motif. Connecting the dye excited state dynamics with the nucleobase dynamics is a central theme running between these chapters.

Of major importance to all this work was expanding our laboratories dynamic regime to the picosecond which involved ingenuity on the experimental front as well as more complete data fitting of time dependent signal.

Lastly, is a two-part chapter on the application of REMPI to study *meso-american pottery* (Chapter 3.1) and *painting cross sections* (Chapter 3.2). These chapters emphasize the ability to go beyond fundamental research and apply these laser spectroscopic methods to more tangible scientific projects.

TABLE OF CONTENTS

I. Alternative Nucleobases

Of great interest is relaxation pathways of a chromophore after photo excitation. The deactivation pathways a molecule takes, be them radiative or non-radiative, have severe implications on the form and function of that molecule. Moreover, these paths are often defined by competing processes which branch and become more complex. Here I continue to expand on the photostability centered hypothesis of prebiotic chemistry; the aromaticity of genetic molecules leave them prone to harsh UV absorption in an ozoneless prebiotic environment, however, a predisposition to convert electronic to ground state vibrational energy (heat) on an ultrafast timescale seems to support the prevalence of our canonical bases A, T, G, C, U. The numerous derivatized or alternative nucleobase alternatives often get trapped in longer lived excited state time windows allowing for reactive chemistry. The work on *isocytosine* (Chapter 1.1) presents us with a possible hybrid nucleobase, exciting both in letting us understand the unique photostability of biological (keto) G and as a possible xeno or pre-RNA/DNA nucleobase due to its ultrafast relaxation. Secondly, *6-thioguanine* (Chapter 1.2) converts with near unity to a long lived dark state and due to the thio←oxo guanine substitution this intersystem crossing happens at an abnormally high rate. Both *isocytosine* and *6-thioguanine* are attractive to us for their fundamental photo properties, but also to a wider research base due to their biological uptake and therefore prospective use as synthetic bio-monomers and in pharmaceuticals as immunosuppressant's (specifically *6-thioguanine* which as a group of thiopurines and pyrimidines cause secondary cancers, e.g. skin cancer).

I. Excited State Dynamics of Isocytosine; A Hybrid Case of Canonical Nucleobase Photodynamics

Jacob A. Berenbeim, Samuel Boldissar, Faady M. Siouri, Gregory Gate, Michael R. Haggmark, Briana Aboulache, Trevor Cohen, and Mattanjah S. de Vries*

Department of Chemistry and Biochemistry, University of California Santa Barabara, CA 93106-9510

**E-mail:* devries@chem.ucsb.edu

Reprinted with Permission from Berenbeim, J. A.; Boldissar, S.; Siouri, F. M.; Gate, G.; Haggmark, M. R.; Aboulache, B.; Cohen, T.; De Vries, M. S. Excited-State Dynamics Of Isocytosine: A Hybrid Case Of Canonical Nucleobase Photodynamics. *J. Phys. Chem. Lett.* **2017,** *8,* 5184-5189.

Abstract

We present resonant two-photon ionization (R2PI) spectra of isocytosine (isoC) and pump-probe results on two of its tautomers. We compare the excited state dynamics with the Watson Crick (WC) cytosine (C) and guanine (G) tautomeric forms. These results suggest that the excited state dynamics of WC G may primarily depend on the heterocyclic substructure of the pyrimidine moiety, which is chemically identical to isoC. For WC isoC we find a single excited state decay with a rate of ~ 10^{10} s^{-1} while the enol form has multiple decay rates, the fastest of which is 7 times slower than for WC isoC. The excited state dynamics of isoC exhibits striking similarities with that of G, more so than with the photo-dynamics of C.

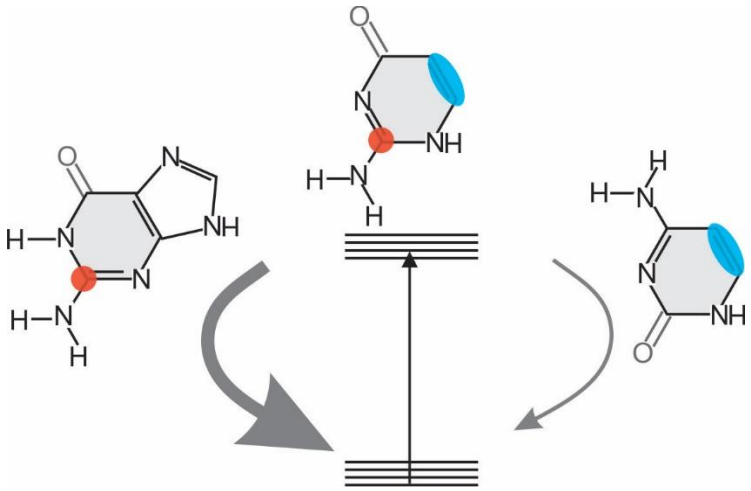

Without a fossil record of the prebiotic chemical world we are left to conjecture to understand the road map that led to RNA and DNA. One of the factors that may have played a role in the prebiotic chemistry on an early earth is the photochemistry that could have been important before modern enzymatic repair and before the formation of the ozone layer.[1-6] Nucleobases, when absorbing ultraviolet (UV) radiation, tend to eliminate the resulting electronic excitation by internal conversion (IC) in picoseconds (ps) or less.[4, 7-9] The availability of this rapid “safe” de-excitation pathway turns out to depend exquisitely on molecular structure. DNA and RNA bases are generally short lived in the excited state, and thus UV protected, while many closely related compounds are long lived and thus more prone to UV damage. This structure dependence suggests a mechanism for the chemical selection of the building blocks of life, implying that photochemical properties may be molecular fossils of the earliest stages of prebiotic chemistry.

It is therefore of great interest to study the photochemical properties of possible alternative bases in comparison to the canonical bases. Especially intriguing are structures

that can form alternate base pairs with the same Watson Crick (WC) motif as the canonical ones, such as the triple hydrogen bonded Guanine/Cytosine (G/C) pair.[10-13] The alternative bases isocytosine (isoC) and isoguanine (isoG) were predicted in 1962 as a plausible third WC base pair.[14] As pointed out by Saladino et al., isoC can form WC base pairs with cytosine (C) and isoguanine or a reversed WC base pair with guanine.[15] Here we focus on isoC, which is not only an isomer of C but also an analogue of guanine (G), see Figure 1. Theoretical and experimental study has established the thermodynamic stability of the isoC/isoG base pair which nominally has greater free energy than G/C as well as of other possible base pair combinations with isoC.[16-17] This has piqued interest in the prebiotic prevalence of these unnatural pairs in addition to their role in synthetic research and medical applications.[18-19] Here we aim to understand the photostability of isoC.

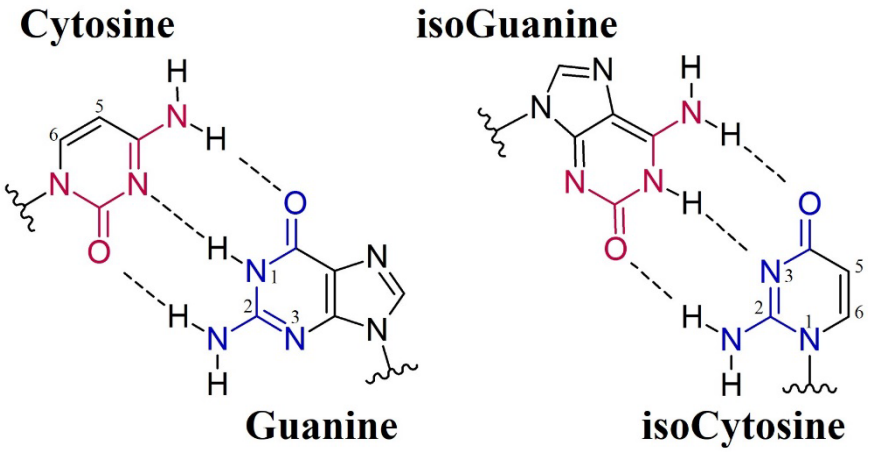

Figure 1: Structures of G/C and isoG/isoC arranged to emphasize heterocyclic substructure similarities, emphasized in red and blue.

We have arranged the bases within Figure 1 to emphasize the functional rearrangement from the standard base to its iso- analog about the pyrimidine heterocyclic centers. Doing so

likens isoC to the core moiety of G. The difference between G and isoC is the five membered ring in G (not present in isoC) which would have consequences for formation of a macromolecular structure. In this work, we find that the excited state dynamics of isoC exhibits striking similarities with that of G and more so than with the photo-dynamics of C.

IsoC has previously been identified in the gas phase[20] and its photo dynamics have been studied theoretically[21-22] and in the condensed phase[23-25] but no excited state lifetime has been experimentally determined of isolated isoC in individual tautomeric forms. The two lowest energy forms are enol and keto which can isomerize via an excited state intramolecular proton transfer. This isomerization after UV excitation has been observed in solution[23] by time dependent absorption spectroscopy and in a rare gas matrix by changes in the IR absorption.[24-25] Chart 1 outlines the lowest energy tautomers in the gas phase. KA2 corresponds to the WC structure in the pairing with isoG in Figure 1. KA1 can also form similar triple hydrogen bonded structures with other tautomeric forms of G, such as the enol form.

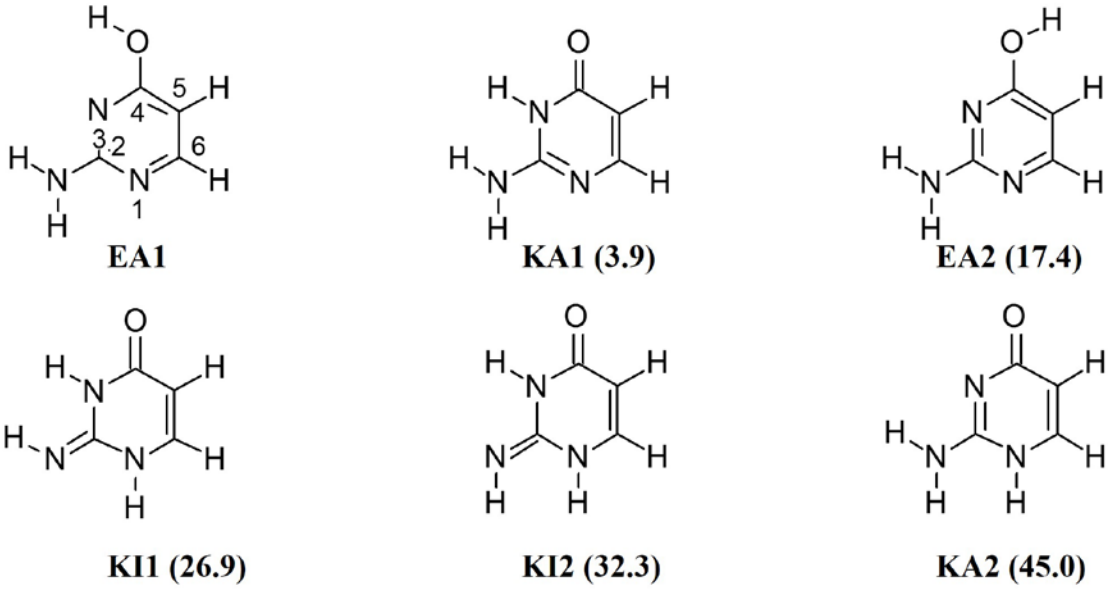

Chart 1: Lowest ground state energy structures (ΔE < 50 kJ/mol). Heterocyclic atoms are numbered for EA1 but the convention is the same for all others. Arranged in order of relative energy given in parenthesis (kJ/mol). Zero point corrected energies were calculated by DFT analysis with the B3LYP hybrid functional and with a cc-pVTZ basis set.

Recent work by Szabla et. al used state-of-the-art surface-hopping adiabatic molecular dynamic simulations to predict the excited states lifetime of isoC to be the following: τ_{EA1}=533 fs and τ_{KA1}=182 fs.[21] These lifetimes are from populating a continuum of mixed character electronic states S1-S6 at the 5.5 ± 0.2 eV spectral domain which proceed to relax through S1 IC. Three dominant conical intersection (CI) geometries are established in their work for the modeled EA1 and KA1 starting structures, whereby pyramidalization of the planar Franck Condon (FC), i.e. excitation geometry, structure at the C2 position accounts for Φ_{EA1}=0.60 and Φ_{KA1}=0.93 non-radiative relaxation yields, while deformation about the C_5=C_6 bond accounts for a CI of negligible yield. Hu et al. also studied the KA1 form computationally, comparing different levels of theory. They assumed excitation at energies closer to the vibrationless level and identified three CIs, all leading to IC to the ground state,

one involving the C=O stretching vibration and two involving out-of-plane structures of the NH_2 group. They found the preferred pathway to depend on the computational method, as did the IC rate, leading to excited state lifetimes ranging from 100 fs to 1 ps.[26] Surprisingly, both computational studies are contrary to the bulk of theoretical work done on pyrimidine relaxation dynamics, where the $CI_{C5=C6}$ is understood to be a major pathway towards nonradiative deactivation by twisting of the H-C_5=C_6-H torsional angle to near ethylene geometry.[27-29] Trachsel et al. most recently showed the importance of this particular bond deformation when they measured excited state lifetimes of 5,6-trimethylenecytosine, a sterically constrained C analogue, in the gas phase.[30] This modified version yielded lifetimes attributed to IC six times greater than that of C, likely due to the absence of a $CI_{C5=C6}$.

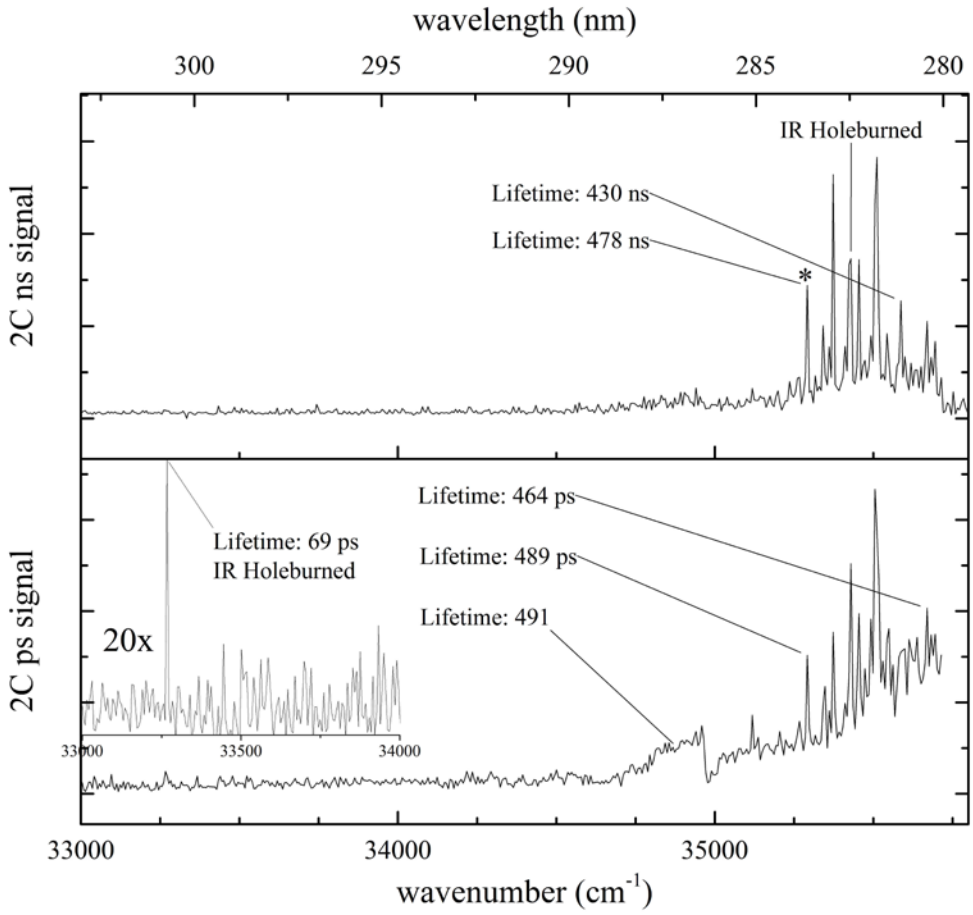

Figure 2: 2C R2PI spectra for isocytosine (a) ns excitation with 193 nm ionization and (b) ps excitation with 213 nm ionization (5th Nd:YAG harmonic). Lifetimes are pump-probe data. See text for details.

Figure 2 shows Two-Color (2C) resonant two-photon ionization (R2PI) spectra of isocytosine with nanosecond (ns) and ps pulse sources. The ns spectrum (Figure 2a) has a well-defined origin transition at 35,292 cm^{-1} (starred *) followed by a series of discrete peaks atop an elevated baseline over a range of 500 cm^{-1}. This elevated baseline extends to the red but is relatively low in intensity and devoid of features. The ps trace (Figure 2b) exhibits the same defined vibronic transitions seen in the ns spectrum but presents another unique feature at 33,266 cm^{-1}. Here, the elevated baseline features to the red of the starred origin are by contrast to the ns spectrum more intense. While this signal could result from

other tautomers, we suspect that this feature is due to hot bands from the low frequency breathing vibrational modes which are more efficiently excited with the 6 cm^{-1} spectral linewidth of ps laser and artificially intensified by elevated laser power in that region. The sharp feature at 35,000 cm^{-1} is a laser power artifact and highlights the non-resonant nature of the absorption in this range. Furthermore, we could not obtain IR-UV double resonant signal from this part of the spectrum, which is also consistent with hot bands. We simultaneously recorded wavelength and mass spectra, shown as a two-dimensional plot in supplemental information (S.1) to verify that there is no contribution to the isoC mass channel from potential higher order clusters, including checking the M+1 mass channel.

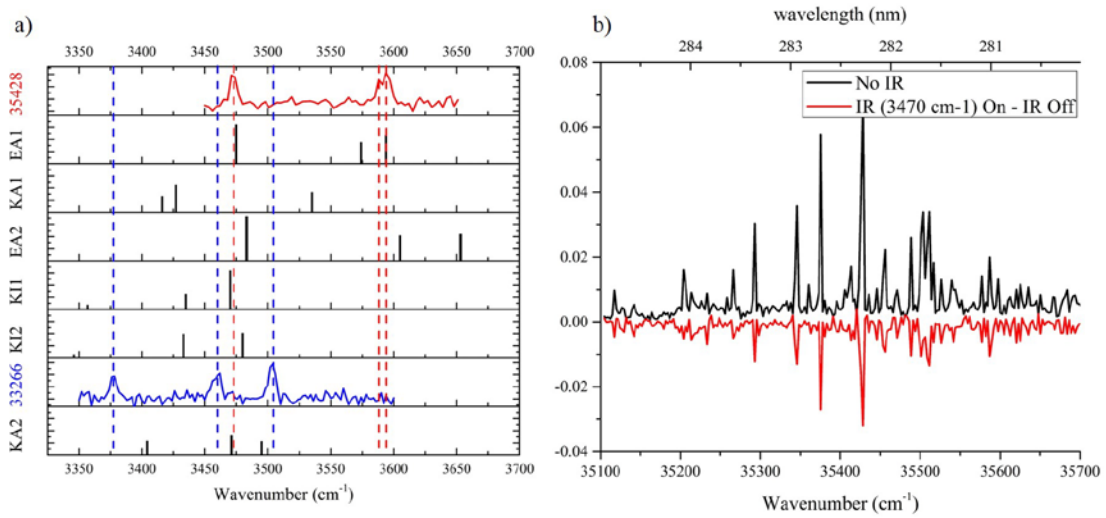

Figure 3 (a) IR UV hole burning results compared to anharmonic simulations for the 6 low energy structures. Experimental spectra are from UV ns probe 35,428 (red) and ps probe 33,266 (blue) cm^{-1} respectively. (b) ns 2C R2PI spectrum (black) and the difference trace below (red) when burning at the EA1 experimental wavelength of 3,470 cm^{-1}. Anharmonic DFT analysis calculated with the B3LYP hybrid functional and the cc-pVTZ basis set.

IR-UV double resonance spectroscopy reveals the presence of the EA1 tautomer, with the origin at 35,269 cm^{-1} and the KA2 tautomer, with the feature at 33,266 cm^{-1}, shown by

Figure 3a. We matched IR-UV hole burning spectra (probed as annotated in Figure 3a) with anharmonic computations. The peaks observed in the ns 2C R2PI scan are all correlated with the EA1 tautomer by IR-UV double resonance spectroscopy in which the IR resonance at 3,470 cm^{-1} was held constant 200 ns prior to scanning the UV source (Figure 3b). We have attached UV-UV hole burning results at 35,428 cm^{-1} as supplemental figure (S.2) which further confirms that all the peaks shown in the ns spectrum belong to a single tautomer which we identify as EA1. After characterization the KA2 and EA1 electronic origin transition energies correlated to within 10% of those predicted for KA1 and EA1 by Szabla et al. and KA1 by Hu et al.[21, 26]

Referring to Chart 1, KA2 is predicted to be the highest energy structure indicating that if this tautomer is present all other forms may be present in our beam as well. Jet-cooling is not an equilibrium process so we cannot predict the tautomer distribution but in our experience in our set-up usually the lowest energy tautomers up to typically about 50 kJ/mol are present. Furthermore, the KA1 tautomer was observed in matrix isolation experiments.[24-25] Three possible reasons certain tautomers are not observed in our experiment are the following. (1) There can be tautomers that absorb in different ranges of the UV spectrum, which we have not covered. (2) Our experiment measures action spectroscopy rather than direct absorption. It is possible that a molecule is excited by the first photon but not ionized by the second. One way this situation can occur is when the excited state lifetime is significantly shorter than the ionizing laser pulse. A very similar situation exists for guanine: the lowest energy keto tautomers, equivalent to KA1 in isoC, have not been observed so far by R2PI, although from direct absorption in microwave experiments and in He droplets they are known to exists.[31-32] (3) A molecule may undergo fragmentation after excitation or

ionization adding complexity to the action spectrum as we typically monitor only the parent ion mass. We did not observe any obvious non-statistical fragmentation.

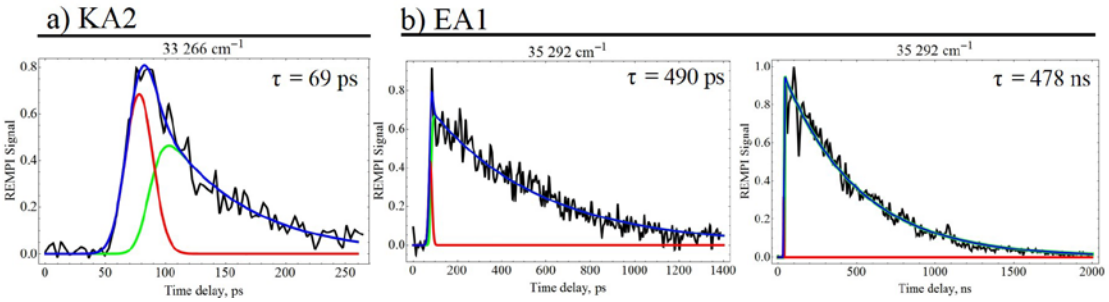

Figure 4: Pump-Probe results from the origin bands of (a) the KA2 and (b) the EA1 tautomer in the ps and ns regimes. The data in (a-b) is fit to a curve (blue) which is the sum of a single exponential decay convolved with a Gaussian component (green) representative of our instrument response function (IRF) and the IRF itself (red).

Figure 4 shows a selection of the pump-probe results from the origin transitions of EA1 and KA2; additional pump-probe fits are found in supplemental material (S.3). The derived lifetimes are shown within Figure 2a-b. The 463-491 ps lifetime of the EA1 tautomer represents the decay rate of the excited state. All pump-probe curves were fit to a mono-exponential decay.

We probed the broad elevated baseline signal present to the red of the EA1 origin in Figure 2a in hopes of attributing it to a specific species from Chart 1. The lifetime of 491 ps agrees with the ps component measured for EA1. We were unable to support this pump-probe correlation to EA1 with conclusive IR-UV hole burning results, like those from Figure 3a. The inability to obtain a clear IR-UV spectrum would be consistent with hot bands.

	keto KA1	keto KA2	enol
Isocytosine	N/O	69 ps	489 ps / 478 ns
Cytosine	N/O	730 ps[33] / 290 ns[34]	*56 ps / *30.5 ns
Guanine	N/O	N/O	13 ns[35] / 40 ns[35]

Table 1 Vibrationless excited state lifetimes. N/O = not observed. *These reported pump-probe results for enol-C were not obtained at the 0-0 transition but rather on the rising edge of its broad initial absorption region

Table 1 lists vibrationless excited state lifetimes, following 0-0 excitation unless otherwise noted, which we found here for isoC and compares those with the equivalent lifetimes for C and G. In terms of its photo-dynamics, isoC has elements of both G and C. The six membered ring in G is an amino-pyrimidione, identical to isoC with a five membered ring that immobilizes the C5=C6 bond that is free in isoC. Szabla et al. identified major conical intersections involving ring puckering, C=O stretching, NH_2 out-of-plane bending and C=C rotation.[21] The former three are similar to the CIs that dominate G dynamics[36] while the latter cannot occur in G but is characteristic for pyrimidines, including cytosine.[37]

We first compare isoC with G. Neither the 1H-9h-keto-amino (KA1 equiv) nor the 3H-keto-amino (KA2 equiv) have been identified yet by ps or ns R2PI. So in both isoC and G we do not observe the KA1 form (because of the difference in numbering between pyrimidines and purines this is N3H for isoC and N1H for G, see Figure 1). For G this is the

WC form and is slightly less in energy than the imino forms, which are observed.[36, 38] As noted before, one likely reason for not observing a species with R2PI is an excited state lifetime significantly shorter than the laser pulse length. In the G experiments pulse widths were of the order of 5 ns and in the current isoC experiments they are lower limited at 30 ps. Excited states with lifetimes of the order of a few hundred fs could thus defy detection by R2PI in these experiments. Notably the conical intersection that is most responsible for the ultrafast IC in the G keto case involves pyramidalization at the C2 position and does not involve the 5-membered ring[29, 36, 39-40] Therefore, it is possible for the isoC KA1 form to undergo very similar ultrafast IC. For the KA2 form of isoC we find a lifetime of 69 ps while the equivalent form for G was not observed with R2PI although it is lower in energy than the imino forms that are observed with R2PI.[31-32, 41] For both compounds the enol form is significantly longer lived, with two independent decay channels of almost 0.5 ns and 0.5 μs for isoC and 13 ns and 40 ns for G.[35] In both cases we consider that the long lived dark state could be a triplet state and for G the 13 ns decay can be attributed to fluorescence.[42] In the case of enol isoC the observation of two decays with a 3 orders of magnitude difference implies that those two channels do not decay from the same excited state. If they did, the higher rate process would have 3 orders of magnitude larger quantum yield and dwarf the signal from the lower rate process. Instead we assume an ultrafast population of a doorway state, possibly a triplet, which in turn decays at the slow rate.

In comparing isoC and C we notice larger differences in excited state dynamics. Again we do not see the KA1 equivalent form for C, which is about 30 kJ/mol higher in energy than the WC KA2 equivalent and enol forms. The KA2 form, which is the lowest energy keto form for C, behaves very different from isoC. Leutwyler and coworkers have reported

this case in great detail, finding a vibrationless decay time of 730 ps.[33, 43-45] Nir et al. reported on a long lived state, presumably a triplet, with a 290 ns lifetime.[34, 46] These observations suggest different dynamics than for isoC where we found a single 69 ps decay. For the enol form of C we find a 56 ps short component which populates a longer lived state with a 30.5 ns lifetime (shown in S4). Because the ns R2PI spectra of enol C, also reported by Nir et al., is broad and without a clear 0-0 transition[46] we performed these pump-probe measurements on the rising edge of the broad signal which appears along with the ps 2C R2PI in supplemental information (S.4). So for C the vibrationless excited state for the enol form is shorter lived than for the keto form, contrary to the situation for both G and isoC. Szabla et al. find a CI for the isoC enol that involves the C5=C6 twist, which also plays a role in C, however according their calculations only 14% of the trajectories follow this path in isoC.[21] It should be noted that their trajectories start at 5.5 ± 0.2 eV which is a full eV more excited state energy than what we impart in our experiments. This may suggest that the C5=C6 CI for EA1 has an energy barrier of up to 1 eV.

The conclusion that isoC resembles G in its photochemistry is just one of the considerations in evaluating its potential role in prebiotic scenarios. For example, we are currently investigating the photo-stability of isoguanine as one of its possible alternative base pair partners. Furthermore, the response to radiation is wavelength dependent and its consideration should not be limited to a single wavelength or small parts of the spectrum. The study of the dynamics near the threshold for absorption provides opportunities to probe the potential energy landscape close to the most relevant CIs and barriers. It is hoped that these data will serve as support for further detailed theoretical treatments.

Experimental section

Here we report results which identify the EA1 and KA2 tautomers of cold isocytosine prepared in a molecular beam. We have investigated the absorption spectrum with 2C R2PI, identified the tautomers with IR-UV hole burning, and performed pump-probe experiments to probe excited state relaxation dynamics in the ns and ps time regimes. The instrument and explanation of these specific techniques are detailed elsewhere and very briefly outlined here.[35, 47] IsoC standard (Sigma, ≥99%) is entrained into a pulsed molecular beam by laser desorption and ionized by tunable 2C R2PI. The ps spectroscopic and pump-probe delay measurements are performed with a Nd:YAG driven Optical Parametric Oscillator (OPG) laser system which produces ~30 ps laser pulses. The molecule is excited by the tunable light from the OPG and ionized by 213 nm, which is mechanically delayed up to 1.5 ns before colineation with the OPG beam. A variable electronic delay between OPG UV laser and an excimer laser (193 nm, 6 ns pulse width) is used for spectroscopic and pump-probe measurements in the ns time delay range.

For IR-UV double resonant spectroscopy an optical parametric oscillator/amplifier (OPO/OPA) precedes the 2C R2PI by 200 ns. IR resonant frequencies are compared to anharmonic DFT analysis calculated with the B3LYP hybrid functional with the cc-pVTZ basis set.

Acknowledgements:

This work was supported by National Aeronautics and Space Administration Grant NNX12AG77G and by the National Science Foundation under CHE-1301305. We

acknowledge support from the Center for Scientific Computing from the CNSI, MRL: an NSF MRSEC (DMR-1121053) and NSF CNS-0960316.

Supporting Content:

Two dimensional TOF data, double resonant UV-UV spectrum of EA1 isoC, and additional pump-probe results of EA1 isoC and enol C.

Supplemental information

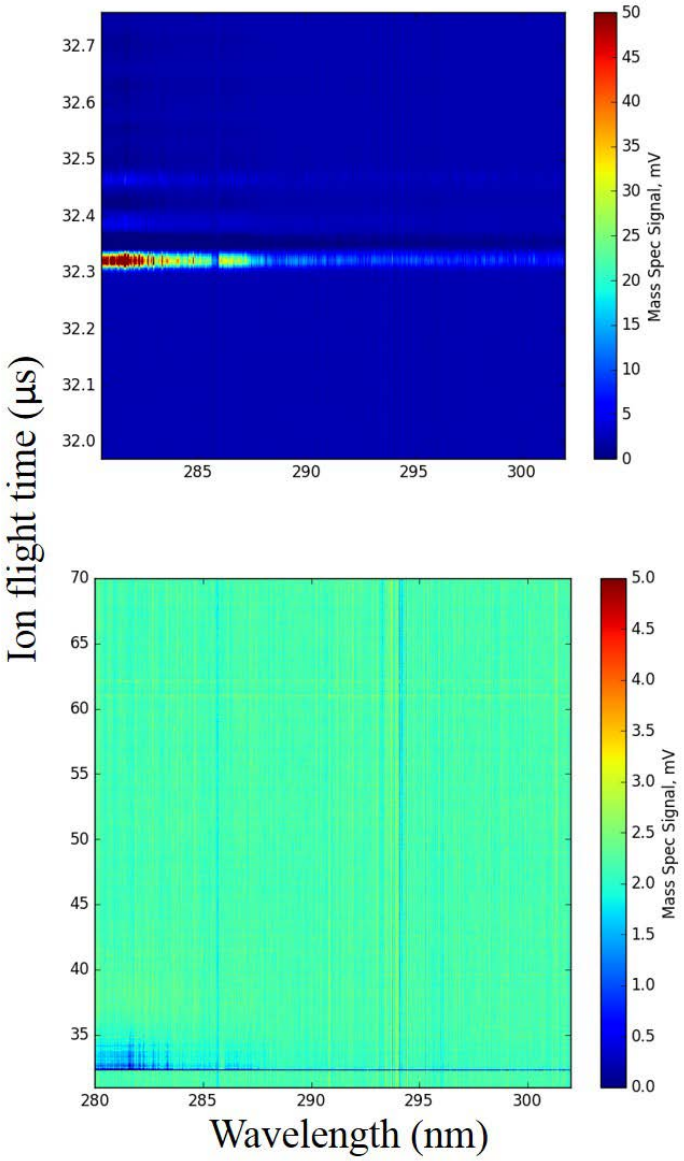

S.1 The two-dimensional time-of-flight data showing ion signal intensity (z axis 0-50 mv top, 0-5 mv bottom) with respect to flight time (y axis) and excitation wavelength (x axis). The only signal is the parent mass of isoC at 32.3 us across all wavelengths. Therefore, no signal is due to the fragmentation of higher order mass ions.

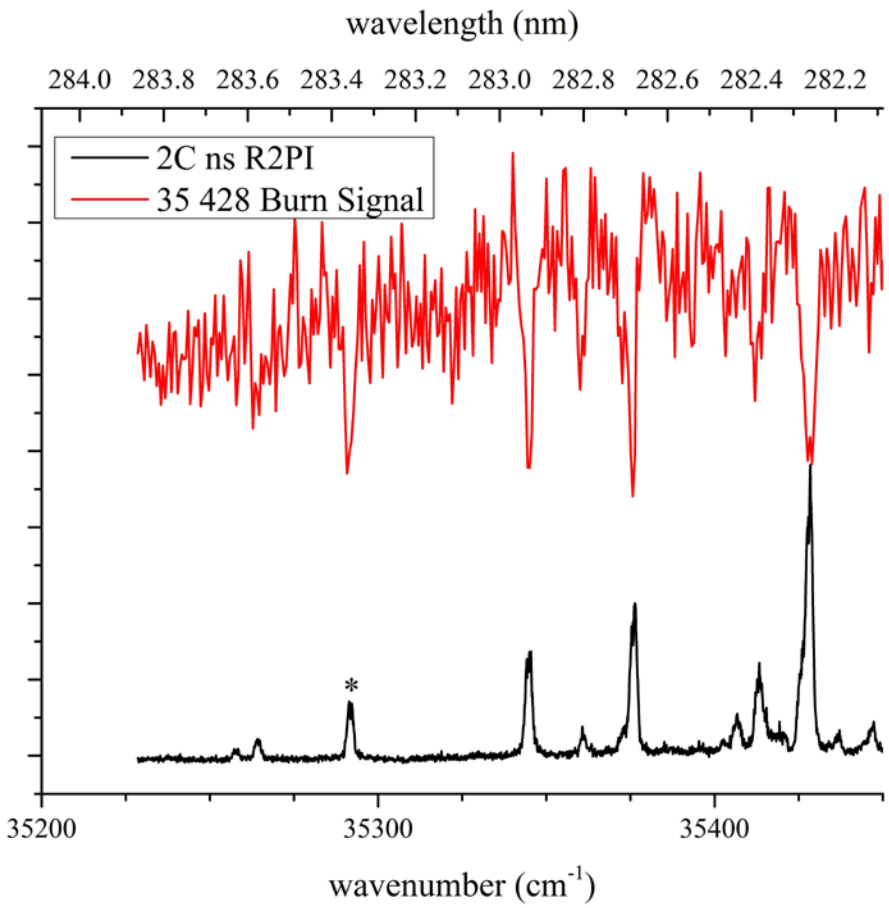

S.2 The UV-UV of the EA1 region (35,428 cm^{-1} probe) supporting the IR-UV in Figure 3b that all signal in the ns scan within the shown range is from the EA1 tautomer only. The EA1 origin of 35,292 cm^{-1} is starred (*).

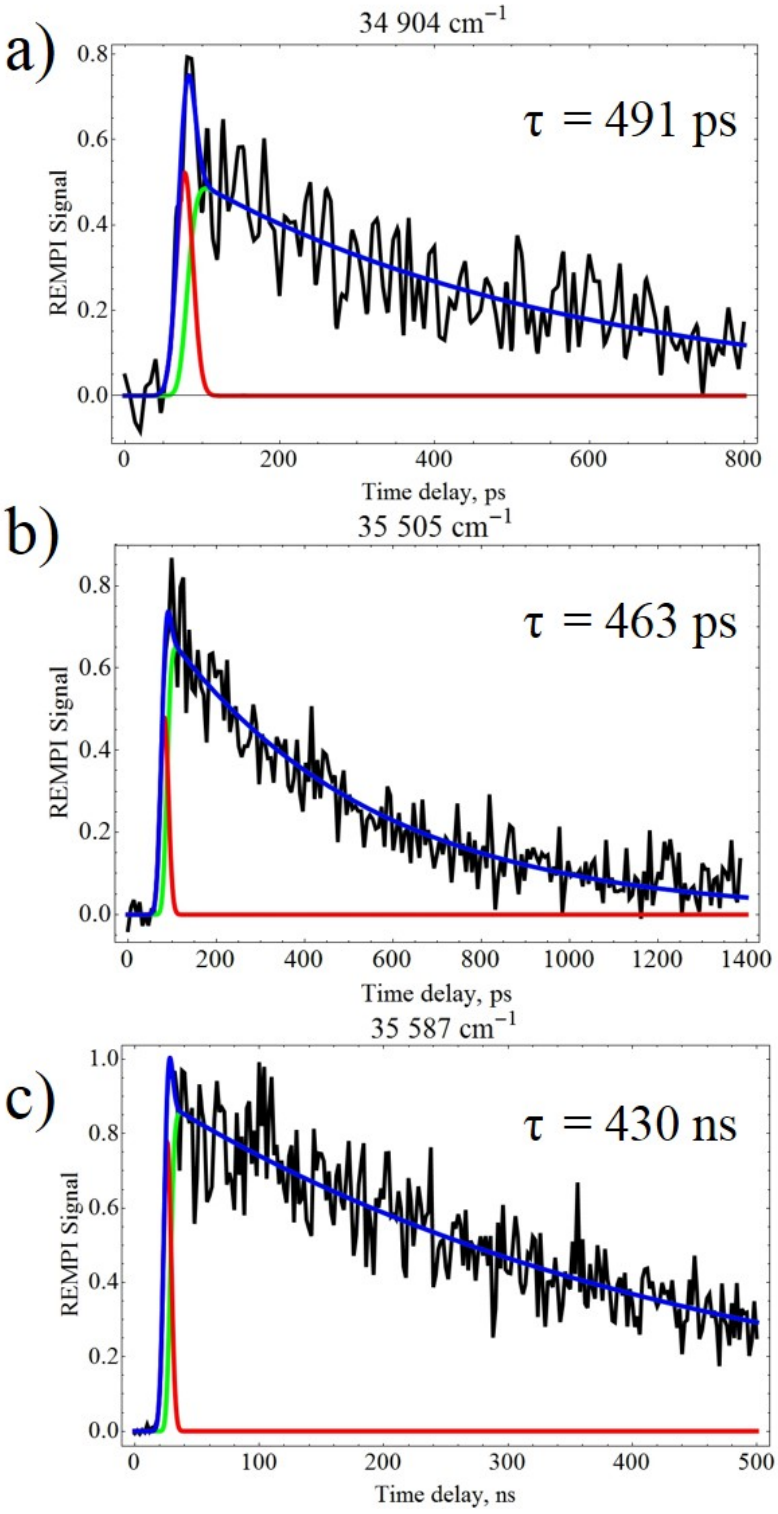

S.3 The pump-probe results (a) through (c) at excitations other than the 0-0 transition wavelengths. The data in (a-c) is fit to a curve (blue) which is the sum of a single exponential decay convolved with a Gaussian component (green) representative of our instrument response function (IRF) and the IRF itself (red).

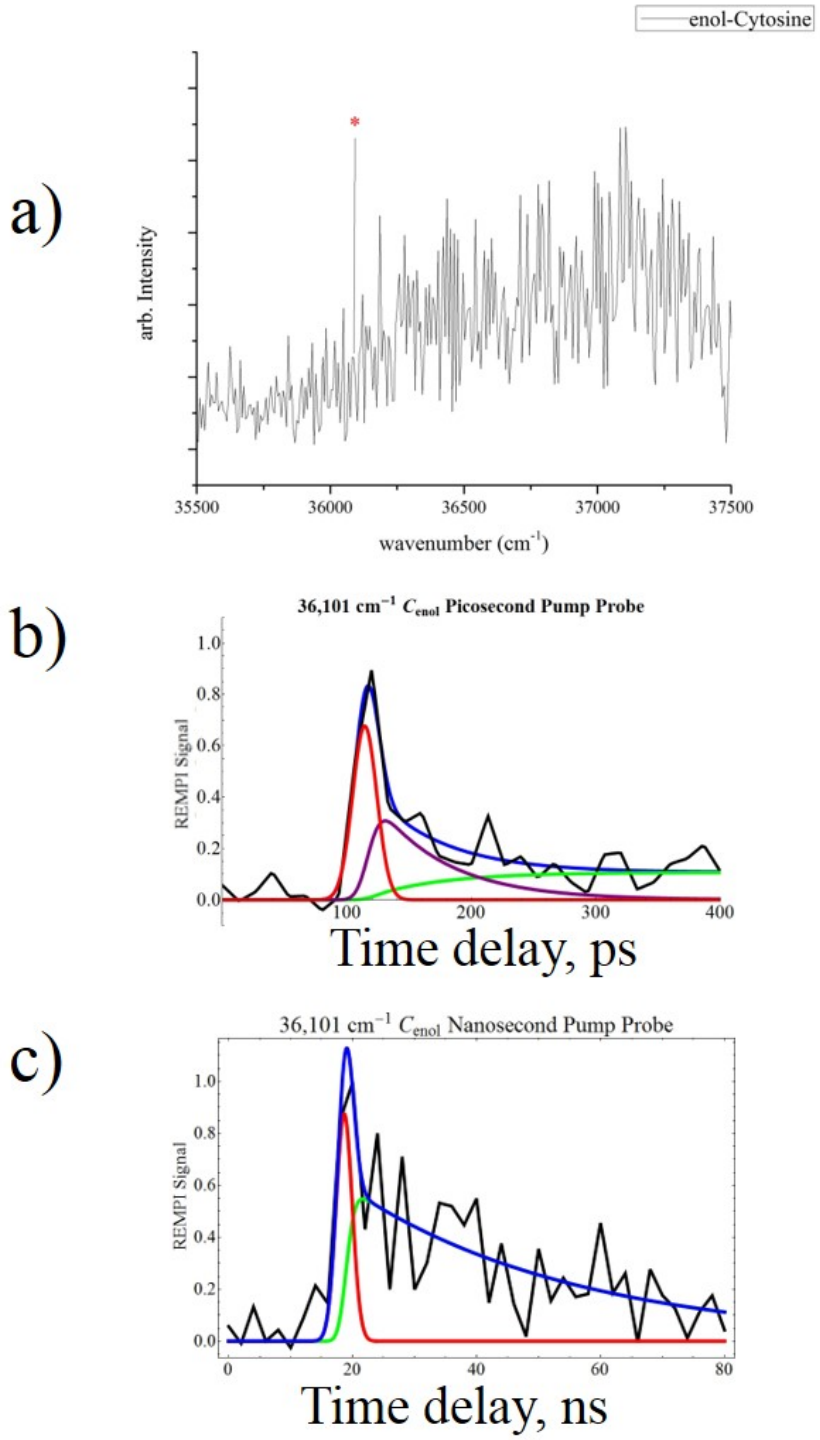

S.4 The (a) ps 2C R2PI and (b) ps pump-probe results of enol C. 213 nm was the second color for both, and (c) ns pump-probe results of enol C with 193 nm as a second color. In the ps pump-probe two lifetimes were fit for, a short lifetime (purple) of 56 ps which populates a >5 ns secondary lifetime (green). The ns pump-probe fit to a single decay of 30.5 ns (green) In both the IRF is plotted in red. Our previous work on 6-TG

showed the upper fitting limit of our ps setup to be ~5 ns, longer lifetimes need additional fitting in the ns regime.

References

(1) Beckstead, A. A.; Zhang, Y. Y.; De Vries, M. S.; Kohler, B. Life in the Light: Nucleic Acid Photoproperties as a Legacy of Chemical Evolution. *PCCP* **2016,** *18*, 24228-24238.

(2) Nir, E.; Kleinermanns, K.; Grace, L.; De Vries, M. S. On the Photochemistry of Purine Nucleobases. *J. Phys. Chem. A* **2001,** *105*, 5106-5110.

(3) Rios, A. C.; Tor, Y. On the Origin of the Canonical Nucleobases: An Assessment of Selection Pressures across Chemical and Early Biological Evolution. *Isr. J. Chem.* **2013,** *53*, 469-483.

(4) Middleton, C. T.; De La Harpe, K.; Su, C.; Law, Y. K.; Crespo-Hernandez, C. E.; Kohler, B. DNA Excited-State Dynamics: From Single Bases to the Double Helix. *Annu. Rev. Phys. Chem.* **2009,** *60*, 217-239.

(5) Miller, S. L.; Orgel, L. E. *The Origins of Life on the Earth*. Prentice-Hall: Englewood Cliffs, NJ, **1974**.

(6) Gustavsson, T.; Improta, R.; Markovitsi, D. DNA/Rna: Building Blocks of Life under Uv Irradiation. *J. Phys. Chem. Lett.* **2010,** *1*, 2025-2030.

(7) Kohler, B. Nonradiative Decay Mechanisms in DNA Model Systems. *J. Phys. Chem. Lett.* **2010,** *1*, 2047-2053.

(8) Kleinermanns, K.; Nachtigallová, D.; De Vries, M. S. Excited State Dynamics of DNA Bases. *Int. Rev. Phys. Chem.* **2013,** *32*, 308-342.

(9) Crespo-Hernandez, C. E.; Martinez-Fernandez, L.; Rauer, C.; Reichardt, C.; Mai, S.; Pollum, M.; Marquetand, P.; Gonzalez, L.; Corral, I. Electronic and Structural Elements That Regulate the Excited-State Dynamics in Purine Nucleobase Derivatives. *J. Am. Chem. Soc.* **2015,** *137*, 4368-4381.

(10) Yang, Z. Y.; Hutter, D.; Sheng, P. P.; Sismour, A. M.; Benner, S. A. Artificially Expanded Genetic Information System: A New Base Pair with an Alternative Hydrogen Bonding Pattern. *Nucleic Acids Res.* **2006,** *34*, 6095-6101.

(11) Leontis, N. B.; Stombaugh, J.; Westhof, E. The Non-Watson-Crick Base Pairs and Their Associated Isostericity Matrices. *Nucleic Acids Res.* **2002,** *30*, 3497-3531.

(12) Wojciechowski, F.; Leumann, C. J. Alternative DNA Base-Pairs: From Efforts to Expand the Genetic Code to Potential Material Applications. *Chem. Soc. Rev.* **2011,** *40*, 5669-5679.

(13) Cafferty, B. J.; Hud, N. V. Was a Pyrimidine-Pyrimidine Base Pair the Ancestor of Watson-Crick Base Pairs? Insights from a Systematic Approach to the Origin of Rna. *Isr. J. Chem.* **2015,** *55*, 891-905.

(14) Rich, A. On the Problems of Evolution and Biochemical Information Transfer. In *Horizons in Biochemistry*, Michael Kasha, B. P., Ed. Academic Press: New York, **1962**, pp 103-126.

(15) Saladino, R.; Crestini, C.; Cossetti, C.; Di Mauro, E.; Deamer, D. Catalytic Effects of Murchison Material: Prebiotic Synthesis and Degradation of Rna Precursors. *Origins Life Evol B* **2011,** *41*, 437-451.

(16) Roberts, C.; Bandaru, R.; Switzer, C. Theoretical and Experimental Study of Isoguanine and Isocytosine: Base Pairing in an Expanded Genetic System. *J. Am. Chem. Soc.* **1997,** *119*, 4640-4649.
(17) Yang, X. L.; Sugiyama, H.; Ikeda, S.; Saito, I.; Wang, A. H. Structural Studies of a Stable Parallel-Stranded DNA Duplex Incorporating Isoguanine:Cytosine and Isocytosine:Guanine Basepairs by Nuclear Magnetic Resonance Spectroscopy. *Biophys. J.* **1998,** *75*, 1163-1171.
(18) Sismour, A. M.; Benner, S. A. The Use of Thymidine Analogs to Improve the Replication of an Extra DNA Base Pair: A Synthetic Biological System. *Nucleic Acids Res.* **2005,** *33*, 5640-5646.
(19) Hirao, I. Unnatural Base Pair Systems for DNA/Rna-Based Biotechnology. *Curr. Opin. Chem. Biol.* **2006,** *10*, 622-627.
(20) Lee, S. J.; Min, A.; Ahn, A.; Moon, C. J.; Choi, M. Y.; Ishiuchi, S.-I.; Miyazaki, M.; Fujii, M. In *Resonance Enhanced Multi-Photon Ionization (Rempi) and Double Resonance (Uv-Uv and Ir-Uv) Spectroscopic Investigation Isocytosine*, OSU International Symposium on Molecular Spectroscopy, Ohio State University: **2013**.
(21) Szabla, R.; Gora, R. W.; Sponer, J. Ultrafast Excited-State Dynamics of Isocytosine. *Phys. Chem. Chem. Phys.* **2016,** *18*, 20208-20218.
(22) Shukla, M. K.; Leszczynski, J. Investigations of the Excited-State Properties of Isocytosine: An Ab Initio Approach. *Int. J. Quantum Chem* **2000,** *77*, 240-254.
(23) Bakalska, R. I.; Delchev, V. B. Comparative Study of the Relaxation Mechanisms of the Excited States of Cytosine and Isocytosine. *J. Mol. Model.* **2012,** *18*, 5133-5146.
(24) Ivanov, A. Y.; Stepanian, S. G.; Adamowicz, L. Tautomeric Transitions of Isocytosine Isolated in Argon and Neon Matrices Induced by Uv Irradiation. *J. Mol. Struct.* **2012,** *1025*, 92-104.
(25) Vranken, H.; Smets, J.; Maes, G.; Lapinski, L.; Nowak, M. J.; Adamowicz, L. Infrared Spectra and Tautomerism of Isocytosine; an Ab Initio and Matrix Isolation Study. *Spectrochimica Acta Part A: Molecular Spectroscopy* **1994,** *50*, 875-889.
(26) Hu, D.; Liu, Y. F.; Sobolewski, A. L.; Lan, Z. Nonadiabatic Dynamics Simulation of Keto Isocytosine: A Comparison of Dynamical Performance of Different Electronic-Structure Methods. *Phys. Chem. Chem. Phys.* **2017,** *19*, 19168-19177.
(27) Merchan, M.; Gonzalez-Luque, R.; Climent, T.; Serrano-Andres, L.; Rodriguez, E.; Reguero, M.; Pelaez, D. Unified Model for the Ultrafast Decay of Pyrimidine Nucleobases. *J. Phys. Chem. B* **2006,** *110*, 26471-26476.
(28) Pepino, A. J.; Segarra-Marti, J.; Nenov, A.; Improta, R.; Garavelli, M. Resolving Ultrafast Photoinduced Deactivations in Water-Solvated Pyrimidine Nucleosides. *J. Phys. Chem. Lett.* **2017,** *8*, 1777-1783.
(29) Improta, R.; Santoro, F.; Blancafort, L. Quantum Mechanical Studies on the Photophysics and the Photochemistry of Nucleic Acids and Nucleobases. *Chem. Rev.* **2016,** *116*, 3540-3593.
(30) Trachsel, M. A.; Lobsiger, S.; Schär, T.; Blancafort, L.; Leutwyler, S. Planarizing Cytosine: The S1 State Structure, Vibrations, and Nonradiative Dynamics of Jet-Cooled 5,6-Trimethylenecytosine. *The Journal of Chemical Physics* **2017,** *146*, 244308.
(31) Choi, M. Y.; Miller, R. E. Four Tautomers of Isolated Guanine from Infrared Laser Spectroscopy in Helium Nanodroplets. *J. Am. Chem. Soc.* **2006,** *128*, 7320-7328.

(32) Mons, M.; Piuzzi, F.; Dimicoli, I.; Gorb, L.; Leszczynski, J. Near-Uv Resonant Two-Photon Ionization Spectroscopy of Gas Phase Guanine: Evidence for the Observation of Three Rare Tautomers. *J. Phys. Chem. A* **2006,** *110*, 10921-10924.
(33) Blaser, S.; Trachsel, M. A.; Lobsiger, S.; Wiedmer, T.; Frey, H. M.; Leutwyler, S. Gas-Phase Cytosine and Cytosine-N1-Derivatives Have 0.1-1 Ns Lifetimes near the S1 State Minimum. *J. Phys. Chem. Lett.* **2016,** *7*, 752-757.
(34) Nir, E.; Muller, M.; Grace, L. I.; De Vries, M. S. Rempi Spectroscopy of Cytosine. *Chem. Phys. Lett.* **2002,** *355*, 59-64.
(35) Siouri, F. M.; Boldissar, S.; Berenbeim, J. A.; De Vries, M. S. Excited State Dynamics of 6-Thioguanine. *J. Phys. Chem. A* **2017,** *121*, 5257-5266.
(36) Marian, C. M. The Guanine Tautomer Puzzle: Quantum Chemical Investigation of Ground and Excited States. *J. Phys. Chem. A* **2007,** *111*, 1545-1553.
(37) Kistler, K. A.; Matsika, S. Radiationless Decay Mechanism of Cytosine: An Ab Initio Study with Comparisons to the Fluorescent Analogue 5-Methyl-2-Pyrimidinone. *J. Phys. Chem. A* **2007,** *111*, 2650-2661.
(38) Mons, M.; Dimicoli, I.; Piuzzi, F. Isolated Guanine: Tautomerism, Spectroscopy and Excited State Dynamics. In *Radiation Induced Molecular Phenomena in Nucleic Acids: A Comprehensive Theoretical and Experimental Analysis*, Shukla, M. K.; Leszczynski, J., Eds. Springer Netherlands: Dordrecht, **2008**, pp 343-367.
(39) Chen, H.; Li, S. Ab Initio Study on Deactivation Pathways of Excited 9h-Guanine. *J. Chem. Phys.* **2006,** *124*, 154315.
(40) Yamazaki, S.; Domcke, W.; Sobolewski, A. L. Nonradiative Decay Mechanisms of the Biologically Relevant Tautomer of Guanine. *J. Phys. Chem. A* **2008,** *112*, 11965-11968.
(41) Alonso, J. L.; Pena, I.; Lopez, J. C.; Vaquero, V. Rotational Spectral Signatures of Four Tautomers of Guanine. *Angew. Chem. Int. Ed. Engl.* **2009,** *48*, 6141-6143.
(42) Chin, W.; Mons, M.; Dimicoli, I.; Piuzzi, F.; Tardivel, B.; Elhanine, M. Tautomer Contributions to the near Uv Spectrum of Guanine: Towards a Refined Picture for the Spectroscopy of Purine Molecules. *The European Physical Journal D* **2002,** *20*, 347-355.
(43) Lobsiger, S.; Etinski, M.; Blaser, S.; Frey, H. M.; Marian, C.; Leutwyler, S. Intersystem Crossing Rates of S1 State Keto-Amino Cytosine at Low Excess Energy. *J. Chem. Phys.* **2015,** *143*, 234301.
(44) Lobsiger, S.; Trachsel, M. A.; Frey, H. M.; Leutwyler, S. Excited-State Structure and Dynamics of Keto-Amino Cytosine: The 1pipi* State Is Nonplanar and Its Radiationless Decay Is Not Ultrafast. **2013,** *117*, 6106-6115.
(45) Lobsiger, S.; Leutwyler, S. The Adiabatic Ionization Energy and Triplet T-1 Energy of Jet-Cooled Keto-Amino Cytosine. *J. Phys. Chem. Lett.* **2012,** *3*, 3576-3580.
(46) Nir, E.; Hunig, I.; Kleinermanns, K.; De Vries, M. S. The Nucleobase Cytosine and the Cytosine Dimer Investigated by Double Resonance Laser Spectroscopy and Ab Initio Calculations. *Phys. Chem. Chem. Phys.* **2003,** *5*, 4780-4785.
(47) Meijer, G.; Devries, M. S.; Hunziker, H. E.; Wendt, H. R. Laser Desorption Jet-Cooling of Organic-Molecules - Cooling Characteristics and Detection Sensitivity. *Appl Phys B-Photo* **1990,** *51*, 395-403.

II. Excited State Dynamics of 6-Thioguanine

Faady M. Siouri, Samuel Boldissar, Jacob A. Berenbeim, Mattanjah S. de Vries*

Department of Chemistry and Biochemistry, University of California, Santa Barbara, CA 93016-9510

Reprinted with Permission from Siouri, F. M.; Boldissar, S.; Berenbeim, J. A.; De Vries, M. S. Excited State Dynamics of 6-Thioguanine. *J. Phys. Chem. A* **2017,** *121*, 5257-5266.

Abstract

Here we present the excited state dynamics of jet-cooled 6-thioguanine (6-TG), using resonance-enhanced multiphoton ionization (REMPI), IR-UV double resonance spectroscopy, and pump-probe spectroscopy in the nanosecond and picosecond time domains. We report data on 2 thiol tautomers, which appear to have different excited state dynamics. These decay to a dark state, possibly a triplet state, with rates depending on tautomer form and on excitation wavelength, with the fastest rate on the order of 10^{10} s^{-1}. We also compare 6-TG with 9-enolguanine, for which we observed decay to a dark state with a two orders of magnitude smaller rate. At increased excitation energy (~ +500 cm^{-1}) an additional pathway appears for the predominant thiol tautomer. Moreover, the excited state dynamics for 6-TG thiols is different from that recently predicted for thiones.

1. Introduction

The DNA and RNA bases have a built-in protection mechanism against UV radiative damage. When they absorb UV light, they return safely to the electronic ground state in less than a picosecond by internal conversion (IC). This ultrafast IC dominates alternative relaxation pathways, such as intersystem crossing (ISC), so potentially harmful photochemical processes are largely averted. The availability of rapid IC pathways depends critically on molecular structure. This dependence results from the fact that the conical intersections that mediate IC occur at molecular geometries that differ strongly from ground state minimum geometries. Therefore the excited state dynamics of nucleobases can differ drastically for different derivatives,[1-9] analogues,[10-12] and even tautomers.[13-15] Many derivatives and analogues of the canonical nucleobases that could serve as alternative bases lack the UV protection afforded by rapid internal conversion. This difference suggests a possible prebiotic photochemical selection of nucleobases on an early earth. In the case of guanine (G), the keto tautomer, which is prevalent in DNA, is characterized by rapid IC in contrast to enol and imino tautomers.[15-24] When the oxygen atom in DNA is replaced with a sulfur atom, the photochemistry changes dramatically due to the heavy atom effect on spin-forbidden transitions.[25] Canonical DNA bases absorb UVB (290-320 nm); whereas, sulfur substituted DNA analogues such as 6-thioguanine (6-TG), absorb UVA (320-400 nm).[12, 26-28] Yu et al. reported a significant increase in intersystem crossing rate for 2-thiouracil relative to uracil in the gas phase, following excitation at 295 and 260 nm, respectively[29]. The comparison of the excited state dynamics of G versus 6-TG has so-far been limited to their keto and corresponding thione tautomers.[30-31] The photoproducts and photochemistry of the enol and corresponding thiol tautomers have not been studied in great detail. In this work we find significant transition rates to a dark state, most likely a triplet state, with estimated quantum yields of the order of 25% for enol G and considerably higher rates for

thiol 6-TG. Here and throughout quantum yield estimates represent an upper limit as we may not be observing all decay processes in our experiment.

6-TG and other thiopurines are effective anti-inflammatory, anticancer, and immunosuppressive drugs used for over 50 years,[32] however, prolonged treatment with 6-TG has been associated with a 65-250 times increased risk of skin cancer.[33] 6-TG is of interest because it can be incorporated into a patient's DNA,[34] increasing skin sensitivity to UVA radiation. Once 6-TG is converted into 6-TG nucleotide, it replaces the guanine in the patient's DNA.[35] Excitation of DNA-6TG with UVA radiation generates a series of reactions leading to the formation of reactive oxygen[36] species such as singlet oxygen that can damage both DNA and proteins.[37-38] Other consequences of UVA interaction with DNA 6-TG includes DNA and protein oxidation, DNA-protein cross linking, DNA strand breakage, and DNA interstrand cross linking.[39]

Guanine is known to relax to the ground state by internal conversion with lifetimes of 140 fs and 2.3 ps,[24] and by fluorescence on the timescale of 12 to 25 ns.[40] These fast relaxation times are indicative of a nucleobase that efficiently dissipates internal energy introduced through UV excitation. However, the fast decay was observed in femtosecond pump-probe experiments, performed with a 267 nm excitation pulse and 400 nm probe pulse, which do not map out the complete excited state dynamics. Furthermore, these femtosecond experiments lack tautomer selectivity. In solution guanine is primarily in the keto form. In the gas phase, four guanine tautomers were observed in molecular beams by resonance enhanced multiphoton ionization (REMPI); two imino, and two enol forms.[18, 41] Choi et al. observed keto tautomers in helium droplets which suggests the keto tautomers are present in molecular beams but unobserved by multiphoton ionization.[42] In the present work,

we evaluate the excited state lifetime of the 9-H enol guanine and compare it with that of thiol 6-TG. Research on 6-TG has focused on exploring the excited state dynamics of the thione tautomer, but no studies have been reported on the thiol tautomer.[30, 43-45] Reichardt et al. investigated the excited state dynamics of 6-thioguanosine in phosphate buffer and in acetonitrile solutions via femtosecond broadband transient absorption spectroscopy coupled with quantum chemical calculations.[43] They determined that in aqueous buffer solution, ~ 80% of the S_2 ($\pi\pi^*$) excited state population decays by ultrafast intersystem crossing to T_3 ($n\pi^*$) which is ~0.1 eV below the S_2 Franck-Condon (FC) region, suggesting a strong spin-orbit coupling between these two states. However, Martínez-Fernández et al have later argued that the proposed channel is not the correct pathway to the triplet manifold.[30, 44] Instead, they used *ab initio* calculations to show that the dominant pathway is $S_2 \rightarrow S_1 \rightarrow T_2 \rightarrow T_1$. Moreover, Martínez-Fernández et al assigned T_3 as ($\pi\pi^*$) instead of ($n\pi^*$). As a result, Martínez-Fernández et al. determined that the S_2 state ($\pi\pi^*$) and T_3 state ($\pi\pi^*$) negligibly coupled at the FC and S_2 minimum structures. Both authors however agreed that internal conversion and intersystem crossing compete in the relaxation mechanism to the ground state with the intersystem crossing pathway being the major pathway and $S_2 \rightarrow S_1 \rightarrow S_0$ being the minor pathway.

Here we present the tautomeric characterization and excited state dynamics of jet-cooled guanine in the enol form (G_e) and of 6-thioguanine (6-TG) as an alternative nucleobase and as a case study into heavy-atom effects on ISC and application of El-Sayed's rules.[46] We collected 1 and 2-color REMPI on isolated 6-TG, with IR-UV characterization, and performed nanosecond and picosecond pump-probe spectroscopy on G_e and 6-TG to

construct a model of excited state decay from the origin up to ~900 cm^{-1} excess internal energy.

2. Methods

Experimental

The instrument has been previously described in detail and only a brief description of the experimental setup follows.[47] Samples (6-thioguanine, TCI 95%) are mixed with carbon black and placed on a translating graphite substrate directly in front of a pulsed molecular beam valve, based on a piezo cantilever design.[48] They are laser desorbed by a focused Nd:YAG laser (1064 nm, ~ 1 mJ/cm^2), then entrained in a supersonic molecular beam of argon (8 atm backing pressure, 15 μsec pulse width) at a repetition rate of 10 Hz. The cold, neutral molecules are ionized by REMPI and are subsequently detected in a reflectron time of flight mass spectrometer. One-color nanosecond REMPI is carried out with the frequency doubled output of a Lumonics HD-300 tunable dye laser (2 mJ/pulse, 8 ns pulse length, 0.04 cm^{-1} spectral linewidth).

The picosecond REMPI spectroscopic and pump-probe delay measurements are performed with an Ekspla PL2251 Nd:YAG laser system producing ~ 30 ps laser pulses. The 355 nm output pumps an Ekspla PG401 tunable optical parametric generator (OPG) (UV output of 80-120 μJ/pulse, 30 ps pulse length, ~ 6 cm^{-1} spectral linewidth). 6-TG is excited by the OPG UV and ionized by 266 nm, fourth harmonic of the ps pump laser, which is mechanically delayed up to 2 ns before colineation with the OPG beam. A variable

delay between OPG UV laser and an excimer laser (193 nm, 1.5-2 mJ/pulse) is used for pump-probe measurements in the nanosecond range.

For IR-UV double resonant spectroscopy a Laser Vision optical parametric oscillator/amplifier (OPA/OPA) (mid-IR output over the range 3,200-3,800 cm^{-1} of ~3-5 mJ/pulse, 3 cm^{-1} spectral linewidth) precedes the ns REMPI by 200 ns. We perform double resonant spectroscopy with two different pulse sequences in this report: in mode I we scan the IR at a fixed UV probe wavelength and in mode II we scan the UV with a fixed IR burn wavelength. In mode I the IR laser is scanned while the UV laser is fixed on one vibronic transition and signal depletes when the IR laser becomes resonant with that ground state population. The resulting ion-dip spectrum represents the ground state IR spectrum of a single tautomer, selected by the UV probe wavelength. This IR spectrum can be compared with calculated IR frequencies to determine the specific tautomer of the selected vibronic transition. In mode II the IR laser is set to a tautomer-specific vibrational resonance and we scan the UV laser, comparing spectra with IR laser on and off. The difference spectrum identifies peaks in the UV spectrum that arise from the same tautomer.

We performed pump-probe experiments on both the nanosecond and picosecond timescale to determine which types of processes are occurring in this system. By combining information from both time domains and monitoring lifetimes as a function of excitation energy, it is possible to gain an understanding of the excited state dynamics involved in deactivation.

The behavior as a function of time of each decay channel derives from the kinetic equations and from solving the system of ordinary differential equations with boundary

conditions shown in equation 1, where p(t) refers to a primary pathway which is populated at zero delay time and which, with a time constant τ_n, fills a secondary pathway, s(t), which in turn decays with a time constant τ_m. Since measurements are made with a finite pulse width laser, the measured response is a convolution of the instrument response function (IRF) with each of the pump and probe pulses where the IRF is represented by a Gaussian centered around t_0.

The standard deviation of the Gaussian is fitted for each profile rather than using a single value, as reported by Lipert et al.[49] and results in FWHM values which ranged from half to full width of the experimental laser pulses. After convoluting the exponential decays, which gives the excitation profile, the profile is convoluted again with the probe pulse as performed by Spesyvtsev and shown in equations 2a-b.[50] The excitation profile, P(t), consists of a sum of all primary and secondary pathways, where the secondary pathways are multiplied by an ionization efficiency factor (ϕ_{ion}) relative to the primary pathway, as shown in equation 2a. The excitation profile is convolved with 2 Gaussians centered at different t_0 with standard deviation σ in equation 2b. This double convolution is then scaled with a factor f which accounts for the signal intensity being in arbitrary units. The data are fit using a sum of the convolutions in 2b and a Gaussian centered around maximum signal, as performed by Kang et al.[31] We performed all fitting with the Mathematica 10 package which employed the Levenberg–Marquardt algorithm for least squares fitting.[51]

$$\frac{dp}{dt} = -\frac{1}{\tau_n} p(t, \tau_n), \qquad \frac{ds}{dt} = \frac{1}{\tau_n} p(t, \tau_n) - \frac{1}{\tau_m} s(t, \tau_m) \qquad \text{eqn 1}$$

$$P(t) = \sum_{n=1}^{N} \sum_{m=1}^{M} p(t, \tau_n) + \phi_{ion}\, s(t, \tau_m) \qquad \text{eqn 2a}$$

$$I(t) = f \int_0^t G\left(t - t'', t_0^{probe}, \sigma\right) \int_0^t G\left(t - t', t_0^{pump}, \sigma\right) P(t)\, dt'\, dt'' \qquad \text{eqn 2b}$$

Computational Methods

Starting structures for both thiol and thione structures were optimized using the B3LYP hybrid functional with a 6-31+G(2d,p) basis set. The shorthand notation of these structures will include a number, 7 or 9, which indicates which nitrogen is sp^3 hybridized, and a letter, e or k, which indicates whether the structure is a thiol or thione, respectively. This nomenclature was adopted to be consistent with the equivalent enol and keto designations for guanine. These structures were then further optimized using MP2/6-31+G(2d,p), which were then used to perform an anharmonic frequency analysis where ground state minima were confirmed by the absence of imaginary frequencies. The simulated spectra arise from anharmonic frequencies with harmonic intensities using a Lorentzian shape and FWHM of 1 cm^{-1}. The MP2 optimized structures were used for single point energy calculations at the CCSD and EOM-CCSD level with the same basis set. These levels of theory provide good accuracy electronic energies for the ground and electronically excited states, respectively. These computations were performed by using *Gaussian 09*.[52]

Preliminary *ab initio* molecular dynamic simulations were performed on 9e-6TG using surface hopping including arbitrary couplings (SHARC) to augment interpretation of the experimental excited state lifetimes with a first-order relaxation mechanism.[53-54] The package developed by Gonzalez and coworkers performs high accuracy *ab initio*

calculations and modifies nuclear positions as a function of time to obtain molecular dynamic information. The quantum calculations within SHARC were performed with the *Molpro* interface.[55] A limited number of trajectories (10) were run which included three singlet and three triplet electronic states, so that intersystem crossing information could be obtained as well as singlet internal conversion. Once an internal conversion (IC) or intersystem crossing (ISC) geometry was found in a *SHARC* trajectory, the geometry was verified by performing a single point energy calculation with *Gaussian 09*, followed by a linear interpolation of internal coordinates (LIIC) from the Frank-Condon geometry to the intersection of interest. Both *Gaussian 09* and *Molpro* simulations employed the state averaged complete active space self-consistent field method (SA-CASSCF). The active space used in this method consisted of 10 electrons in 10 orbitals (10,10), and used the 6-31G* basis set.

It should be emphasized that the SHARC simulations and LIIC theory were done at a level different from the aforementioned electronic state static energy calculations and anharmonic frequency analysis. We chose this approach to achieve rigorous but preliminary theory at low computational cost and future work on these 6-TG and G enol systems is needed with higher order perturbation methods, such as CASPT2, given the documented complexity of purine excited state models.[56]

3. Results

REMPI

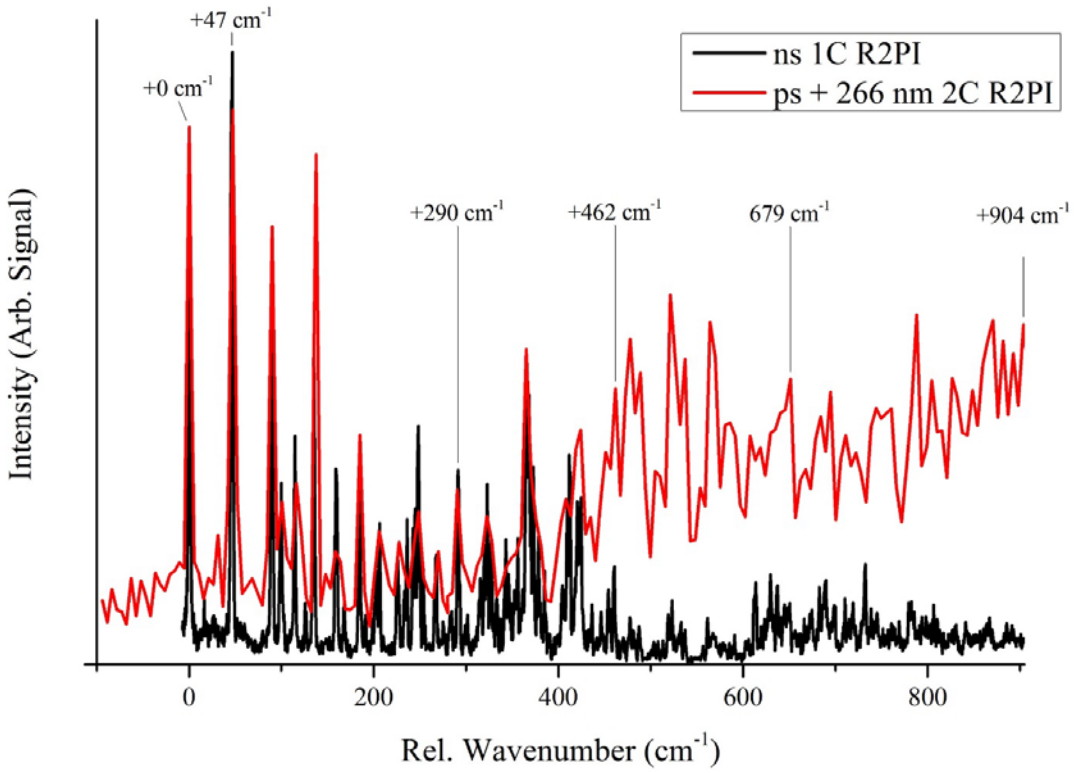

Figure 1. One-color resonant two-photon nanosecond ionization spectrum of jet-cooled 6-thioguanine is shown in black and two-color resonant two-photon picosecond ionization spectrum of jet-cooled 6-thioguanine is shown in red. The wavenumber scale is relative to the 0_0^0 band at 32,343 cm^{-1} and annotations mark where pump-probe was performed. Both spectra have been normalized at +0 cm^{-1}.

Figure 1 shows the REMPI spectrum of jet-cooled 6-TG in the frequency range 32,330 - 33,330 cm^{-1}. The black trace shows nanosecond one-color (1C) REMPI. The spectrum exhibits a sharp red-most band at 32,343 cm^{-1}, which we assume to be a 0_0^0 band and similarly sharp vibronic bands up to +290 cm^{-1}, after which the spectral features lose intensity and congest. The red trace shows the same spectrum with picosecond excitation. In this case the signal is lower so we used two-color (2C) REMPI in which the second color

consisted of 266 nm picosecond pulses. Two-color ionization with nanosecond 193 nm ionization is not shown but shows features identical to ionization at 266 nm. The excitation laser in the 2C-REMPI has a spectral linewidth of 6 cm^{-1}, as opposed to 0.04 cm^{-1} for the laser in the 1C scan. Above 500 cm^{-1} the nanosecond signal is strongly reduced in contrast to the picosecond signal. This observation points to a decrease in excited state lifetime with increasing excitation energy, corresponding to a deactivation pathway with a barrier of the order of 500 cm^{-1}.

Structural Determination

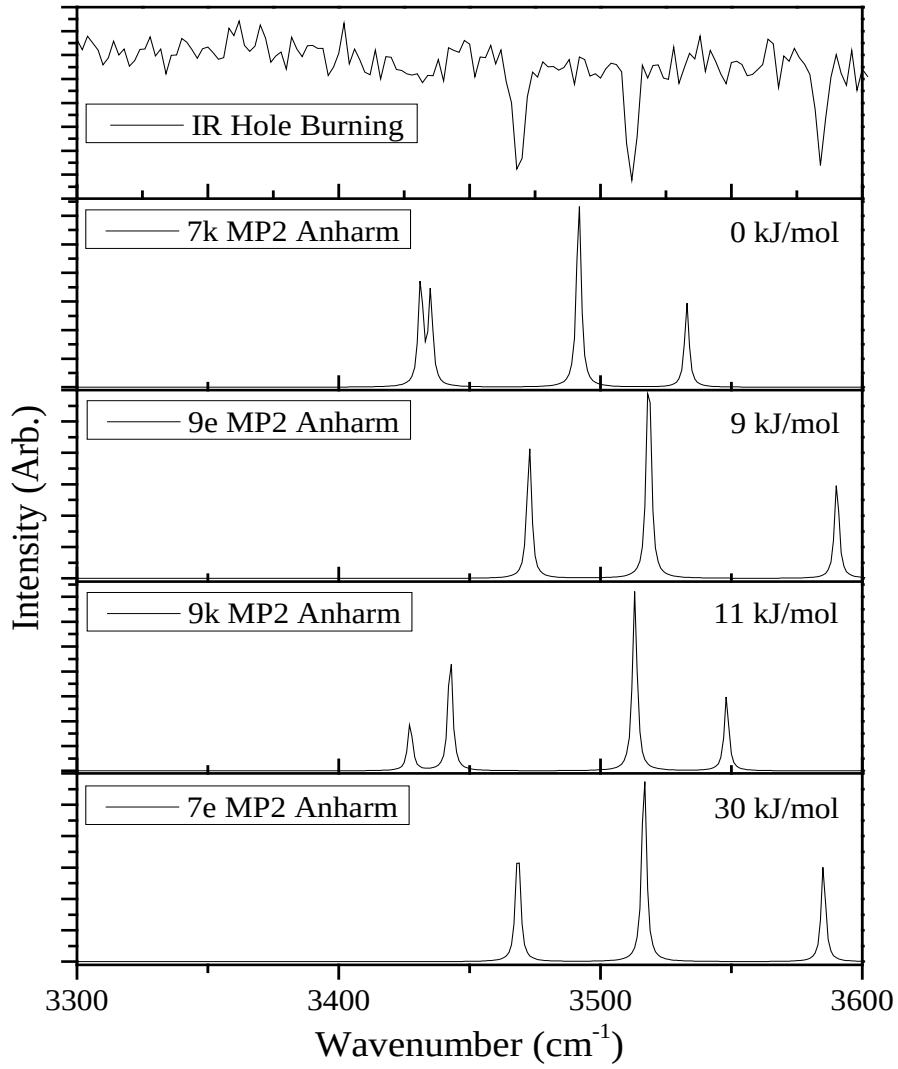

Figure 2. Experimental IR hole burning spectrum in mode I (*top*) and theoretical IR bands calculated at the anharmonic MP2/6-31+G(2d,p) level. Energies shown calculated at CCSD/6-31+G(2d,p).

Figure 2 shows a double resonant spectrum recorded in mode I, with the UV probe laser fixed at 32,343 cm^{-1} together with calculated anharmonic IR frequencies for four different tautomers. Figure 3 shows the optimized structures of the different tautomers. The simulated spectra of both thiol structures fit the experimental spectrum, while none of the thione

spectra fit, which was previously confirmed by Kasende.[57] 6-TG thiones have 2 bands in the red part of the spectrum, whereas only one band is present in the thiols (3,470 cm^{-1}), representing the $(NH_2)_{sym}$ stretch. Moreover, the thione bands do not line up with the experimental data, particularly the highest energy band, the $(NH_2)_{asym}$ stretch, which appears ~50 cm^{-1} lower than the highest frequency measured. The calculated and measured intensities are well matched with the N7H/N9H stretch band at 3,510 cm^{-1}, which is the most intense, followed by the $(NH_2)_{sym}$ stretch at 3,470 cm^{-1} and $(NH_2)_{asym}$ stretch at 3,584 cm^{-1} with nearly identical intensities but slightly more intense at 3,470 cm^{-1}. We did search for the SH stretch which is calculated to be around 2,662 cm^{-1}. However, we did not detect the peak in that region which is most likely due to a weak oscillator strength which is calculated to be less than 10% of the least intense NH/NH_2 peaks.

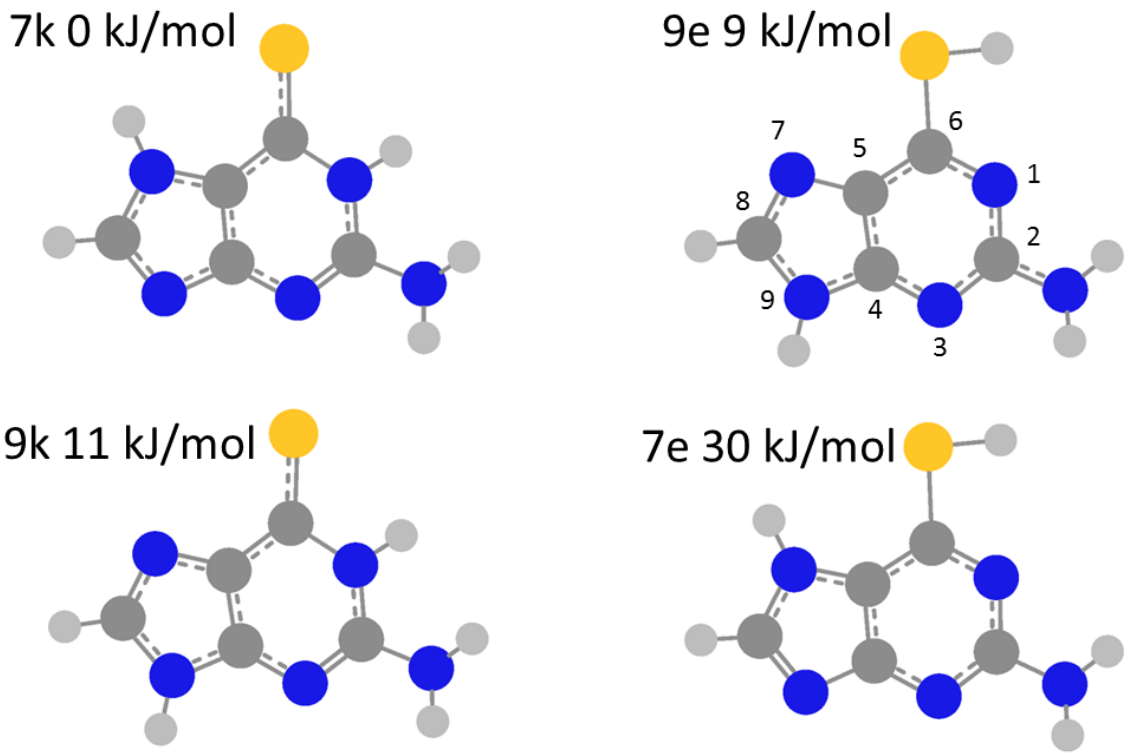

Figure 3. Ground state (Frank-Condon) structures optimized at MP2/6-31+G(2d,p). The atom numbering is shown on the 9e tautomer. Energies shown calculated at CCSD/6-31+G(2d,p).

Vibrational analysis is typically the most direct way of determining which isomers are present in the molecular beam; however, Figure 2 shows that it is difficult to distinguish between 9e and 7e tautomers. As calculated (Figure 3**)** the 9e is ~9 kJ/mol higher in energy than the lowest energy tautomer, and the 7e is ~30 kJ/mol higher in energy than the lowest energy tautomer. Past work in our lab on the nucleobase adenine showed that only the lowest energy isomer was present, where the next lowest energy isomer was calculated to be at ~33 kJ/mol higher energy than the one observed.[58] For this reason, we tentatively assign the UV origin species as 9e. We do not rule out the possibility of 7e or perhaps a 9e-

stereoisomer being present given the ambiguity of their IR spectra. The discussion will proceed focusing on 9e, but keeping these alternatives in consideration.

So far, we have shown that 9e and possibly 7e are the tautomers present when probing at the origin. Typically, UV-UV hole-burning spectroscopy is used to determine the number of tautomers in a REMPI scan; however, the presence of a long-lived dark state, which we discuss below, interferes with this approach. For UV-UV hole-burning to work, the probe laser should only produce ions from the ground state and this signal should be reduced when the ground state is depleted resonantly by the burn laser. However, when the burn laser populates a long-lived dark state, the probe laser can still produce ions indiscriminately from that dark state even at the burn laser resonances. Since it is not practical to perform double resonant spectroscopy in mode I, scanning the IR with the UV wavelength fixed, at each successive UV peak, we performed double resonant spectroscopy in mode II.

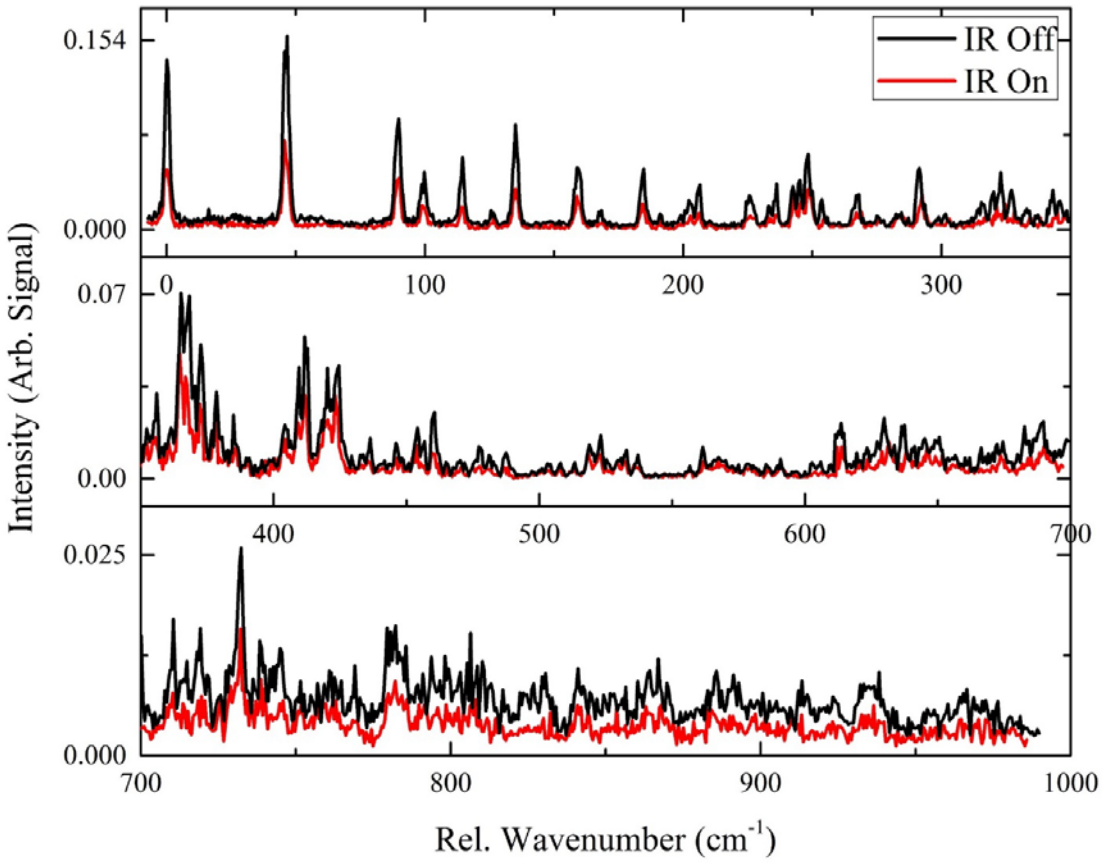

Figure 4. IR laser set to 3,584 cm^{-1} 200 ns prior to scanning UV. Decrease in signal indicates shared IR resonance with the origin transition.

We set the burn laser to 3,584 cm^{-1} 200 ns prior to the UV probe laser which was then scanned to record the IR-UV hole burning spectrum. We chose the $(NH_2)_{asym}$ stretch because it is a good thiol indicator (Figure 2). There is no marker frequency that can distinguish between 7e and 9e tautomers as they share very similar IR spectra. We obtained spectra with IR laser off and IR laser on, where a decrease in signal indicates shared IR resonance with the origin transition and theoretically the same isomer. The result, shown in Figure 4,

indicates that the entire UV spectrum in this range correlates with the same IR marker frequency and thus exclusively with thiol tautomers.

Pump-Probe

6-Thioguanine

In the following discussion, we refer to the UV excitation peaks by their energy relative to the origin at 32,343 cm^{-1}.

Table 1. Summary of fitting parameters where [a] denotes a value from picosecond fit and [b] denotes a value from a nanosecond fit.

Fitting Parameters for 6-Thioguanine				
Excess Energy [cm^{-1}]	**τ_1, ps**	**τ_2, ns**	**τ_{2b}, ns**	**τ_3, ns**
0	481 [a]	6.1 [b]		2025 [b]
47	3920 [ab]			3033 [b]
290	4330 [ab]			2000 [b]
462	577 [a]	5.7 [b]		2590 [b]
679	87 [a]	0.9 [a]	24 [b]	878 [b]
904	168 [a]	1.1 [a]	21.5 [b]	462 [b]

Table 1 lists fitting parameters from the picosecond and nanosecond pump-probe experiments. When fitting the picosecond pump-probe traces, shown in Figure 5**,** all traces except for 47 cm^{-1} and 290 cm^{-1} are fit with a primary decay (τ_1) on the order of hundreds of picoseconds, which populates a secondary state. The lifetime of the secondary state (τ_2) can only be determined within the picosecond data at excess energies greater than 462 cm^{-1} and is of the order of 1 ns. The 47 cm^{-1} and 290 cm^{-1} traces are fit with a single decay of about 4 ns. It cannot be determined on the picosecond timescale whether or not this 4 ns decay fills a

secondary state, so we employ nanosecond timescale experiments to obtain more information.

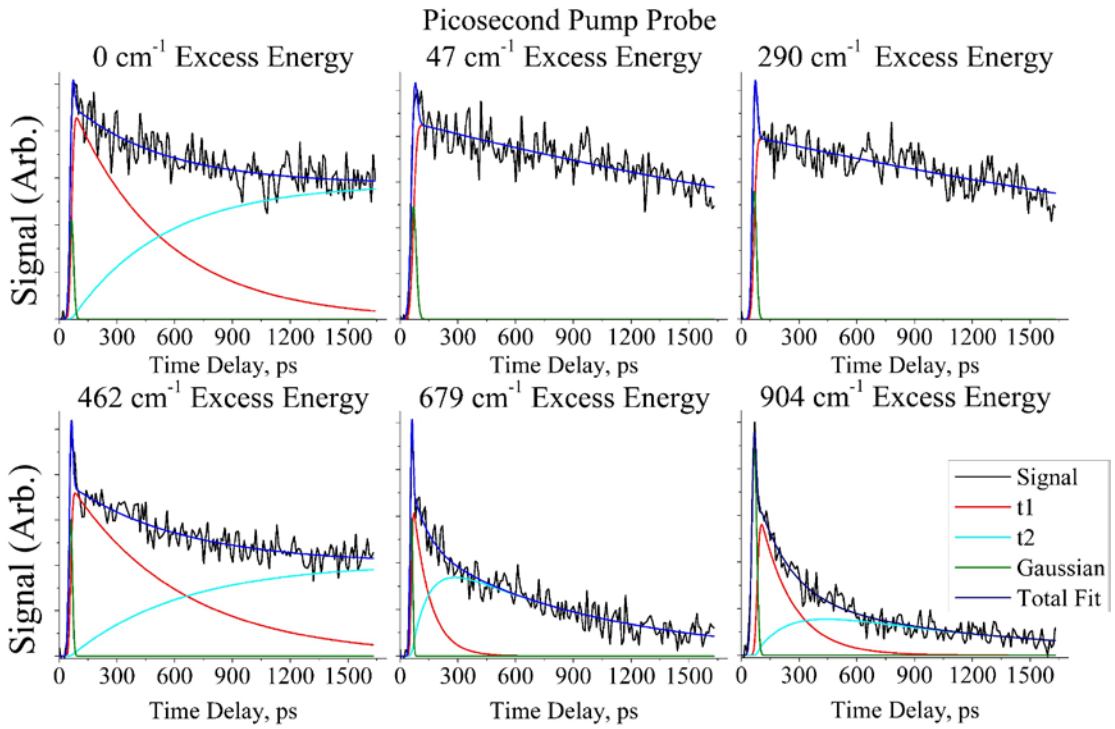

Figure 5: Picosecond pump-probe traces with fitting for 0, 47, 290, 462, 679, and 904 cm^{-1}. Fitting parameters are marked as [a] in Table 1**.**

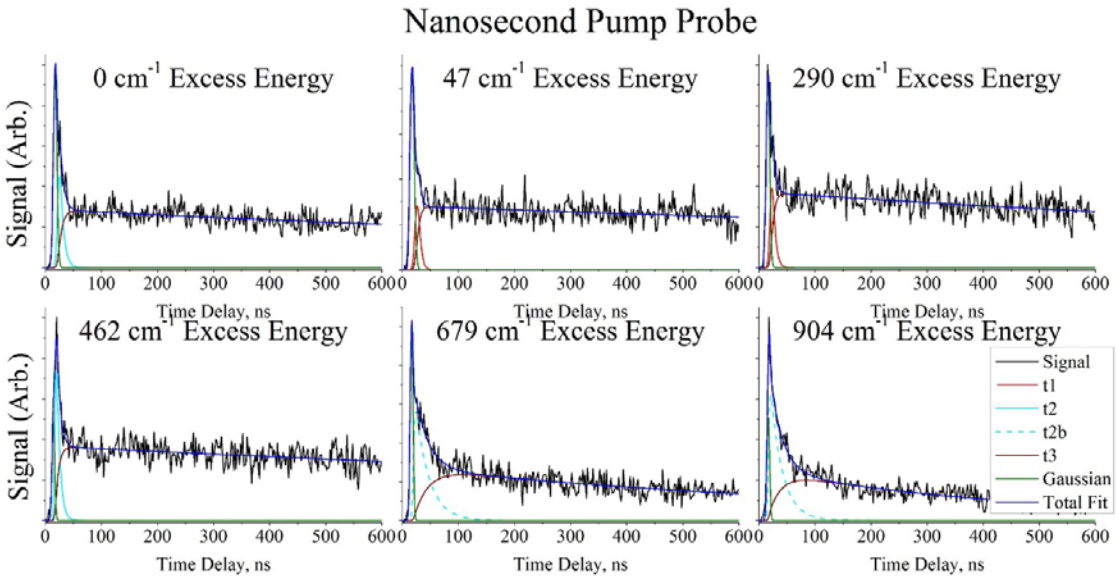

Figure 6. Nanosecond pump-probe traces with fitting for 0, 47, 290, 462, 679, and 904 cm^{-1}. Fitting parameters are marked as [b] in Table 1**.**

The nanosecond lasers are too slow to measure dynamics that occur on shorter timescales, but can be used to fit longer lived pathways. Upon inspection of the nanosecond pump-probe traces (Figure 6**)**, it is evident that a long lived dark state is populated which returns to the ground state on the order of a few microseconds (τ_3). This result suggests the secondary state in the picosecond experiments that decays within single nanoseconds (τ_2) may be a "doorway" state (DS_2) that feeds a long lived "dark" state (DS_1) which is observed in the nanosecond experiment as having the microsecond lifetime τ_3. The nanosecond pump-probe data were fit with primary and secondary decays, however, in this case the primary decay is from DS_2 which decays with time constant τ_2 into DS_1 with a lifetime τ_3. The 1 ns (τ_2) decay from DS_2 for peaks 679 cm^{-1} and 904 cm^{-1} is too fast to be measured by the nanosecond pump-probe, but an additional primary decay of ~20 ns was required to fit the

679 cm^{-1} and 904 cm^{-1} traces, denoted τ_{2b}, implying a double exponential decay to DS_1 at these excess energy levels. The nanosecond (τ_1) component for 47 cm^{-1} and 290 cm^{-1} was fit in both the picosecond and nanosecond traces to within 4% and we report the average value. We assume that for these two excitations the nanosecond decay is from the bright state, not a dark state.

9-enol Guanine

We performed pump-probe experiments on 9e guanine to compare dynamics with 9e-6TG. The excitation wavelength of 32,873 cm^{-1} selects the origin of this tautomer, based on previous results.[41, 59] Measurements in the picosecond range show a flat line, indicating that there are no fast dynamics to capture at that timescale. Supplemental Figure 1 shows the nanosecond trace of the 9e guanine origin revealing two ns lifetime components. One decay path with a 40 ns lifetime feeds a long lived dark state while the other goes directly to the ground state with a 13 ns lifetime. Tautomer selective molecular beam LIF experiments performed by Chin et al. found a 12 ± 2 ns fluorescence lifetime when 9e guanine was excited at its origin.[40] A 50 ns collection window was used in that work and a two-state mixing model $\{S_2,S_1) \rightarrow S_0$ was given to support the broad dispersed fluorescence spectrum. Without a picosecond component to experimentally confirm the $S_2 \rightarrow S_1$ hypothesis we interpret the faster 13 ns decay as fluorescence from the optically bright state. The slower 40 ns decay then feeds a dark state with no fluorescent signature, which could be a $^1n\pi^*$ or a triplet state. In support of the Chin branching model, it is possible that if S_2 is the initially excited state, vibronic equilibration between S_2 and S_1 occurs on a sub-picosecond timescale

leading to fluorescence at rates that are equal or undistinguishable by these experiments. Since in solution guanine exists predominantly in the keto form this is to our knowledge the first observation of such a long lived dark state in enol guanine. If the 13 and 40 ns decays are the only two excited state processes, then the fluorescence quantum yield is about 75%.

Computational Results

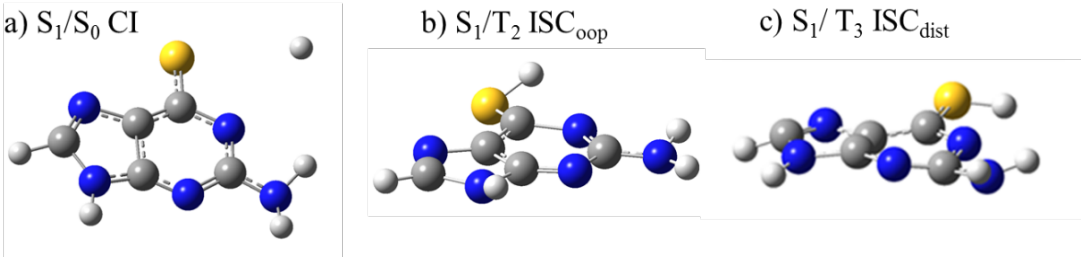

Figure 7. Structures are geometries leading to hops in the SHARC simulation. All structures are calculated at SA-CASSCF(10,10)/6-31G(d) level.

The CCSD energy calculations for the excited states indicate that excitation is to the S_1 state based on oscillator strengths for 9e, 7e 6-TG, and 9e guanine (Supplementary Table 1). This conclusion suggests ruling out the option that τ_1 could be the decay of S_2 to S_1 and instead suggests that τ_1 describes ISC, populating a DS_2 of triplet state character. Such fast ISC can be further explained when combined with information from CASSCF calculations. The 10 SHARC trajectories produce one conical intersection (CI) for S_1/S_0 internal conversion and two relevant intersystem crossing geometries for El-Sayed allowed $S_1(\pi\pi^*)/T_3(n\pi^*)$ and forbidden $S_1(\pi\pi^*)/T_2(\pi\pi^*)$ crossings. The CI involves the loss of the SH hydrogen, where the S_1/T_3 ISC path involves a distortion of the heterocycle (ISC_{dist}), and the S_1/T_2 path corresponds to an out of plane rotation of the thiol group (ISC_{oop}) (Figure 7**)**.

These are preliminary simulations only for the 9e tautomer, consistent with the experimental structural findings described above. We cannot exclude the presence of a second rotamer and of a 7e tautomer so a follow-up comprehensive computational treatment at a higher level will need to also consider those tautomers.

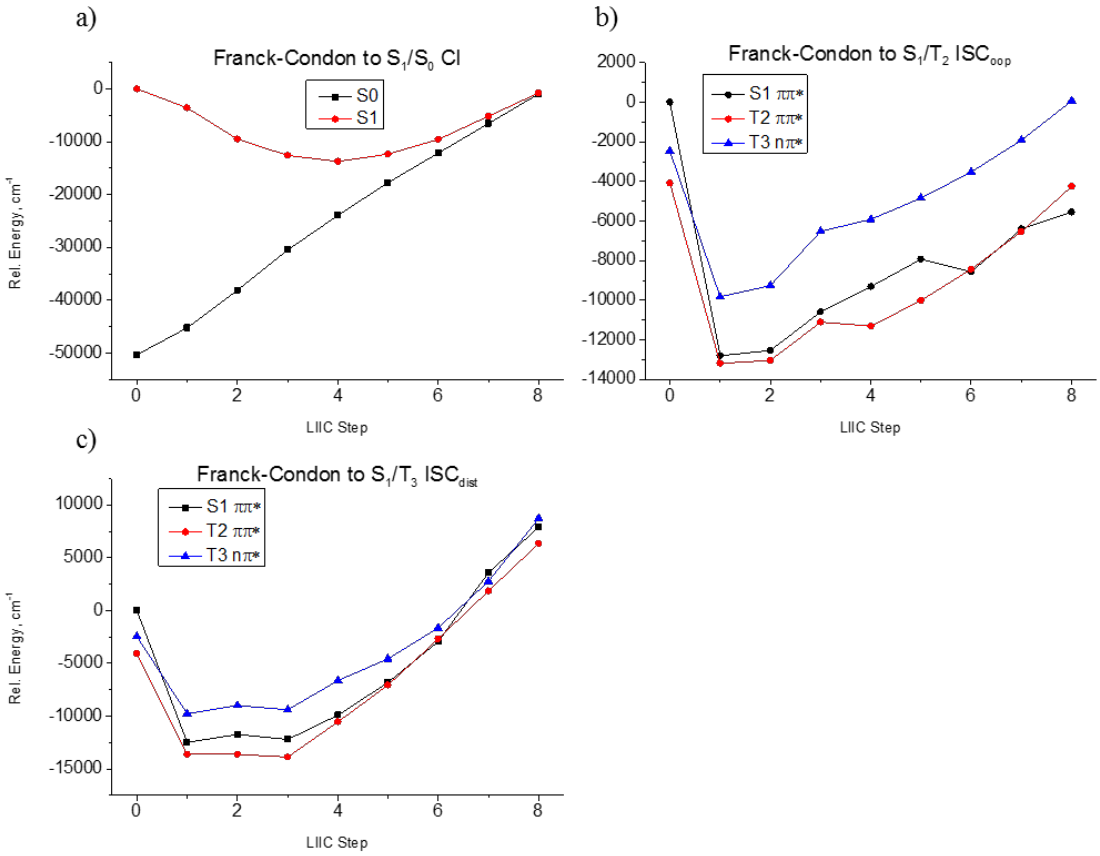

Figure 8. LIIC curves using SA-CASSCF(10,10)/6-31G* from the Frank-Condon geometry to the a) conical intersection, b) ISC path to ISC_{oop}, and c) ISC path to ISC_{dist}

Figure 8a-c shows LIIC plots constructed by stepping the internal coordinates from the FC geometry to the CI/ISC of interest. The path to the CI (Figure 8a) has no barrier, and can be accessed from all excess energies in the FC region. The LIIC for ISC_{oop} (Figure 8b) results in a barrierless path for a S_1/T_2 crossing being located well below the FC region. The

transition is forbidden, but with larger spin orbit coupling due to the sulfur, could be much faster than without it. It also appears that this path results in the singlet and second triplet state being in close proximity, in fact crossing multiple times between the 5^{th} and 8^{th} pathway intervals, which could increase the probability of making the transition at the ISC_{oop} geometry. The ISC_{dist} pathway (Figure 8c) involves a crossing seam which starts around 0 cm^{-1} of excess energy, and extends to nearly 9,000 cm^{-1}. Since this ISC transition is El-Sayed allowed, ultrafast ISC is expected if the crossing is reached which may not be the case considering IVR in the excited state will distribute energy across all modes rather than in the direction of the LIIC.

Like in the LIIC ISC pathway to T_2 (Figure 8b) there are additional crossing points on the potential surface for ISC to T_3 possibly indicating that additional geometries exist for ISC which over the timescale of the SHARC calculations were not populated. It could also be that a greater number of trajectories would yield additional crossing geometries along with statistically significant likelihoods for each. These energy crossings within the LIIC curves may also be artifacts of the level of theory and of plotting a linear interpolation as opposed to a minimum energy pathway.

4. Discussion

Intersystem crossing is typically a slow process due to the required spin flip, but may be ultrafast when spin orbit coupling is large. Increases in spin orbit coupling may happen in various ways, such as a change in symmetry or through the heavy atom effect.[25, 46] We measured excited state lifetimes with increasing excess energy to learn more about possible decay pathways in 6-TG. We performed SHARC simulations initiating in the S_2 state so that

internal conversion to S_1 produces a hot excited state. By performing simulations in this manner, we can find crossing geometries that have an activation barrier, which may be accessed with larger amounts of internal energy.

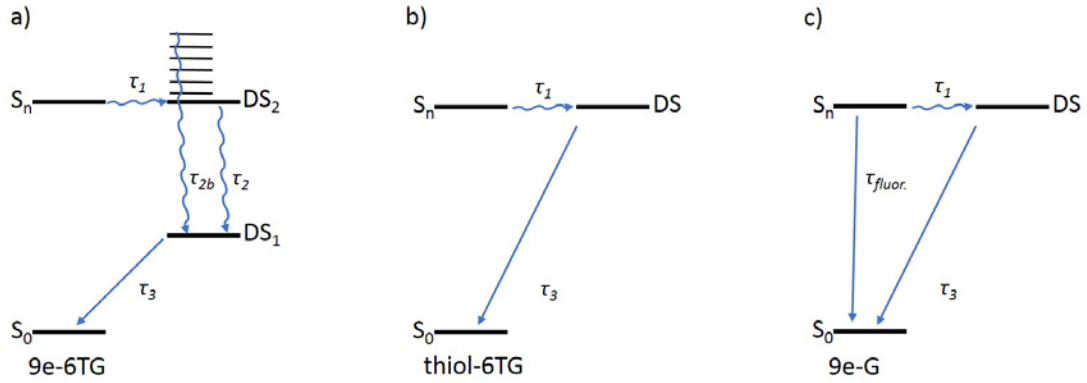

Figure 9. Proposed decay pathways where a) corresponds to traces 0, 462, 679, and 904 cm^{-1} and b) corresponds to traces 47 and 290 cm^{-1} of 6-TG and c) corresponds to the 0 cm^{-1} trace of 9e guanine. S_n is the assumed to be the optically bright state probed by picosecond resolution. DS_2, and S_n of (b) and (c), are assumed to be the initial decay states probed by nanosecond resolution. τ_{2b} has an activation barrier of +679 cm^{-1} (upper limit).

Based on the assumption that excitation of 9e-6TG results in population of S_1, the initial decay can go to either the ground state (IC) or a triplet state (ISC). The picosecond pump-probe data indicates initial decay to a doorway DS_2 state, suggesting that fast ISC is occurring. We do not observe direct decay to the ground state on the timescales of our experiments, suggesting the absence of IC. This result is interesting because Figure 8a shows a conical intersection located below the Frank-Condon region. It may be that IC occurs quicker than the picosecond laser pulse widths, obscuring this pathway in our experiments. Without certainty that all processes are observed we cannot derive quantum yields from the rates, but we can compare observed (τ_1^{-1}) and (τ_2^{-1}) rates with the 40 ns

decay to the long lived dark state of 9e guanine. Here it seems that the sulfur←oxo substitution quenches the 75% fluorescence decay seen in 9H-G_e in favor of total population redistribution to the long-lived excited state in 9e-6TG. Additionally, this long-lived dark state is directly populated in the guanine case but proceeds through a doorway state in 6-TG. This comparison is generalized in Figure 9 cases (a) and (c) for the 6-TG and guanine models respectively.

Figure 9 (a,b) summarizes a tentative interpretation of the pump-probe observations of 9e-6TG with two cases. Case (a) corresponds to excitation at 0, 462, 679, and 904 cm^{-1} and case (b) corresponds to excitation at 47 and 290 cm^{-1}. A possible explanation involving two different relaxation mechanisms is that the excess energy traces included excitations of multiple thiol forms that went unresolved by mode II IR hole burning measurements. Neither the 7e tautomer nor a rotational isomer, about the thiol dihedral coordinate, can be excluded. Alternatively, there may be some vibronic selection criteria which strongly mediate relaxation to either case for 9e-6TG. In these models the first decay τ_1 represents total population transfer from the bright state S_n to DS_2 for (a) and to DS for (b). DS_2 provides a pathway to DS_1 by two measurable decay rates, τ_2^{-1} and τ_{2b}^{-1}. The latter rate, τ_{2b}^{-1}, has an empirical vibronic energy barrier of +679 cm^{-1} (upper limit). Case (a) then decays at τ_3^{-1} from DS_1 to below the ionization potential of our probe laser, into what is likely the ground state of 6-TG. In case (b) τ_1 feeds directly into the long-lived DS, which then decays at τ_3^{-1} on a microsecond timescale. The microsecond relaxation time may lend credence to the identity of DS_1 and DS as triplet states.

A thorough theoretical model is needed to correlate the pump-probe dynamics with specific electronic state identities and trajectory mechanisms. Our preliminary LIIC results provide trends of IC and ISC from the 9e-6TG FC geometry, at the CASSCF level, as initial insight. Figure 8b supports the notion that the S_1/T_2 crossing occurs below the Frank-Condon geometry. Figure 8c shows an S_1/T_3 crossing well above the Frank-Condon geometry with S_1 and T_2 intersecting along this path as well. This suggests that ISC, likened to τ_1, is occurring quickly to T_2 at the energies probed here, and that with even more energy (around +679 cm^{-1}), T_3 may be accessed which would provide access to an El-Sayed allowed transition. In this case T_3/T_2 conversion would be rapid and could yield the τ_2^{-1} and τ_{2b}^{-1} rates seen at higher energies.

5. Conclusion

When comparing the dynamics of the thiol system studied here with the aqueous phase femtosecond study of the thione-nucleoside by Reichardt et al.[43] interpreted by Martínez-Fernández et al.,[30, 44] the rates for ISC are 300-1000 times lower for the thiol. Reichardt also saw internal conversion occurring on the tens of picoseconds timescale, which we do not see in the thiol in the gas phase. In addition to the lack of tautomer selectivity, aqueous phase experiments can produce different results because the solvent affects excited state dynamics by hydrogen bonding and structural changes. Possible ISC lifetimes for 9k and 7k tautomers of 6-thioguanine in the gas phase for comparison are unknown. We demonstrated the effect on ISC of replacing the oxygen in guanine with a sulfur by comparing the pump-probe results of 9e 6-TG with those of 9e guanine. The guanine data correspond to fluorescence lifetimes and a lower decay, possibly ISC, of 13 ns and 40 ns, respectively. At the origin the

rate (τ_1^{-1}) for filling DS_2 in 9e 6-TG is 80 times greater than the decay to the long lived dark state in 9e guanine. Lastly, the presence of an intermediary state (DS_2) is not seen when probing 9e guanine. Higher level computations are needed for a more complete interpretation of the experimental results.

Supporting Information

Singlet and triplet excited state analysis at CCSD/6-31+G(2d,p) for ground state and EOM-CCSD/6-31+G(2d,p) for excited states, nanosecond pump probe trace of 9-enol guanine at its origin.

Acknowledgments

This work was supported by National Aeronautics and Space Administration Grant NNX12AG77G and by the National Science Foundation under CHE-1301305. We acknowledge support from the Center for Scientific Computing from the CNSI, MRL: an NSF MRSEC (DMR-1121053) and NSF CNS-0960316.

References

1. He, Y. G.; Wu, C. Y.; Kong, W. Decay Pathways of Thymine and Methyl-Substituted Uracil and Thymine in the Gas Phase. *J. Phys. Chem. A* **2003,** *107*, 5145-5148.
2. Gengeliczki, Z.; Callahan, M. P.; Svadlenak, N.; Pongor, C. I.; Sztaray, B.; Meerts, L.; Nachtigallova, D.; Hobza, P.; Barbatti, M.; Lischka, H.; de Vries, M. S. Effect of Substituents on the Excited-State Dynamics of the Modified DNA Bases 2,4-Diaminopyrimidine and 2,6-Diaminopurine. *Phys. Chem. Chem. Phys.* **2010,** *12*, 5375-5388.
3. Etinski, M.; Fleig, T.; Marian, C. M. Intersystem Crossing and Characterization of Dark States in the Pyrimidine Nucleobases Uracil, Thymine, and 1-Methylthymine. *J. Phys. Chem. A* **2009,** *113*, 11809-11816.
4. Trachsel, M. A.; Lobsiger, S.; Schar, T.; Leutwyler, S. Low-Lying Excited States and Nonradiative Processes of 9-Methyl-2-Aminopurine. *J. Chem. Phys.* **2014,** *140*, 044331.

5. Kunitski, M.; Nosenko, Y.; Brutschy, B. On the Nature of the Long-Lived "Dark" State of Isolated 1-Methylthymine. *Chemphyschem* **2011,** *12*, 2024-2030.
6. Nir, E.; Kleinermanns, K.; Grace, L.; de Vries, M. S. On the Photochemistry of Purine Nucleobases. *J. Phys. Chem. A* **2001,** *105*, 5106-5110.
7. Malone, R. J.; Miller, A. M.; Kohler, B. Singlet Excited-State Lifetimes of Cytosine Derivatives Measured by Femtosecond Transient Absorption. *Photochem. Photobiol.* **2003,** *77*, 158-164.
8. Trachsel, M. A.; Wiedmer, T.; Blaser, S.; Frey, H. M.; Li, Q.; Ruiz-Barragan, S.; Blancafort, L.; Leutwyler, S. The Excited-State Structure, Vibrations, Lifetimes, and Nonradiative Dynamics of Jet-Cooled 1-Methylcytosine. *J. Chem. Phys.* **2016,** *145*, 134307.
9. Brister, M. M.; Crespo-Hernandez, C. E. Direct Observation of Triplet-State Population Dynamics in the Rna Uracil Derivative 1-Cyclohexyluracil. *J. Phys. Chem. Lett.* **2015,** *6*, 4404-4409.
10. Lobsiger, S.; Frey, H. M.; Leutwyler, S. Supersonic Jet Uv Spectrum and Nonradiative Processes of the Thymine Analogue 5-Methyl-2-Hydroxypyrimidine. *Phys. Chem. Chem. Phys.* **2010,** *12*, 5032-5040.
11. Nachtigallova, D.; Lischka, H.; Szymczak, J. J.; Barbatti, M.; Hobza, P.; Gengeliczki, Z.; Pino, G.; Callahan, M. P.; de Vries, M. S. The Effect of C5 Substitution on the Photochemistry of Uracil. *Phys. Chem. Chem. Phys.* **2010,** *12*, 4924-4933.
12. Pollum, M.; Martínez-Fernández, L.; Crespo-Hernández, C. E. Photochemistry of Nucleic Acid Bases and Their Thio- and Aza-Analogues in Solution. In *Photoinduced Phenomena in Nucleic Acids I: Nucleobases in the Gas Phase and in Solvents*, Barbatti, M.; Borin, A. C.; Ullrich, S., Eds. Springer International Publishing: Cham, **2015**, pp 245-327.
13. Tomic, K.; Tatchen, J.; Marian, C. M. Quantum Chemical Investigation of the Electronic Spectra of the Keto, Enol, and Keto-Imine Tautomers of Cytosine. *J. Phys. Chem. A* **2005,** *109*, 8410-8418.
14. Plutzer, C.; Kleinermanns, K. Tautomers and Electronic States of Jet-Cooled Adenine Investigated by Double Resonance Spectroscopy. *Phys. Chem. Chem. Phys.* **2002,** *4*, 4877-4882.
15. Marian, C. M. The Guanine Tautomer Puzzle: Quantum Chemical Investigation of Ground and Excited States. *J. Phys. Chem. A* **2007,** *111*, 1545-1553.
16. Canuel, C.; Mons, M.; Piuzzi, F.; Tardivel, B.; Dimicoli, I.; Elhanine, M. Excited States Dynamics of DNA and Rna Bases: Characterization of a Stepwise Deactivation Pathway in the Gas Phase. *J. Chem. Phys.* **2005,** *122*, 074316.
17. Nachtigallova, D.; Hobza, P.; Spirko, V. Assigning the Nh Stretches of the Guanine Tautomers Using Adiabatic Separation: Ccsd(T) Benchmark Calculations. *J. Phys. Chem. A* **2008,** *112*, 1854-1856.
18. Seefeld, K.; Brause, R.; Haber, T.; Kleinermanns, K. Imino Tautomers of Gas-Phase Guanine from Mid-Infrared Laser Spectroscopy. *J. Phys. Chem. A* **2007,** *111*, 6217-6221.
19. Mons, M.; Piuzzi, F.; Dimicoli, I.; Gorb, L.; Leszczynski, J. Near-Uv Resonant Two-Photon Ionization Spectroscopy of Gas Phase Guanine: Evidence for the Observation of Three Rare Tautomers. *J. Phys. Chem. A* **2006,** *110*, 10921-10924.

20. Cerny, J.; Spirko, V.; Mons, M.; Hobza, P.; Nachtigallova, D. Theoretical Study of the Ground and Excited States of 7-Methyl Guanine and 9-Methyl Guanine: Comparison with Experiment. *Phys. Chem. Chem. Phys.* **2006,** *8*, 3059-3065.
21. Hare, P. M.; Crespo-Hernandez, C. E.; Kohler, B. Internal Conversion to the Electronic Ground State Occurs Via Two Distinct Pathways for Pyrimidine Bases in Aqueous Solution. *Proc. Natl. Acad. Sci. USA* **2007,** *104*, 435-440.
22. Serrano-Andres, L.; Merchan, M. Are the Five Natural DNA/Rna Base Monomers a Good Choice from Natural Selection? A Photochemical Perspective. *J. Photochem. Photobio., C* **2009,** *10*, 21-32.
23. Yamazaki, S.; Domcke, W.; Sobolewski, A. L. Nonradiative Decay Mechanisms of the Biologically Relevant Tautomer of Guanine. *J. Phys. Chem. A* **2008,** *112*, 11965-11968.
24. Mons, M.; Dimicoli, I.; Piuzzi, F. Isolated Guanine: Tautomerism, Spectroscopy and Excited State Dynamics. In *Radiation Induced Molecular Phenomena in Nucleic Acids: A Comprehensive Theoretical and Experimental Analysis*, Shukla, M. K.; Leszczynski, J., Eds. Springer Netherlands: Dordrecht, **2008**, pp 343-367.
25. Koziar, J. C.; Cowan, D. O. Photochemical Heavy-Atom Effects. *Acc. Chem. Res.* **1978,** *11*, 334-341.
26. Rubin, Y. V.; Blagoi, Y. P.; Bokovoy, V. A. 6-Thioguanine Luminescence Probe to Study DNA and Low-Molecular-Weight Systems. *J. Fluoresc.* **1995,** *5*, 263-272.
27. Ashwood, B.; Jockusch, S.; Crespo-Hernandez, C. E. Excited-State Dynamics of the Thiopurine Prodrug 6-Thioguanine: Can N9-Glycosylation Affect Its Phototoxic Activity? *Molecules* **2017,** *22*.
28. Stewart, M. J.; Leszczynski, J.; Rubin, Y. V.; Blagoi, Y. P. Tautomerism of Thioguanine: From Gas Phase to DNA. *J. Phys. Chem. A* **1997,** *101*, 4753-4760.
29. Yu, H.; Sanchez-Rodriguez, J. A.; Pollum, M.; Crespo-Hernandez, C. E.; Mai, S.; Marquetand, P.; Gonzalez, L.; Ullrich, S. Internal Conversion and Intersystem Crossing Pathways in Uv Excited, Isolated Uracils and Their Implications in Prebiotic Chemistry. *Phys. Chem. Chem. Phys.* **2016,** *18*, 20168-20176.
30. Martinez-Fernandez, L.; Corral, I.; Granucci, G.; Persico, M. Competing Ultrafast Intersystem Crossing and Internal Conversion: A Time Resolved Picture for the Deactivation of 6-Thioguanine. *Chem. Sci.* **2014,** *5*, 1336-1347.
31. Kang, H.; Lee, K. T.; Jung, B.; Ko, Y. J.; Kim, S. K. Intrinsic Lifetimes of the Excited State of DNA and Rna Bases. *J. Am. Chem. Soc.* **2002,** *124*, 12958-12959.
32. Karran, P.; Attard, N. Thiopurines in Current Medical Practice: Molecular Mechanisms and Contributions to Therapy-Related Cancer. *Nat. Rev. Cancer* **2008,** *8*, 24-36.
33. Euvrard , S.; Kanitakis , J.; Claudy , A. Skin Cancers after Organ Transplantation. *N. Engl. J. Med.* **2003,** *348*, 1681-1691.
34. Kaplan, H. S.; Smith, K. C.; Tomlin, P. Radiosensitization of E. Coli by Purine and Pyrimidine Analogues Incorporated in Deoxyribonucleic Acid. *Nature* **1961,** *190*, 794-796.
35. Cuffari, C.; Li, D. Y.; Mahoney, J.; Barnes, Y.; Bayless, T. M. Peripheral Blood Mononuclear Cell DNA 6-Thioguanine Metabolite Levels Correlate with Decreased Interferon-Gamma Production in Patients with Crohn's Disease on Aza Therapy. *Dig. Dis. Sci.* **2004,** *49*, 133-137.
36. Zhang, X. H.; Jeffs, G.; Ren, X. L.; O'Donovan, P.; Montaner, B.; Perrett, C. M.; Karran, P.; Xu, Y. Z. Novel DNA Lesions Generated by the Interaction between Therapeutic Thiopurines and Uva Light. *DNA Repair* **2007,** *6*, 344-354.

37. O'Donovan, P.; Perrett, C. M.; Zhang, X.; Montaner, B.; Xu, Y.-Z.; Harwood, C. A.; McGregor, J. M.; Walker, S. L.; Hanaoka, F.; Karran, P. Azathioprine and Uva Light Generate Mutagenic Oxidative DNA Damage. *Science* **2005,** *309*, 1871-1874.
38. Montaner, B.; O'Donovan, P.; Reelfs, O.; Perrett, C. M.; Zhang, X.; Xu, Y. Z.; Ren, X.; Macpherson, P.; Frith, D.; Karran, P. Reactive Oxygen-Mediated Damage to a Human DNA Replication and Repair Protein. *EMBO Rep* **2007,** *8*, 1074-1079.
39. Attard, N. R.; Karran, P. Uva Photosensitization of Thiopurines and Skin Cancer in Organ Transplant Recipients. *Photochem. Photobiol. Sci.* **2012,** *11*, 62-68.
40. Chin, W.; Mons, M.; Dimicoli, I.; Piuzzi, F.; Tardivel, B.; Elhanine, M. Tautomer Contributions to the near Uv Spectrum of Guanine: Towards a Refined Picture for the Spectroscopy of Purine Molecules. *Euro. Phys. J. D.* **2002,** *20*, 347-355.
41. Nir, E.; Janzen, C.; Imhof, P.; Kleinermanns, K.; de Vries, M. S. Guanine Tautomerism Revealed by Uv-Uv and Ir-Uv Hole Burning Spectroscopy. *J. Chem. Phys.* **2001,** *115*, 4604-4611.
42. Choi, M. Y.; Miller, R. E. Four Tautomers of Isolated Guanine from Infrared Laser Spectroscopy in Helium Nanodroplets. *J. Am. Chem. Soc.* **2006,** *128*, 7320-7328.
43. Reichardt, C.; Guo, C.; Crespo-Hernandez, C. E. Excited-State Dynamics in 6-Thioguanosine from the Femtosecond to Microsecond Time Scale. *J. Phys. Chem. B* **2011,** *115*, 3263-3270.
44. Martinez-Fernandez, L.; Gonzalez, L.; Corral, I. An Ab Initio Mechanism for Efficient Population of Triplet States in Cytotoxic Sulfur Substituted DNA Bases: The Case of 6-Thioguanine. *Chem. Commun.* **2012,** *48*, 2134-2136.
45. Mai, S.; Pollum, M.; Martinez-Fernandez, L.; Dunn, N.; Marquetand, P.; Corral, I.; Crespo-Hernandez, C. E.; Gonzalez, L. The Origin of Efficient Triplet State Population in Sulfur-Substituted Nucleobases. *Nat. Commun.* **2016,** *7*, 13077.
46. El-Sayed, M. A. Spin—Orbit Coupling and the Radiationless Processes in Nitrogen Heterocyclics. *J. Chem. Phys.* **1963,** *38*, 2834-2838.
47. Meijer, G.; Devries, M. S.; Hunziker, H. E.; Wendt, H. R. Laser Desorption Jet-Cooling of Organic-Molecules - Cooling Characteristics and Detection Sensitivity. *Appl. Phys. B.* **1990,** *51*, 395-403.
48. Irimia, D.; Dobrikov, D.; Kortekaas, R.; Voet, H.; van den Ende, D. A.; Groen, W. A.; Janssen, M. H. A Short Pulse (7 Micros Fwhm) and High Repetition Rate (Dc-5 Khz) Cantilever Piezovalve for Pulsed Atomic and Molecular Beams. *Rev. Sci. Instrum.* **2009,** *80*, 113303.
49. Lipert, R. J.; Bermudez, G.; Colson, S. D. Pathways of S1 Decay in Phenol, Indoles, and Water Complexes of Phenol and Indole in a Free Jet Expansion. *J. Phys. Chem.* **1988,** *92*, 3801-3805.
50. Spesyvtsev, R. Experimental Investigation of Ultrafast Internal Conversion in Aniline and 1,4-Diazabicyclo[2.2.2]Octane (Dabco). UCL (University College London), **2013**.
51. Wolfram Research, I. *Mathematica*, 10.0; Wolfram Research, Inc.: Champaign, Illinois, **2014**.
52. Frisch, M. J.; Trucks, G. W.; Schlegel, H. B.; Scuseria, G. E.; Robb, M. A.; Cheeseman, J. R.; Scalmani, G.; Barone, V.; Mennucci, B.; Petersson, G. A.; et al. Gaussian 09, Revision B.01. Wallingford CT, **2009**.
53. Mai, S. R., M.; Ruckenbauer, M.; Oppel, M.; Marquetand, P.; González, L. *Sharc: Surface Hopping Including Arbitrary Couplings – Program Package for Non-Adiabatic Dynamics*, sharc-md.org, **2014**.

54. Richter, M.; Marquetand, P.; González-Vázquez, J.; Sola, I.; González, L. Sharc: Ab Initio Molecular Dynamics with Surface Hopping in the Adiabatic Representation Including Arbitrary Couplings. *J. Chem. Theory Comput.* **2011,** *7*, 1253-1258.
55. Werner, H.-J.; Knowles, P. J.; Knizia, G.; Manby, F. R.; Schütz, M. Molpro: A General-Purpose Quantum Chemistry Program Package. *Wiley Interdisciplinary Reviews: Computational Molecular Science* **2012,** *2*, 242-253.
56. Crespo-Hernandez, C. E.; Martinez-Fernandez, L.; Rauer, C.; Reichardt, C.; Mai, S.; Pollum, M.; Marquetand, P.; Gonzalez, L.; Corral, I. Electronic and Structural Elements That Regulate the Excited-State Dynamics in Purine Nucleobase Derivatives. *J. Am. Chem. Soc.* **2015,** *137*, 4368-4381.
57. Kasende, O. E. Infrared Spectra of 6-Thioguanine Tautomers. An Experimental and Theoretical Approach. *Spectrochim. Acta. Mol. Biomol. Spectrosc.* **2002,** *58*, 1793-1808.
58. Plutzer, C.; Nir, E.; de Vries, M. S.; Kleinermanns, K. Ir-Uv Double-Resonance Spectroscopy of the Nucleobase Adenine. *Phys. Chem. Chem. Phys.* **2001,** *3*, 5466-5469.
59. Nir, E.; Grace, L.; Brauer, B.; de Vries, M. S. Rempi Spectroscopy of Jet-Cooled Guanine. *J. Am. Chem. Soc.* **1999,** *121*, 4896-4897.

II. Photodynamics of Dyes

The work on anthraquinone dyes (Chapter 2.1) was an effort to understand the photostability of these molecules within their historically usage in cultural heritage materials. We focus on the most famous and molecularly simple hydroxyanthraquinones, namely alizarin and purpurin. The concern is that even though these select organic dyes are photostable their natural origin is inhomogeneous so their degradation is unpredictable over many years and makes cultural heritage preservation and restoration difficult. I present a case study that can help us predict relative photo stabilities based on a key structural motif. Connecting the dye excited state dynamics with the nucleobase dynamics is a central theme running between this and the previous chapters.

I. Excited State Intramolecular Proton Transfer in Seven Isolated Hydroxyanthraquinones Depends on Hydrogen Bond Structure

Jacob A. Berenbeim[a], Samuel Boldissar[a], Shawn Owens[a], Faady M. Siouri[a], Michael R. Haggmark[a], Greg Gate[a], Briana Aboulache[a], Trevor Cohen[a], Catherine Schmidt Patterson[b], and Mattanjah S. de Vries[a]*

[a]*Department of Chemistry and Biochemistry, University of California Santa Barabara, CA 93106-9510*

[b]Getty Conservation Institute, 1200 Getty Center Drive, Suite 700, Los Angeles, CA, USA. E-mail: cpatterson@getty.edu; Fax: +1 310 440 7711; Tel: +1 310 440 6232

**E-mail:* devries@chem.ucsb.edu

1. Introduction

Exposure to light can degrade many molecules because absorption of ultraviolet and visible wavelength photons places them in an energetically excited state prone to chemical and physical changes. Molecules which are open to photodegradation are ubiquitous and the undesired effects can be seen everywhere from the disappearance of a particular hue in a museum painting, to the appearance of abnormal cells on one's skin marking melanoma, to the drop of efficiency in polymer solar cells by way of photo-bleaching. On the other hand, certain molecules may be photostable by possessing an excited state pathway, which dissipates energy garnered from photons, to regain a stable ground state structure on a timescale much faster than the reaction rates of degradation.

One such photo protective pathway is excited-state intramolecular proton transfer (ESIPT), and it constitutes one of the quickest reactions known.[1-2] Planar organic molecules that contain acidic and basic functional groups connected by an intramolecular hydrogen bond often have photophysics driven by the transfer of the proton between them. This excited state tautomerization, occurs through the excitation of the ground state enol-form to an electronically excited intermediate where the rapid (often barrierless) enol to keto proton transfer occurs on a sub-picosecond timescale. Radiationless decay and emission follows

bringing the excited keto form back to the ground state, and a barrierless back proton transfer regains the stable ground state enol form.[3] Molecules which undergo ESIPT are typically identified by dual band fluorescence with a large degree of Stokes shift from the ESIPT lower well equilibrium geometry[ref].

Modern applications for ESIPT molecules are plenty, such as fluorophores for biological imaging and microscopy, as well as environmental probes of these systems whereby the hydrophobicity can modulate the Starks shift and relaxation rates[grab refs from intro of serdiuk and roshul 2017].[4] ESIPT molecules that undergo a cis-to-trans twist are currently being investigated as ultrafast molecular switches.[5-6] And there is great interest in using ESIPT molecules as solid state emitters within the optoelectronic device community.[7] Historically ESIPT molecules were used as vibrant colorants in pre-20th century cultural heritage materials (e.g. paintings, dyed textiles, decorated artifacts) as they happened to be the most colorfast. Natural product sources often yielded mixtures of multiple chromophores which non-uniformly fade over time. One of the groups of these molecules are the functionalized anthraquinones (AQs) which are the focus of this study.

Naturally occurring AQs are a diverse group of polycyclic aromatic pigments structurally related to 9,10-dioxoanthracene that occur in plants, lichens, insects, and fungi as pigments across the entire visible spectrum.[8-11] While commercial interest has veered from chromic to pharmaceutical application,[12-14] past use of natural AQ derivatives as photostable Lake dyes (insoluble dye-mordant complexes, typical Al or Ca cation coordinated) attracted attention of fine artists and tradesmen over the centuries.[15-16] One of the simplest and possibly the most notorious AQ is 1,2-dihydroxyanthraquinone (1,2-dhaq),

known as alizarin. Alizarin is naturally produced by multiple species related to *Rubia tinctorum* (common madder) where it is a primary chromophore along with 1,2,4-thaq, known as purpurin. It is well documented that alizarin is more photostable than purpurin, in the cultural heritage community,[17-20] and in the condensed phase scientific community,[16, 21] however, neither molecule's photodynamics have been studied in the gas phase.

Formative work was done in the 1980s with laser induced fluorescent spectroscopy[22-25] to study these AQs/HAQs predisposition towards dual fluorescence and Flom and Barbara[3] determined that the presence of a 1,4- electron donating group (e.g. -OH) precludes dual fluorescence likely indicating a high barrier towards ESIPT. This qualitative result was later supported by the nodal-plain model by Nagaota.[26] More recent transient spectroscopic work has been done to measure the rate of ESIPT[27-31] as a femtosecond process and to correlate this with pigment fading[21, 32-33] however these are all condensed phase experiments which fail to measure the unimolecular dynamics of the AQ/HAQ molecules when intermolecular effects are widely known to affect relaxation.[30, 34]

In this paper, we report an experimental case study on the effects of intramolecular hydrogen bond structure on excited state lifetime of seven HAQs. We measure and compare intrinsic lifetimes of neutral HAQ molecules in a jet-cooled molecular beam by time resolved, pump-probe, two- color (2C) resonant two-photon ionization (R2PI) spectroscopy and time-of-flight ion resolution and detection. In this way, these molecules are prepared cold (10-20 K) and isolated from intermolecular interactions so we can interpret relaxation dynamics occurring at the lower limit of the excited state potential energy surface. Given the number of molecules in this study we present the following collection of data: 1) VIS

spectra in the form of 2C R2PI action spectra, 2) a two-point snapshot of excited state lifetimes from the lowest energy vibronic transition and one at higher internal energy (~500-1000 cm^{-1}) for each compound, and partial mid-IR characterization of the ground state hydrogen bond vibrations with IR hole burning of the R2PI probe signal. Our results show a trend of shorter excited state lifetimes for the structures with evidence for ESIPT, as derived from dual fluorescence by Flom and Barbara and others. Both phenomena correlate with structural motifs with specific hydrogen bonding patterns.

2. Methods

Experimental

We purchased standards of all seven HAQs from Sigma-Aldrich and used them without further purification. Standards are directly applied to graphite sample bars as a thin solid layer. All spectra were collected using separate graphite bars to ensure each spectrum is free of any other standards.

The instrument has been previously described in detail and only a brief description of the experimental setup follows.[35-36] Samples are laser desorbed in vacuo (4 x 10^{-6} Torr source chamber pressure) directly in front of a pulsed molecular beam controlled by a piezo cantilever valve.[37] Our desorption laser is a tightly focused Nd:YAG laser (1064 nm, ~ 0.1 mJ cm^2) and the piezo cantilever valve operates at a 45 usec pulse duration with 8 bars backing argon gas. The desorbed sample is adiabatically cooled by collisions with the argon jet-expansion to between 10-20 K and the molecular beam is skimmed before being

intersected by laser beams and photo-ionized. We implement two-color resonant two photon ionization (2C-R2PI). The subsequent ions are detected by a reflectron time of flight mass spectrometer (2 x 10^{-6} Torr analyzer pressure, mass resolution m/Δm=500).

The 2C-R2PI spectroscopic and picosecond (ps) pump-probe delay measurements are performed with an Ekspla PL2251 Nd:YAG laser system producing ~ 30 ps laser pulses. The 355 nm output pumps an Ekspla PG401 tunable optical parametric generator (OPG) (VIS output of 450-600 uJ/pulse, UV output of 80-120 μJ/pulse, ~ 6 cm^{-1} spectral linewidth). The sample is excited by the OPG and ionized by 213 nm, fifth harmonic of the Ekspla PL2251 laser, which is mechanically delayed up to 600 ps before colineation with the OPG beam. A variable electronic (SRS DG645) delay between OPG UV laser and an excimer laser (193 nm, 1.5-2 mJ/pulse) is used for pump-probe measurements in the nanosecond (ns) time delay range.

For IR-UV double resonant spectroscopy a Laser Vision optical parametric oscillator/amplifier (OPA/OPA) (mid-IR output over the range 3,000-3,600 cm^{-1} of ~3-5 mJ/pulse, 3 cm^{-1} spectral linewidth) precedes the REMPI by 200 ns. We perform double resonant spectroscopy with two different pulse sequences in this report: in mode I we scan the IR at a fixed UV probe wavelength and in mode II we scan the UV with a fixed IR burn wavelength. In mode I the IR laser is scanned while the UV laser is fixed on one vibronic transition and signal depletes when the IR laser becomes resonant with that ground state population. The resulting ion-dip spectrum represents the ground state IR spectrum of a single tautomer, selected by the UV probe wavelength. This IR spectrum can be compared with calculated IR frequencies to determine the specific tautomer of the selected vibronic

transition. In mode II the IR laser is set to a tautomer-specific vibrational resonance and we scan the UV laser, comparing spectra with IR laser on and off. The difference spectrum identifies peaks in the UV spectrum that arise from the same tautomer.

Calculations

All calculations were performed with the Gaussian 09 program package.[38] Starting structures for hydroxy derivatized anthracine-9,10-dione (HAQ) structures, tautomer and rotamer isomers, were optimized using the B3LYP hybrid functional with CC-pVTZ basis set. Relative zero- point corrected energy (ZPE) values are used to predict the number of isomers in our molecular beam based on the rule of thumb that for a given species isomers up to 20 kJ/mol of the lowest energy structure are typically kinetically trapped laser desorption jet-expansion. Past work in our lab on the nucleobase adenine showed that only the lowest energy isomer was present, where the next lowest energy isomer was calculated to be at ~33 kJ/mol higher energy than the one observed.[39] Ground state minima were confirmed by the absence of imaginary frequencies and these geometries later used to determine electronic transition state strengths for S1-4 by way of TD-DFT with the B3LYP hybrid functional with CC-pVTZ basis set. The simulated IR spectra arise from frequencies with harmonic intensities using a Lorentzian shape and FWHM of 3 cm^{-1} and are presented without a spectral shift.

3. Results

Isomer ZPE Calculations

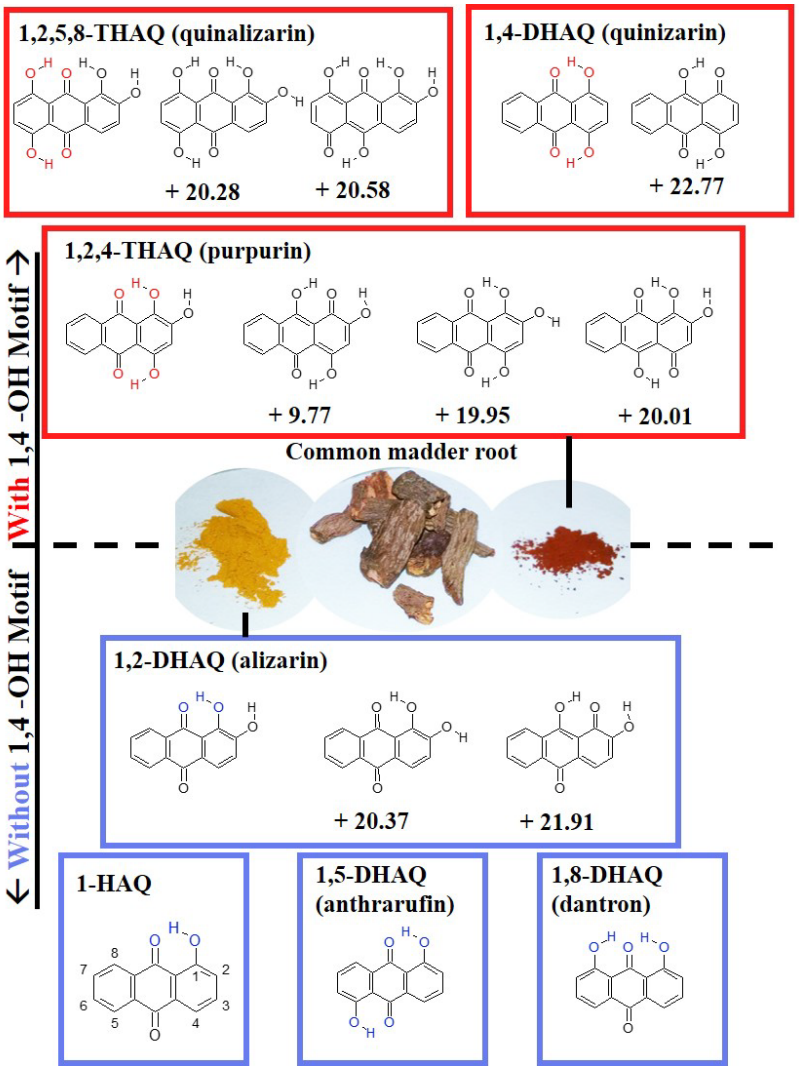

Figure 5 The molecules of this study arranged as those having a 1,4 -OH motif above the dotted line and without 1,4 -OH motif below. Isomers shown are within ~20 kJ/mol of the lowest energy (LE) ZPE corrected structure are include relative energy values (kJ/mol) with respect to the lowest energy form. Central to this figure is the common madder root and its primary chromophores alizarin and purpurin.

The molecular structures shown in Figure 1 are planar in all cases and the lowest energy (LE) structure is of the 9,10-anthraquinone form. The isomers above are shown because they may exist isolated in the conditions of a cold molecular expansion based on their relative energy value. Centrally located in the above figure are the primary *common madder* chromophores 1,2-dhaq, and 1,2,4-thaq. Both have multiple low energy isomers as do

1,2,5,8-thaq and 1,4-dhaq. 1-haq, 1,5-dhaq, and 1,8-dhaq all have a single lowest energy structure (the rotamers for each of these molecules lay 52.3, 53.2, and 47.4 kJ/mol higher in energy respectively).

R2PI of n-hydroxy anthraquinones with 1,4-Motif

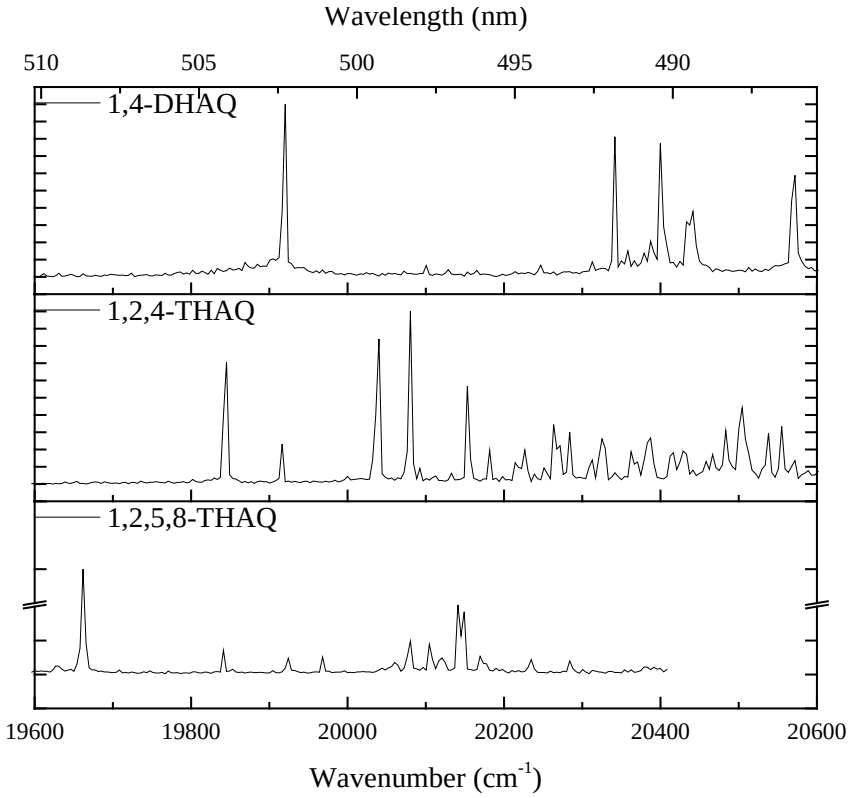

Figure 6 2C-R2PI Spectrum of each HAQ that contains the 1,4-dihydroxy substitution. Intensities have been scaled to 1 and are plotted in arbitrary intensity units (0.1 tick marks). The intensity scale on the bottommost spectrum has been truncated between .2-.95 in order to show the majority of the features which were low in relative intensity.

Figure 2 shows the R2PI spectra of the substituted anthraquinone derivatives containing 1,4 -OH motif substitution; 1,2,5,8-THAQ at 19,661 cm^{-1}, followed by 1,2,4-THAQ at 19,845 cm^{-1}, and 1,4-DHAQ at 19,920 cm^{-1}. Their origins are all within 300 cm^{-1} of each other and sharp laser linewidth limited bands define each trace over ~ 1000 cm^{-1}.

R2PI of n-hydroxy anthraquinones without 1,4-Motif

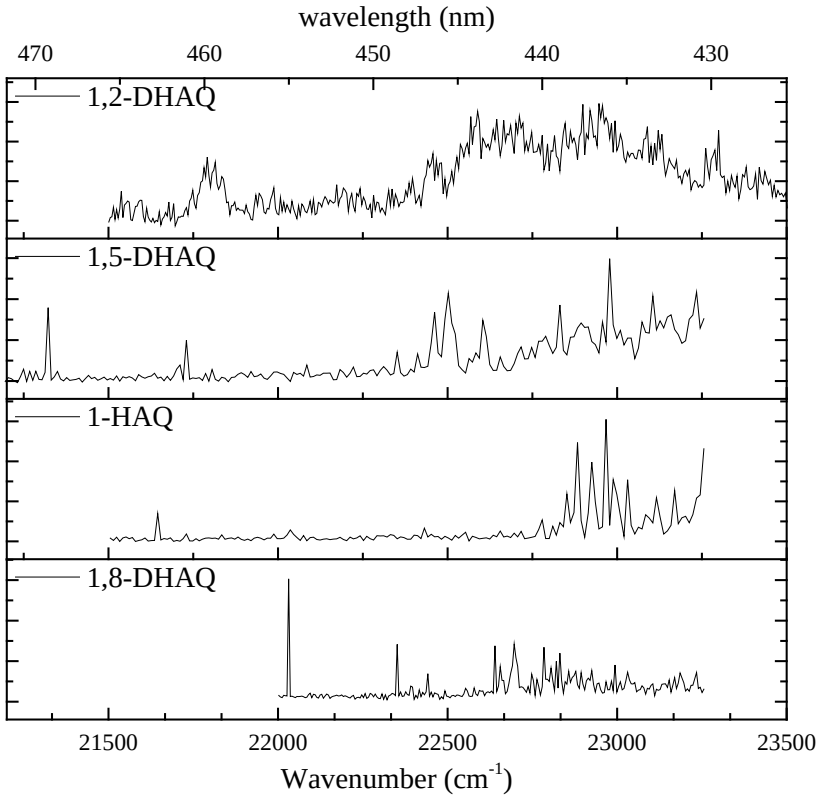

Figure 7 2C-R2PI of each labeled HAQ which did not contain the 1,4 substitution motif. Intensities have been scaled to 1 and are plotted in arbitrary intensity units.

Figure 3 shows the R2PI spectra of the substituted anthraquinone derivatives not containing 1,4 -OH motif substitution; 1,2-DHAQ at 21,748 cm^{-1}, 1,5-DHAQ at 21,321 cm^{-1}, 1-HAQ at 21,645 cm^{-1}, and 1,8-DHAQ at 22,031 cm^{-1}. The origins are at an average 2,000 cm^{-1} higher energy than those of the 1,4 type compounds. The 1,2-DHAQ spectrum is notably broad. All spectra in figures 2 and 3 are normalized to their respective maxima but the signal generating the spectra of Figure 2 was significantly larger than that of the spectra in Figure 3.

Intramolecular Hydrogen Bonding Characterization and Structural Confirmation

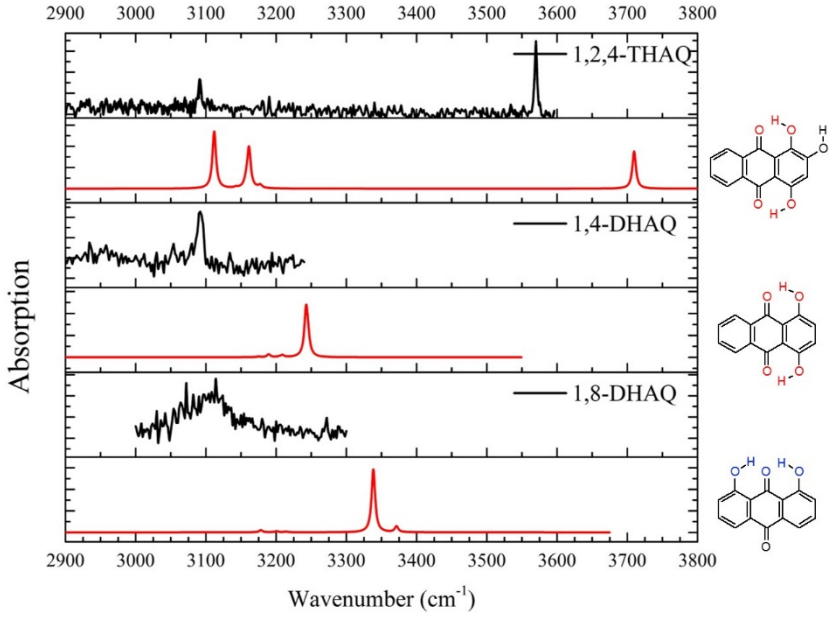

Figure 4 IR hole burning spectra (in black) taken in mode I of 1,2,4-thaq, 1,4-dhaq, and 1,8-dhaq probed at their lowest energy R2PI transition. The ground state predicted frequencies for the given LE structure are plotted below each hole burn spectrum (in red). Harmonic analysis is shown unshifted.

In order to understand the hydrogen bonding environment of the LE ground state species we performed IR hole burning in Mode 1 on 1,2,4-thaq, 1,4-dhaq, and 1,8-dhaq while probing the vibrationless transition of each. The experimental spectra are shown in Figure 4 for direct comparison with the LE predicted spectrum plotted with a linewidth of 3 cm^{-1}.All have been separately plotted against all lowest energy structure predictions and presented in Supplemental Information (Figures S.4-6 respectively).

For both 1,4-dhaq and 1,8-dhaq, the stretch at ~3,100 cm^{-1} represents stretching modes associated with the -OH hydrogen bound to a carbonyl group. In the former case, the narrow line width is due to a single intramolecular hydrogen bound carbonyl, and the latter is broadened by the competitive sharing of the carbonyl with intramolecular hydrogen bonds 180° about the oxygen atom (9-position). The harmonic vibrational analysis for both

DHAQs predicted this stretch to be 150-250 cm^{-1} higher in energy. The concerted symmetric and asymmetric -OH stretches are resolved in the predicted case of 1,8-dhaq but unresolved in 1,4-dhaq due to the splitting being lower than the chosen linewidth, thus these stretching modes appear as a single peak for 1,4-dhaq. For the 1,2,4-thaq spectrum we only resolve two of the three predicted features associated with the LE structure. The high-energy feature at 3,570 cm^{-1} is the in-plane hydroxyl (2-position) which is hydrogen bound to the neighboring hydroxyl(1-position). The 470 cm^{-1} separation is a direct measurement of different hydrogen bond environments: between carbonyl and hydroxy intramolecular bonded -OH stretches.

It appears our level of harmonic analysis may be ineffectively predicting the splitting between the carbonyl bound -OH stretches on 1,2,4-thaq, in this case with a high bias (overly splitting) treating these as individual motions rather than concerted, as in the dhaq examples. The peak width of the 3,570 cm^{-1} (2-position -OH) mode is ~4 cm^{-1} while the stretch near 3,100 cm^{-1} is ~7 cm^{-1}. In the case of 1,4-dhaq the width was 10 cm^{-1}. This experimental evidence suggests we may have the LE form of 1,2,4-thaq with unresolved carbonyl bound -OH modes, much like the 1,4-dhaq case. Additionally, the predicted spectrum of the LE rotamer, where the 2-position -OH rotates such to break the intramolecular hydrogen bond, is invariant with respect to the splitting of the carbonyl bound -OH modes relative to the LE predicted spectrum. This supports the notion that the B3LYP functional ought not to be used in further analysis of these HAQs.

IR-UV results takin in mode II that indicate 1,2,4-thaq and 1,4-dhaq R2PI results are from a single confirmation (see Supplemental Information Figure S.7).

Pump-Probe Results

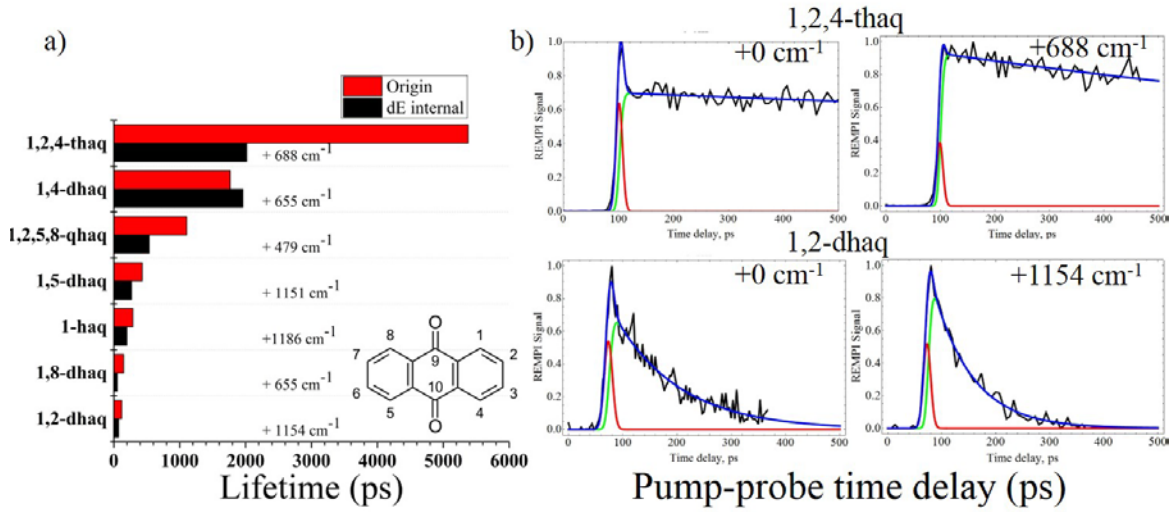

Figure 5 a) Pump-probe lifetime results taken at the 0_0^0 transition (red) and at excess energy (black) are arranged in order of decreasing measured lifetimes. b) Pump-probe traces of the molecules with the longest and shortest measured excited state lifetime, 1,2,4-thaq and 1,2-dhaq respectively, plotted over 500 ps. The pump-probe data are fit to a curve (blue) which is the sum of a single exponential decay convolved with a Gaussian component (red) representative of our instrument response function (IRF) and the IRF itself (green).

We performed ps pump-probe measurements on the origin transition and one additional higher energy transition for each HAQ from Figure 1. The bar graph in Figure 5 highlights the effect of structure on relaxation lifetime. The molecules with the 1,4 -OH motif have ns lifetimes at their lowest energy transitions while those without the 1,4 -OH motif have ps lifetimes. Coincidently the primary madder chromophores have the longest and the shortest excited state lifetimes of all molecules measured; probed at the origin 1,2,4-thaq (purpurin) has an excited state lifetime of 5.4 ns and 1,2-dhaq (alizarin) has an excited state lifetime of 120 ps. By comparison, 1-haq has a measured lifetime of 290 ps while 1,4-dhaq has a measured lifetime of 1.7 ns. We were unable to record R2PI signal from 2-haq to probe its lifetime for this comparison.

The right side of Figure 5 shows the ps pump-probe data for 1,2,4-thaq and 1,2-dhaq. For tabulated lifetime values, ns pump-probe data for 1,2,4-thaq and 1,4-dhaq, and remaining ps pump-probe data see Supplemental Information (Table S.7). Excitation at higher energies shortens the lifetime. This trend holds for the data shown in Figure 5 with the exception of 1,4-dhaq with a slight increase in excited state lifetime at +655 cm^{-1} (1.7 ns to 1.9 ns).

We also performed ns pump-probe measurements on 1,2,4-thaq and 1,2-dhaq (shown in Figure S.3) and found no component at longer time scale than those found in the ps measurements.

4. Discussion

We consider the 1-haq and 1,4-dhaq structural motifs as the major distinguishing factor affecting relaxation dynamics. When interpreting spectral and pump-probe results it is important to keep in mind that multiple tautomeric forms are possible as shown in Figure 1. Generally, in jet-cooling conditions only the lowest energy forms exist and the mode II IR-UV data for 1,24-thq and 1,4-dhaq suggest those data to be exclusively from a single tautomer (though possible from either LE or its complimentary rotamer in Figure 1). Absent further IR-UV data we assume the other compounds also to be exclusively or at least predominantly in the lowest energy form but the possible existence of other tautomers in the beam cannot be discarded.

The results have been consolidated in Supplemental Information (Table S.1) to aid discussion where we have included the excitation level selection criteria. The trend is that relative to the 1-OH motif there is a 15x average longer lifetime for the molecular species with the 1,4-OH motif.

In the cases where ESIPT occurs, as evidence by dual fluorescence (not performed here), the pump-probe results would originate from two excited state populations, as this process equilibrates on the femtosecond timescale which is well below the IRF of our 30 ps laser pulse width. All the data shown in Figure 5 originated from single exponential decay fits, suggesting either very high quantum yields of the one state or indistinguishable relaxation rates (immeasurable or identical). There are three arguments why the latter explanation seems unlikely. 1) Not all R2PI scans could be collected with a ns ionization source, specifically not 1,2-dhaq, which argues against the existence of a long-lived excited state population. 2) 1,2,4-thaq and 1,2-dhaq have single ns lifetimes confirmed with both ns and ps pump-probe measurement and have no longer lived component. This suggests that the excited state non-proton transfer (non-PT) geometries, which are vibrationally cold relative to ESIPT driven ones, in this case study relax on the single ns timescale still measurable by ps pump-probe. Therefore, in the case of these similar molecules with lifetimes measurable solely by ps pump-probe we ought to be capable of measuring ps and ns decays simultaneously. 3) As for PT and non-PT geometries relaxing at identical rates, only concerted rigorous excited state theoretical studies can confirm this trend but a vibrationless non-PT form versus a vibrationally hot PT form relaxing at identical rates does not seem practical.

Approximate Excited State Relaxation Geometry

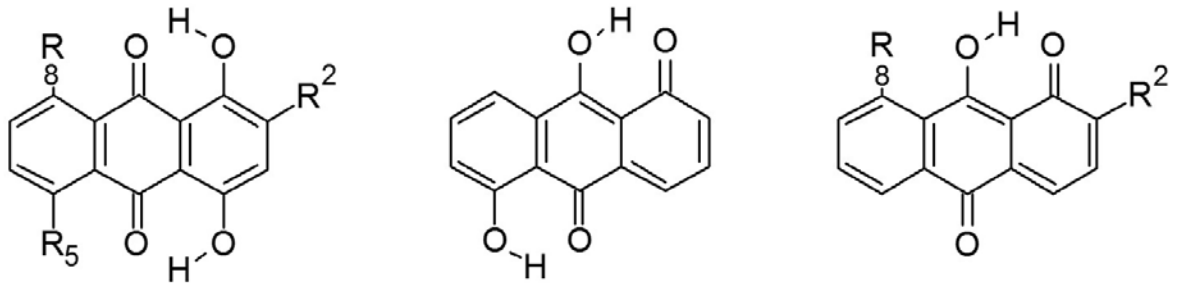

Lifetime > 1 ns	R2	R5	R8	Lifetime 430 ps	Lifetime < 290 ps	R2	R5	R8
1,2,4-thaq	OH	H	H	1,5-dhaq	1-haq*	H	H	H
1,4-dhaq	H	H	H		1,8-dhaq*	H	H	OH
1,2,5,8-qhaq	OH	OH	OH		1,2-dhaq	OH	H	H

Figure 6 Approximate Excited State Relaxation Geometries and their associated lifetimes. All cases are predicted to relax from an S1←S0 transition except for those starred (*) which are predicted to be from S2←S0 by TD-DFT calculations using the B3LYP functional and a CC-pVTZ basis performed from the S0 optimized geometry.

In the absence of a theoretical explanation for relaxation pathways we present a visual comparison of HAQs organized by approximate excited state structure and lifetime, shown in Figure 6. Here we show that upon excitation and a propensity towards ESIPT these molecules can adopt three distinct aromatic structures: those without PT on the left adopt a geometry with planar C_2 carbonyl symmetry; those in the center and rightmost columns relax from PT geometries. Since we record single lifetimes for all HAQs and previous studies on these molecules observed fluorescence, we interpret the inverse of these lifetimes as rates of fluorescence. Without knowing the internal energy difference between PT and non-PT emissive geometries it is unclear what effect internal vibration redistribution (IVR) following the ESIPT may have on increasing the rate of fluorescence and whether any IC pathways exist for PT relaxation. The internal energy barrier where IVR begins to blur

elucidation of individual decay pathways is unclear and highly dependent on the available normal modes.[40-41] But IC pathways could be due to the differences in molecular rigidity that could arise from an aromatic superstructure between that of the anthracene moiety and the one created by intramolecular hydrogen bonds in the 1,4 motif (structures in the left column of Figure 6), as compared to the "diagonalized" arrangement of hydrogen bonds in the center column, and the largely asymmetric hydrogen bond pattern for the HAQs in the right column. It may be that breaking of this aromatic superstructure allows for increased out-of-plane vibrational motion, such as that of a hydrogen bond stretch, key to many internal conversion geometries responsible for nonradiative deactivation.[42]

We also comment on the lack of triplet state formation here which has been reported in high quantum yield by Mohamed et al. in a study of 1,8-DHAQ in a series of nonpolar, polar aprotic, and polar protic solvents. When the solvent was able to break the intramolecular proton bond in the excited state, the formation of an long lived triplet state occurred.[30] Our results support this notion.

The photobleaching effects of *common madder* chromophores, 1,2,4-thaq and 1,2-dhaq, was recently investigated by Tan et al. by counting emissive events in time (photo-blinking) of these dyes under inert (N_2) irradiant conditions on glass. They measured that 1,2-dhaq is able to absorb and emit 4 times longer (and over many more events) than purpurin, which they argue to be due to a long lived excited state which degrades through electron injection to the glass slide.[21] This decay pathway is consistent with the literature.[27, 31, 43] One cannot compare absolute lifetime values between gas phase and condensed phase states but the trend in the condensed phase correlates with of the inherent lifetime trends presented here (that alizarin is ~ 45 times shorter lived at its vibrationless transition than is natural *common madder* companion. Taken with the body of work done on UV radiation on anthracene by

Mallakin on the production of toxic species (i.e. reactive, typically $^1O_2$) through the stepwise formation and further irradiation of AQs and HAQs[44-45] and the work by Nagaoka et. al on the quenching of singlet oxygen ($^1O_2$) by ESIPT HAQs a complicated picture begins to form in the degradation of the madder colorants in cultural heritage materials. It may be possible that due to its longer lifetime, purpurin can transfer the energy of its electronic transition to a reactive species, either a mordant metal or in formation of a reactive oxygen species which the PT excited structure can efficiently quench.

5. Conclusion

The experimental results support the idea that there is increased photostability for those HAQ dyes that lack the 1,4 -OH motif. When comparing the relaxation from the lowest energy vibrionic transition, where the internal energy of the excited state molecule is at its lowest, there is more than an order of magnitude difference in relaxation rates.

This relative difference is significantly large and begs the question what characteristics the excited state potential surfaces have in common that give rise to such a general structural trend. Excited state computational work is needed to understand what processes are at play. In addition, further experimentation on the isotopic effects of deuterating the proton in transfer can help experimentally define the ESIPT process, which may of course help with excited state computational modelling.

Acknowledgements:

This work was supported by National Aeronautics and Space Administration Grant NNX12AG77G and by the National Science Foundation under CHE-1301305. We acknowledge support from the Center for Scientific Computing from the CNSI, MRL: an NSF MRSEC (DMR-1121053) and NSF CNS-0960316.

Supplemental Information

Nanosecond and picosecond pump-probe spectra for remaining HAQs and IR hole burning spectra for 1,4-DHAQ and 1,2,4-THAQ in mode II, theoretical comparisons for mode I results, and electronic transition strengths from S1-S4 for HAQs.

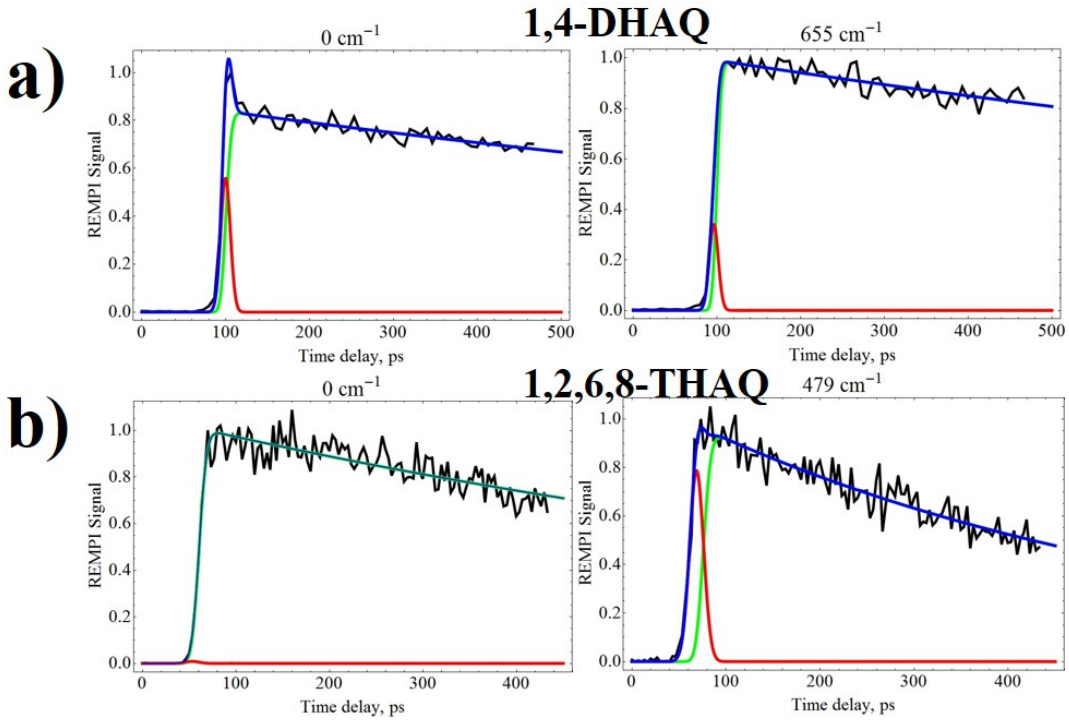

Figure S.1 ps pump-probe spectra for a) 1,4-DHAQ at vibrationless and excess probe lengths and b) 1,2,6,8-THAQ at vibrationless and excess probe lengths. All lifetime values are listed in Table 1. The pump-probe data are fit to a curve (blue) which is the sum of a single exponential decay convolved with a Gaussian component (red) representative of our instrument response function (IRF) the IRF itself (green).

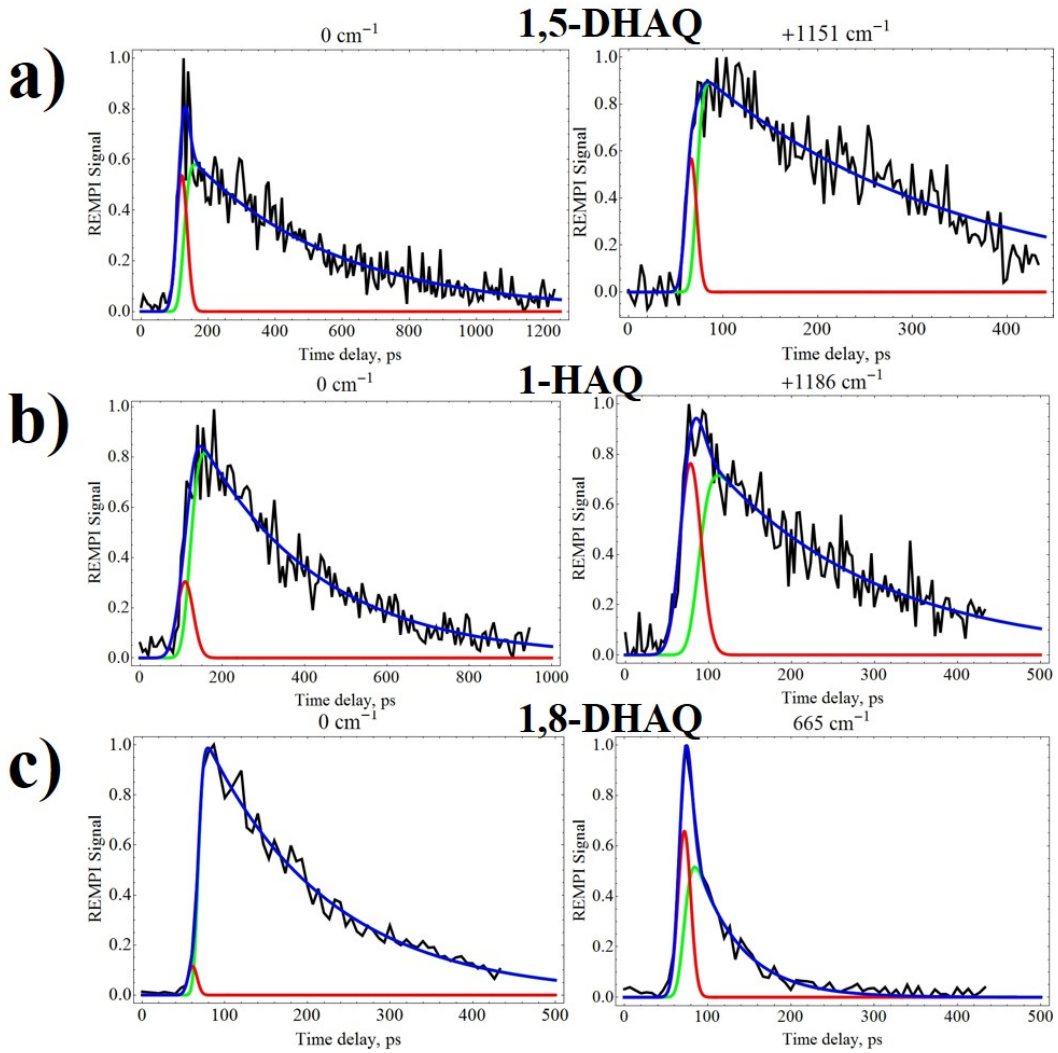

Figure S.2 ps pump-probe spectra for a) 1,5-DHAQ at vibrationless and excess probe lengths, b) 1-HAQ at vibrationless and excess probe lengths, and c) 1,8-DHAQ at vibrationless and excess probe lengths. All lifetime values are listed in Table 1. The pump-probe data are fit to a curve (blue) which is the sum of a single exponential decay convolved with a Gaussian component (red) representative of our instrument response function (IRF) the IRF itself (green).

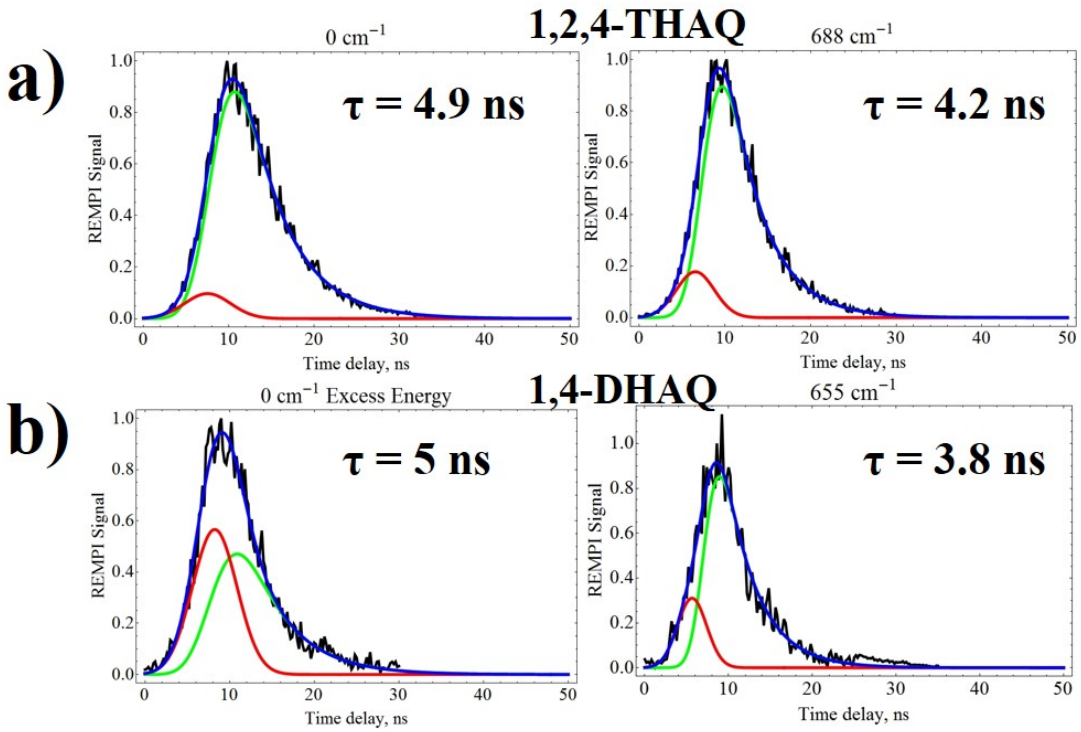

Figure S.3 ns pump-probe spectra for a) 1,2,4-THAQ at vibrationless and excess probe lengths and for c) 1,4-DHAQ at vibrationless and excess probe lengths. The lifetime values here agree with those presented in Table 1 for ps pump-probe measurement within the time jitter (± 3 ns) of the 193 nm ns ionization source. The pump-probe data are fit to a curve (blue) which is the sum of a single exponential decay convolved with a Gaussian component (red) representative of our instrument response function (IRF) the IRF itself (green).

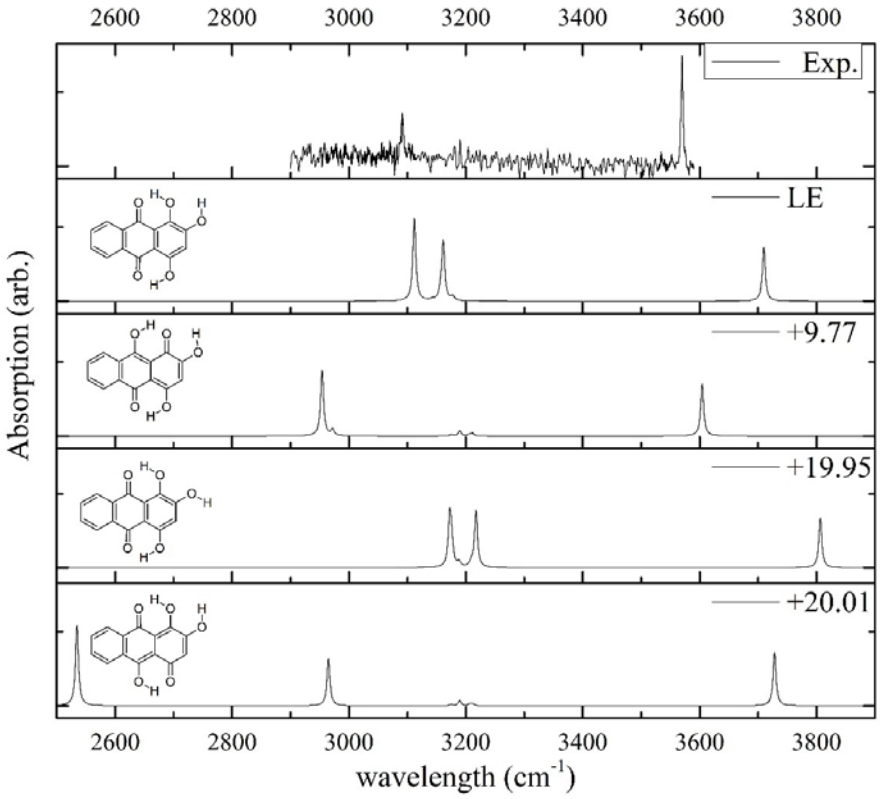

Figure S.4 IR hole burning spectra of 1,2,4-THAQ in mode I with the ps 2C R2PI probe laser set to 19,845 cm^{-1}. Harmonic analysis for each given tautomer (with relative energy in kcal/mol to LE structure) is shown unshifted.

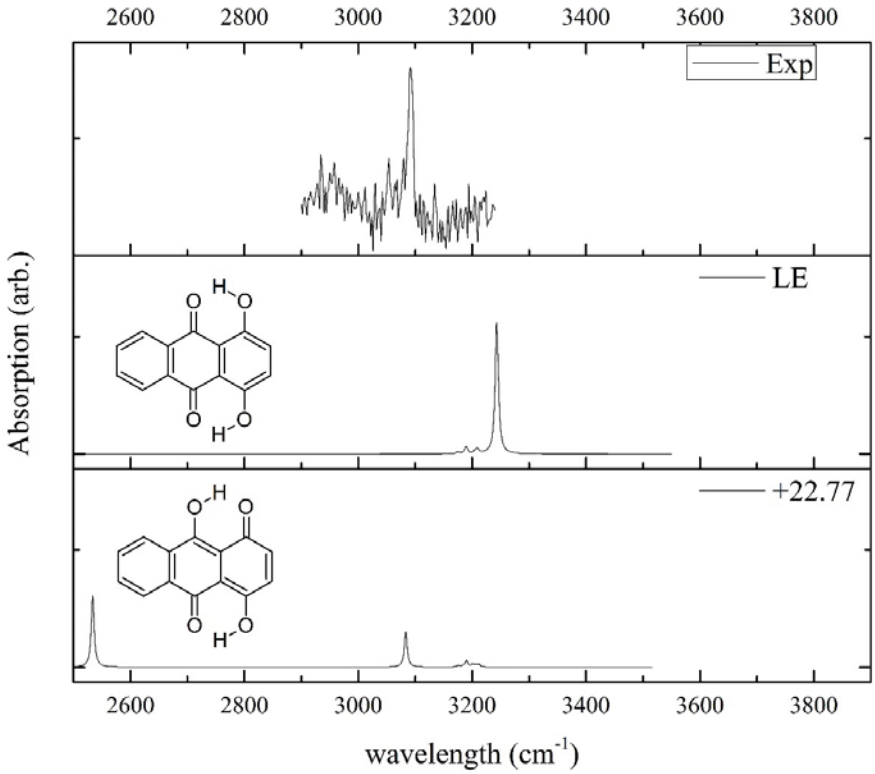

Figure S.5 IR hole burning spectra of 1,4-DHAQ in mode I with the ps 2C R2PI probe laser set to 19,920 cm^{-1}. Harmonic analysis for each given tautomer (with relative energy in kcal/mol to LE structure) is shown unshifted.

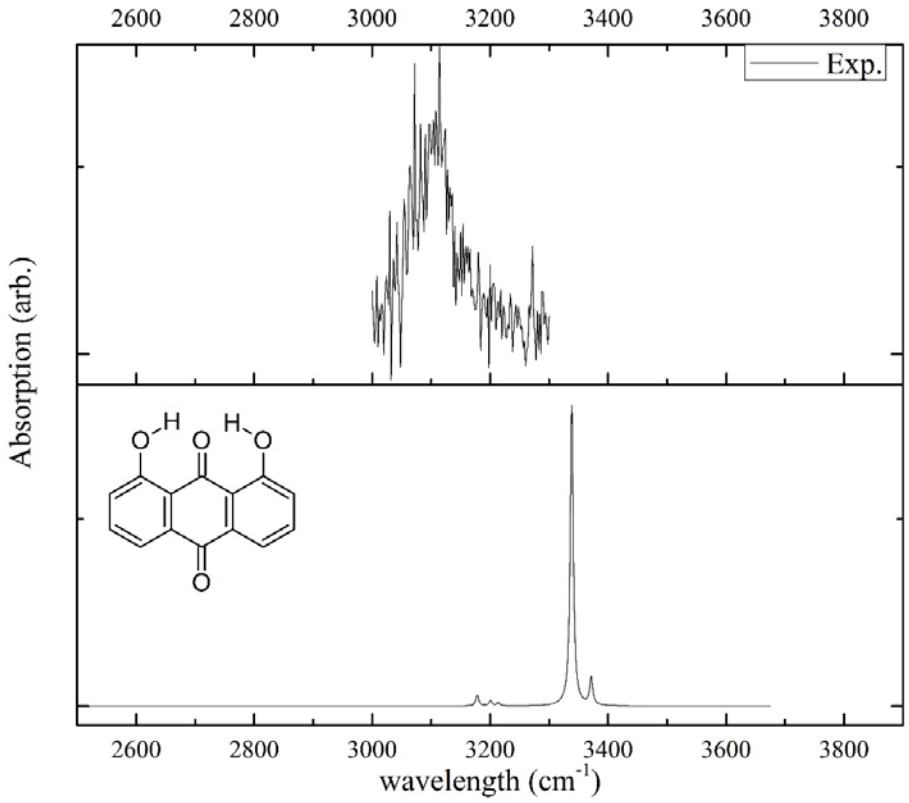

Figure S.6 IR hole burning spectra of 1,8-DHAQ in mode I with the ps 2C R2PI probe laser set to 22,031 cm^{-1}. Harmonic analysis is shown unshifted.

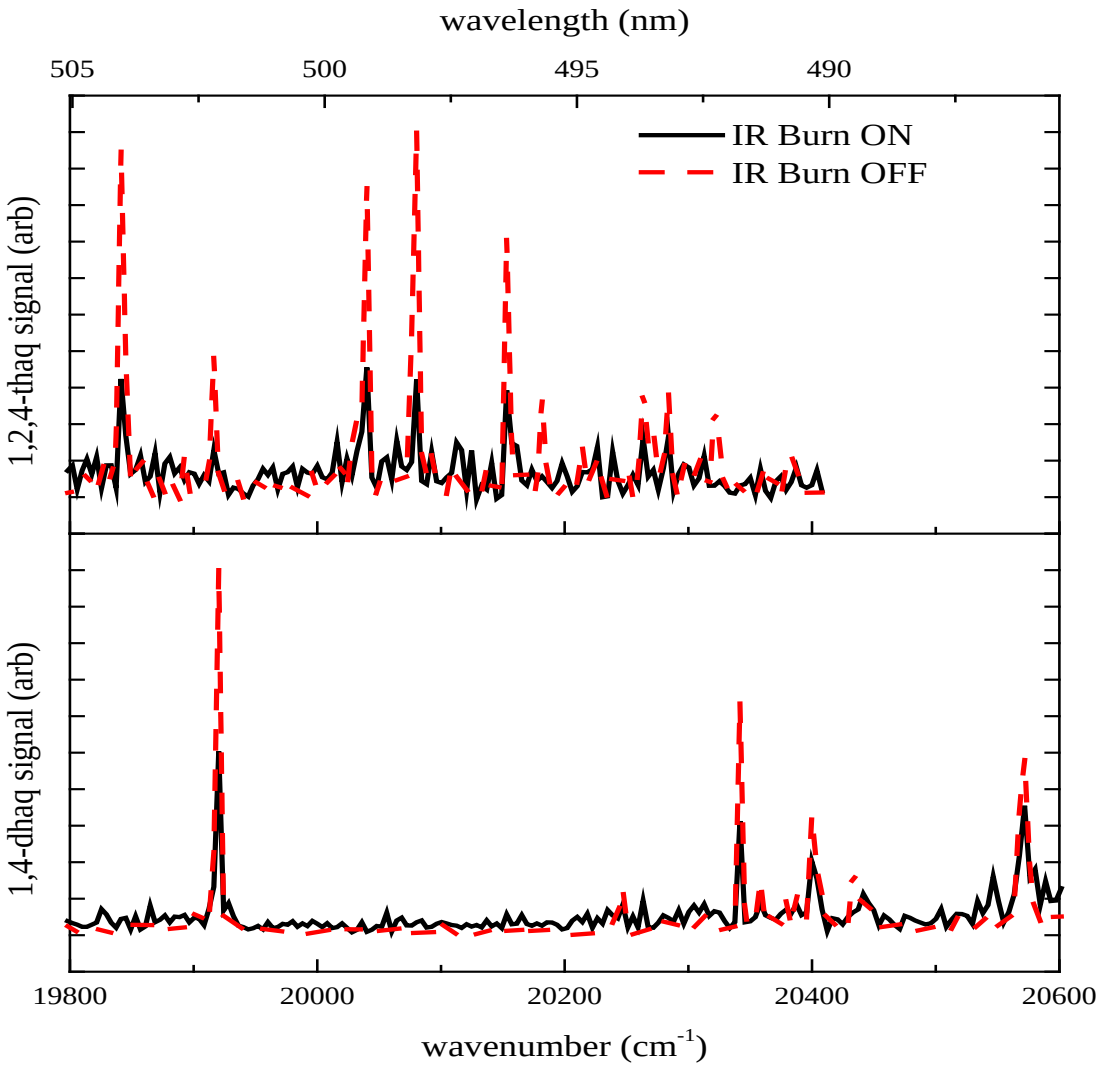

Figure S.7 IR hole burning spectra in mode II with the burn laser set to 3090 cm^{-1}. (Top) All 1,2,4-thaq vibrionic transitions share resonance at IR burn wavelength, as do all (bottom) 1,4-dhaq vibrionic transition suggesting single tautomer.

Table S.2 Review of spectral origins and electronic transition strengths towards excited state lifetimes interpretation. Electronic transition state strengths for S1-4 determined by way of TD-DFT with the B3LYP hybrid functional with CC-pVTZ basis set.

Absorption (cm^{-1})	Oscillator Strength (*f*)	Excited State

			from S0 Optimization				Lifetime (ps)	
Sample	Origin	Δv	S 1	S 2	S 3	S 4	Origin	Δ v
1,2,4-thaq	19,845	+6 88	. 139	0	.0 178	0	5,376	2, 017
1,4-dhaq	19,920	+6 55	. 161	0	0	. 001	1,766	1, 958
1,2,5,8-qhaq	19,661	+4 79	. 233	. 014	0	. 019	1,106	5 37
1,5-dhaq	21,321	+1 151	. 211	0	0	0	431	2 62
1-haq	21,645	+1 186	0	. 114	0	0	290	1 87
1,8-dhaq	22,031	+6 55	0	. 211	.0 05	0	149	5 4
1,2-dhaq	21,748	+1 154	. 089	0	.0 27	0	120	7 3

References

1. Douhal, A.; Lahmani, F.; Zewail, A. H., Proton-transfer reaction dynamics. *Chem. Phys.* **1996,** *207* (2), 477-498.
2. Formosinho, S. J.; Arnaut, L. G., Excited-state proton transfer reactions II. Intramolecular reactions. *Journal of Photochemistry and Photobiology A: Chemistry* **1993,** *75* (1), 21-48.
3. Flom, S. R.; Barbara, P. F., Proton transfer and hydrogen bonding in the internal conversion of S1 anthraquinones. *The Journal of Physical Chemistry* **1985,** *89* (21), 4489-4494.
4. Zhao, J.; Ji, S.; Chen, Y.; Guo, H.; Yang, P., Excited state intramolecular proton transfer (ESIPT): from principal photophysics to the development of new chromophores and applications in fluorescent molecular probes and luminescent materials. *Phys. Chem. Chem. Phys.* **2012,** *14* (25), 8803-17.
5. Bahrenburg, J.; Rode, M. F.; Sobolewski, A. L.; Temps, F., Ultrafast Dynamics of a Bistable Intramolecular Proton Transfer Switch. In *Ultrafast Phenomena XIX: Proceedings of the 19th International Conference, Okinawa Convention Center, Okinawa, Japan, July 7-11, 2014*, Yamanouchi, K.; Cundiff, S.; de Vivie-Riedle, R.; Kuwata-Gonokami, M.; DiMauro, L., Eds. Springer International Publishing: Cham, 2015; pp 399-402.

6. Lapinski, L.; Nowak, M. J.; Nowacki, J.; Rode, M. F.; Sobolewski, A. L., A Bistable Molecular Switch Driven by Photoinduced Hydrogen-Atom Transfer. *ChemPhysChem* **2009,** *10* (13), 2290-2295.
7. Padalkar, V. S.; Seki, S., Excited-state intramolecular proton-transfer (ESIPT)-inspired solid state emitters. *Chem. Soc. Rev.* **2016,** *45* (1), 169-202.
8. Christie, R., Carbonyl dyes and pigments. In *Colour Chemistry*, Christie, R. M., Ed. The Royal Society of Chemistry: 2001; pp 69-91.
9. Dave, H.; Ledwani, L., *A review on anthaquinones isolated from Cassia species and their applications*. 2012; Vol. 3, p 291-319.
10. Wijnsma, R.; Verpoorte, R., Anthraquinones in the Rubiaceae. In *Fortschritte der Chemie organischer Naturstoffe / Progress in the Chemistry of Organic Natural Products*, Herz, W.; Grisebach, H.; Kirby, G. W.; Tamm, C., Eds. Springer Vienna: Vienna, 1986; pp 79-149.
11. Willy Herbst, K. H., *Industrical Organic Pigments: Production, Properties, Applications*. Third ed.; WILEY-VCH Verlag GmbH & Co. KGaA: Weinheim, Germany, 2004.
12. Brown, J. P., A review of the genetic effects of naturally occurring flavonoids, anthraquinones and related compounds. *Mutation Research/Reviews in Genetic Toxicology* **1980,** *75* (3), 243-277.
13. Malik, E. M.; Müller, C. E., Anthraquinones As Pharmacological Tools and Drugs. *Medicinal Research Reviews* **2016,** *36* (4), 705-748.
14. El-Najjar, N.; Gali-Muhtasib, H.; Vuorela, P.; Urtti, A.; Vuorela, H., Naphthoquinones and Anthraquinones: Chemical, Analytical, and Biological Overview. In *Encyclopedia of Analytical Chemistry*, John Wiley & Sons, Ltd: 2006.
15. Finlay, V., Color: A Natural History of the Palette. Random House, Inc.: New York, 2004; pp 134-68.
16. Grazia, C.; Clementi, C.; Miliani, C.; Romani, A., Photophysical properties of alizarin and purpurin Al(III) complexes in solution and in solid state. *Photochem Photobiol Sci* **2011,** *10* (7), 1249-54.
17. Ahn, C.; Zeng, X.; Obendorf, S. K., High-performance liquid chromatography-diode array detector-mass selective detector analysis of major natural dyes with the application of H2O2/ultraviolet treatment as a way to simulate burial degradation of textiles. *Textile Research Journal* **2014**.
18. Saunders, D.; Kirby, J., Light-induced Colour Changes in Red and Yellow Lake Pigments. *National Gallery Technical Bulletin* **1994,** *15*, 77-79.
19. Padfield, T.; Landi, S., The Light-Fastness of the Natural Dyes. *Studies in Conservation* **1966,** *11* (4), 181-196.
20. Clementi, C.; Nowik, W.; Romani, A.; Cibin, F.; Favaro, G., A spectrometric and chromatographic approach to the study of ageing of madder (Rubia tinctorum L.) dyestuff on wool. *Anal. Chim. Acta* **2007,** *596* (1), 46-54.
21. Tan, J. A.; Garakyaraghi, S.; Tagami, K. A.; Frano, K. A.; Crockett, H. M.; Ogata, A. F.; Patterson, J. D.; Wustholz, K. L., Contributions from Excited-State Proton and Electron Transfer to the Blinking and Photobleaching Dynamics of Alizarin and Purpurin. *J Phys Chem C* **2017,** *121* (1), 97-106.
22. Navas Diaz, A., Absorption and emission spectroscopy and photochemistry of 1,10-anthraquinone derivatives: a review. *Journal of Photochemistry and Photobiology A: Chemistry* **1990,** *53* (2), 141-167.

23. T. P. Carter, D. G., 't and M. A. Connolly, Intramolecular Hydrogen Bonding Probed by Laser- Induced Fluorescence. 1. 1,4-Dihydroxyanthraquinone (Quinizarin). *J. Phys. Chem.* **1982,** *86*, 192-196.
24. T. P. Carter, M. H. V. B., and G. D. Glllsple, Fluorescence and Fluorescence Excitation Spectra of I-Aminoanthraquinone in an +Heptane Shpol'skii Matrix. *J. Phys. Chem.* **1983,** *87* (1891-1898).
25. Gillispie, M. H. V. B. a. G. D., Intramolecular Hydrogen Bonding. 4. Dual Fluorescence and Excited-State Proton Transfer in 1,5-Dlhydroxyanthraqulnone. *J. Phys. Chem.* **1984,** *88*, 2954-2960.
26. Nagaoka, S.-i.; Nagashima, U., Effects of node of wave function upon excited-state intramolecular proton transfer of hydroxyanthraquinones and aminoanthraquinones. *Chem. Phys.* **1996,** *206* (3), 353-362.
27. Lee, S.; Lee, J.; Pang, Y., Excited state intramolecular proton transfer of 1,2-dihydroxyanthraquinone by femtosecond transient absorption spectroscopy. *Current Applied Physics* **2015,** *15* (11), 1492-1499.
28. Ryu, J.; Kim, H. W.; Kim, M. S.; Joo, T., Ultrafast Excited State Intramolecular Proton Transfer Dynamics of 1-Hydroxyanthraquinone in Solution. *Bull. Korean Chem. Soc.* **2013,** *34* (2), 465-469.
29. Sun, S.-m.; Zhang, S.; Liu, K.; Wang, Y.-p.; Zhou, M.-m.; Zhang, B., Excited State Intramolecular Proton Transfer of 1-Hydroxyanthraquinone. *Chinese Journal of Chemical Physics* **2015,** *28* (5), 545-551.
30. Mohammed, O. F.; Xiao, D.; Batista, V. S.; Nibbering, E. T., Excited-state intramolecular hydrogen transfer (ESIHT) of 1,8-dihydroxy-9,10-anthraquinone (DHAQ) characterized by ultrafast electronic and vibrational spectroscopy and computational modeling. *J. Phys. Chem. A* **2014,** *118* (17), 3090-9.
31. Jen, M.; Lee, S.; Jeon, K.; Hussain, S.; Pang, Y., Ultrafast Intramolecular Proton Transfer of Alizarin Investigated by Femtosecond Stimulated Raman Spectroscopy. *J. Phys. Chem. B* **2017,** *121* (16), 4129-4136.
32. Smoluch, M.; Joshi, H.; Gerssen, A.; Gooijer, C.; van der Zwan, G., Fast excited-state intramolecular proton transfer and subnanosecond dynamic stokes shift of time-resolved fluorescence spectra of the 5-methoxysalicylic acid/diethyl ether complex. *J. Phys. Chem. A* **2005,** *109* (4), 535-41.
33. Simpson, M. C.; Thompson, S. J.; Ashforth, S.; Bodley, O.; Oosterbeek, R.; Ware, H.; Hosking, P., From Art Fading to Sperm Sorting. *2014 Optoelectronics and Communications Conference and Australian Conference on Optical Fibre Technology (Oecc/Acoft 2014)* **2014**, 319-321.
34. Peng, Y.; Ye, Y.; Xiu, X.; Sun, S., Mechanism of Excited-State Intramolecular Proton Transfer for 1,2-Dihydroxyanthraquinone: Effect of Water on the ESIPT. *J. Phys. Chem. A* **2017,** *121* (30), 5625-5634.
35. Meijer, G.; Devries, M. S.; Hunziker, H. E.; Wendt, H. R., Laser Desorption Jet-Cooling of Organic-Molecules - Cooling Characteristics and Detection Sensitivity. *Appl Phys B-Photo* **1990,** *51* (6), 395-403.
36. Siouri, F. M.; Boldissar, S.; Berenbeim, J. A.; de Vries, M. S., Excited State Dynamics of 6-Thioguanine. *J. Phys. Chem. A* **2017,** *121* (28), 5257-5266.
37. Irimia, D.; Dobrikov, D.; Kortekaas, R.; Voet, H.; van den Ende, D. A.; Groen, W. A.; Janssen, M. H., A short pulse (7 micros FWHM) and high repetition rate (dc-5 kHz)

cantilever piezovalve for pulsed atomic and molecular beams. *Rev. Sci. Instrum.* **2009,** *80* (11), 113303.
38. Frisch, M. J.; Trucks, G. W.; Schlegel, H. B.; Scuseria, G. E.; Robb, M. A.; Cheeseman, J. R.; Scalmani, G.; Barone, V.; Mennucci, B.; Petersson, G. A.; Nakatsuji, H.; Caricato, M.; Li, X.; Hratchian, H. P.; Izmaylov, A. F.; Bloino, J.; Zheng, G.; Sonnenberg, J. L.; Hada, M.; Ehara, M.; Toyota, K.; Fukuda, R.; Hasegawa, J.; Ishida, M.; Nakajima, T.; Honda, Y.; Kitao, O.; Nakai, H.; Vreven, T.; Montgomery, J. A.; Peralta, J. E.; Ogliaro, F.; Bearpark, M.; Heyd, J. J.; Brothers, E.; Kudin, K. N.; Staroverov, V. N.; Kobayashi, R.; Normand, J.; Raghavachari, K.; Rendell, A.; Burant, J. C.; Iyengar, S. S.; Tomasi, J.; Cossi, M.; Rega, N.; Millam, J. M.; Klene, M.; Knox, J. E.; Cross, J. B.; Bakken, V.; Adamo, C.; Jaramillo, J.; Gomperts, R.; Stratmann, R. E.; Yazyev, O.; Austin, A. J.; Cammi, R.; Pomelli, C.; Ochterski, J. W.; Martin, R. L.; Morokuma, K.; Zakrzewski, V. G.; Voth, G. A.; Salvador, P.; Dannenberg, J. J.; Dapprich, S.; Daniels, A. D.; Farkas; Foresman, J. B.; Ortiz, J. V.; Cioslowski, J.; Fox, D. J., Gaussian 09, Revision B.01. Wallingford CT, 2009.
39. Plutzer, C.; Nir, E.; de Vries, M. S.; Kleinermanns, K., IR-UV double-resonance spectroscopy of the nucleobase adenine. *Phys. Chem. Chem. Phys.* **2001,** *3* (24), 5466-5469.
40. Felker, P. M.; Lambert, W. R.; Zewail, A. H., Dynamics of intramolecular vibrational-energy redistribution (IVR). IV. Excess energy dependence, t-stilbene. *The Journal of Chemical Physics* **1985,** *82* (7), 3003-3010.
41. Felker, P. M.; Zewail, A. H., Observation of Restricted Ivr in Large Molecules - Quasi-Periodic Behavior, Phase-Shifted and Non-Phase-Shifted Quantum Beats. *Chem. Phys. Lett.* **1983,** *102* (2-3), 113-119.
42. Morimoito, A.; Yatsuhashi, T.; Shimada, T.; Biczók, L.; Tryk, D. A.; Inoue, H., Radiationless Deactivation of an Intramolecular Charge Transfer Excited State through Hydrogen Bonding: Effect of Molecular Structure and Hard−Soft Anionic Character in the Excited State. *The Journal of Physical Chemistry A* **2001,** *105* (45), 10488-10496.
43. Giacco, T. D.; Latterini, L.; Elisei, F., Photophysical and photochemical properties of 1,2,4-trihydroxy-9,10-anthraquinone adsorbed on inorganic oxides. *Photochemical & Photobiological Sciences* **2003,** *2* (6), 681-687.
44. Mallakin, A.; George Dixon, D.; Greenberg, B. M., Pathway of anthracene modification under simulated solar radiation. *Chemosphere* **2000,** *40* (12), 1435-1441.
45. Mallakin, A.; McConkey, B. J.; Miao, G.; McKibben, B.; Snieckus, V.; Dixon, D. G.; Greenberg, B. M., Impacts of Structural Photomodification on the Toxicity of Environmental Contaminants: Anthracene Photooxidation Products. *Ecotoxicology and Environmental Safety* **1999,** *43* (2), 204-212.

III. Applied REMPI Analysis

Lastly, is a two-part chapter on the application of REMPI to study *meso-american pottery* (Chapter 3.1) and *painting cross sections* (Chapter 3.2). These chapters emphasize the ability to go beyond fundamental research and apply these laser spectroscopic methods to more tangible scientific projects.

I. Direct Analysis of Xanthine Stimulants in Archaeological Vessels by Laser Desorption Resonance Enhanced Multiphoton Ionization

Shawn C. Owens[†], Jacob A. Berenbeim[†], Marshall R. Ligare[†], Lisa E. Gulian[†], Faady M. Siouri[†], Samuel Boldissar[†], Stuart Tyson-Smith[‡], Gregory Wilson[‡], Anabel Ford[§], and Mattanjah S. de Vries[*†]

[†] Department of Chemistry and Biochemistry, University of California Santa Barbara, Santa Barbara, California 93106, United States

[‡] Department of Anthropology, University of California Santa Barbara, Santa Barbara, California 93106, United States

[§] MesoAmerican Research Center, University of California Santa Barbara, Santa Barbara, California 93106, United States

Reprinted with permission from *Anal. Chem.*, 2017, 89 (5), pp 2838–2843 **DOI:** 10.1021/acs.analchem.6b03932

*E-mail: devries@chem.ucsb.edu.

Abstract

Resonance enhanced multiphoton ionization spectroscopy (REMPI) generates simultaneous vibronic spectroscopy and fragment free mass spectrometry to identify molecules within a complex matrix. We combined laser desorption with REMPI spectroscopy to study organic residues within pottery sherds from Maya vessels (600–900 CE) and Mississippian vessels (1100–1200 CE), successfully detecting three molecular markers, caffeine, theobromine, and theophylline, associated with the use of cacao. This analytical approach provides a high molecular specificity, based on both wavelength and mass identification. At the same time, the high detection limit allows for direct laser desorption from sherd scrapings, avoiding the need for extracting organic constituents from the sherd matrix.

Introduction

Analysis of organic compounds in pottery sherds traditionally relies on the use of infrared spectroscopy,[1] separation techniques such as gas chromatography–mass spectrometry (GC–MS),[2,3] high-performance liquid chromatography (HPLC),(4) and liquid chromatography–mass spectrometry (LC–MS).[2,5-7] Chromatographic techniques, while providing a wealth of information, often cannot be routinely applied to cultural heritage artifacts, e.g., pottery sherds, due to the relatively large sample-size and sample consumption required by most GC and LC techniques.[7] Typically, pieces of several cm^3 in size may be needed to yield 500 mg of material for extraction. Fourier transform-infrared (FT-IR) spectroscopy of pottery samples can provide functional group identification of organic, as well as some inorganic, compounds but can be challenging since the organic materials often are present as part of an extremely complex mixture.[1] While these techniques provide important information, they often lack the capability to identify unique compounds or require hundreds of milligrams of sample to do so. Therefore, there remains a need for

techniques that require less sample, thus causing less physical damage to the object, while maintaining high molecular selectivity. Here we describe a technique for organic tracer molecule analysis for archaeometry, in a specialized form of laser mass spectrometry. A laser-desorption jet-cooling source is followed by resonance enhanced multiphoton ionization (REMPI) and time-of-flight (TOF) mass spectrometry. This approach combines the *selectivity* of resonant laser spectroscopy with the *sensitivity* of mass spectrometry and is therefore simultaneously highly specific and sensitive.[8-16]

As a member of the theobroma genus, the cacao bean (*Theobroma cacao*) originates from a tree confined to within the tropical regions of South America and Mesoamerica.[17] The seeds, or pods, produced by the tree were ground up and mixed with other ingredients (water, maize, honey) to make a drink that had a mild stimulating effect.[18] It was a particularly important cultural icon in Mesoamerican society and has been consumed by the Maya as early as 600 BCE[18] in addition to being the precursor to modern day chocolate.

Three molecules associated with the cacao bean are caffeine (1,3,7-trimethylxanthine), theobromine (3,7-dimethylxanthine), and theophylline (1,3-dimethylxanthine) and these have been found in pottery sherds found in the Mesoamerican region.[2,18-22] These compounds are still very common today in stimulant drinks such as coffee, tea, and yerba mate. Serving as natural pest deterrents, these three methylxanthines are found in over 13 orders of plants, comprising well over 100 different plant species and are often used as molecular markers to identify geo-cultural origins of pottery sherds, particularly cacao.[3,23]

Similar to cacao in MesoAmerican culture, people from regions around the American gulf coast prepared a black tea made from the yaupon holly (*I. vomitoria*) as well as the dahoon holly (*I. cassine*). These species contain caffeine and theobromine but are not believed to contain theophylline.[3,7,24] Further, yerba mate (*I. paraguariensis*), guarana fruit

(*P. cupana*), and the yoco vine (*P. yoco*) is widespread in South America and contains caffeine, theobromine, and/or theophylline.[23,25-27] Because of the shared occurrence of caffeine, theobromine, and/or theophylline it is clear that analytical tools need to go beyond positive identification of these molecules within complex matrixes and need to consider the relative occurrence to identify the organic origin of the residue in question.

Each plant species has a characteristic concentration of each methylxanthine, which is commonly used to narrow down the species of plant serving as the source of the organic residues in question. The method presented here can positively confirm the presence of methylxanthines with a reasonably high analytical detection limit and may pragmatically identify cacoa residue from pottery samples excavated where cacao and holly species are geolocated. The complete attribution of concentration ratios of the different marker molecules to specific plants is complicated because the distribution and concentration of these molecules in different plants is somewhat contentious given all the variable conditions. Moreover, the extraction dynamics can affect the ratios observed.[25] Previous analysis of pottery from Central America has identified theobromine in residue from the inside of ceramic vessels from Honduras, Guatemala, and Belize dating from 1500 BCE to 480 CE.[18,21,2] The identifications were made by GC–MS and HPLC–MS. Recent research has also suggested the presence of all three molecular markers in sherds found in Northwestern New Mexico and the Central Illinois River Valley, with the authors suggesting a previously unknown trade network with MesoAmerican cultures.[7,28,29]

In the following sections we will detail the technique by which we identify these molecular markers in pottery sherds, followed by a first example of the identification of methylxanthine markers in organic residues in Maya and Mississippian pottery sherds.

Experimental Section

Two-Step Laser Mass Spectrometry

Figure 1 schematically shows the experimental setup which has been reported in more detail elsewhere.[30] The sample obtained from the pottery sherd can be either an extract deposited onto a sample bar or sherd scrapings placed on a sample bar from which we laser desorb directly. The sample bar is mounted in a vacuum chamber, directly in front of a pulsed molecular beam controlled by a piezo cantilever valve[31,32] (4×10^{-6} Torr source chamber pressure). Laser desorption provides intact vaporization of large, complex, and/or thermally labile molecules. The desorbed molecules are entrained in a pulsed supersonic jet expansion of argon, which provides very efficient cooling of the internal degrees of freedom of the molecules to the order of 10–20 K.[33,34] At this point, the cold molecules are gaseous and free of any intermolecular, i.e. matrix, interactions. The cooling makes it possible to perform high-resolution unimolecular spectroscopy while at the same time stabilizing the molecule, permitting its detection at the parent molecular mass. Typical desorption laser fluence is on the order of 10 $\mu J/cm^2$ in 10 ns laser pulses.[35-40] The desorption laser is focused using either a cylindrical lens or a spherical lens, generating desorption spot sizes of 0.50 mm × 3.0 mm or 0.75 mm diameter, respectively. Following jet-cooling, the molecular beam is skimmed before being intersected by laser beam(s) and photoionized. We implement resonance enhanced multiphoton ionization (REMPI) in two modes, using either one or two colors.[41] The subsequent ions are detected by a reflectron time-of-flight mass spectrometer (2×10^{-6} Torr analyzer pressure, mass resolution $m/\Delta m = 500$).

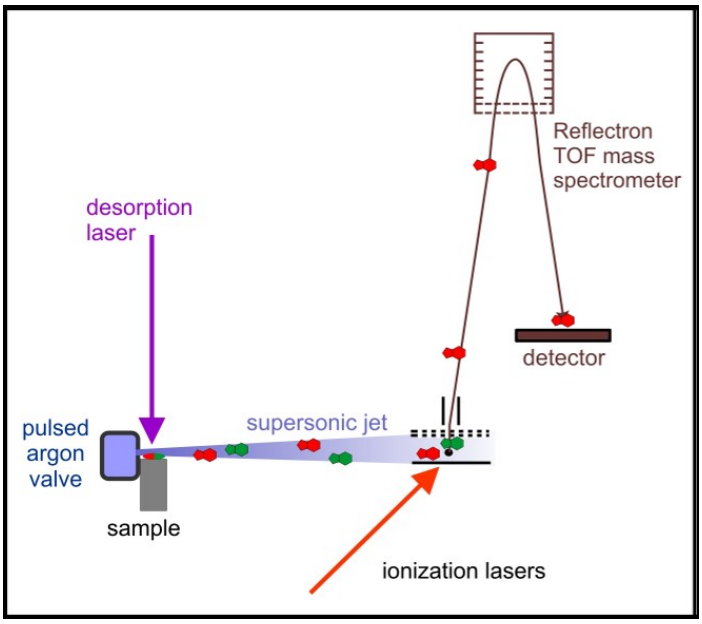

Figure 1. Depiction of the laser desorption jet cooling mass spectrometer where a mixture of isomers (represented by red and green symbols) is laser desorbed in vacuo and entrained in a pulsed Ar molecular beam. Upon entering the ion source, tunable REMPI lasers offer spectroscopic selectivity (in this example, exciting the "red" isomers) and soft ionization, followed by TOF mass detection.

REMPI

Resonance enhanced two-photon ionization combines optical spectroscopy with mass spectrometry. This dramatically enhances the specificity for selected compounds and allows for distinction of structural isomers, tautomers, and enantiomers.[42] A tunable laser provides resonant vibronic excitation of the jet-cooled molecules to a low level intermediate electronic state. Subsequently, another photon ionizes the excited molecule either from the same laser pulse (1-color REMPI) or from an overlapped second laser if additional energy is needed (2-color REMPI). In the case of methylxanthine, both photons originate from the doubled output of a Lumonics HD-300 tunable dye laser (spectral line width ≈ 0.04 cm^{-1}, pulse energy ≈ 0.3–0.7 mJ in 8 ns pulses).

Scanning the wavelength of the first photon while monitoring a specific ion mass generates a mass selected excitation spectrum or REMPI spectrum. When the REMPI

spectrum of a given compound is known, the excitation laser can be tuned to a specific resonance in order to selectively ionize it. Since the sample has been decoupled from matrix interactions in the laser desorption process, REMPI is matrix and concentration independent. This single molecule resonant absorption is a “soft” ionization method with molecular identification based on the wavelength specific signal of the parent ion and no fragmentation pattern disambiguation is necessary. Resonant ionization not only selects for a specific compound; it can also select for specific isomers. We have demonstrated that with this technique we can detect compounds at the femtomole level and in favorable cases down to the 100 attomole level.[9] We can further improve REMPI sensitivity by two color ionization in which the excitation and ionization steps are performed at different wavelengths. Typically, the absorption cross sections for the first and second step are of the order of 10^{-17} cm^2 and 10^{-19} cm^2, respectively. To maintain optimum selectivity, it is undesirable to significantly saturate the first step, forcing us to use a laser fluence that is low by 2 orders of magnitude from what would maximize the second (ionization) step. Therefore, we can improve overall detection limits without sacrificing selectivity if we employ a different wavelength for the second step at higher laser fluence. We have demonstrated this principle for perylene, obtaining an overall 0.25 photoionization efficiency resulting in a 30 femtogram detection limit.[9]

The combination of laser spectroscopy and mass spectrometry provides analytical information in two dimensions: wavelength and mass. Generally spectroscopic resolution, which is typically fractions of wave numbers is several orders of magnitude higher than the mass resolution that can be obtained in conventional mass spectrometry.[42] To fully capitalize on these advantages it is necessary that the spectroscopy of the analyte molecule

is known in a predetermined spectral library. We can find a needle in a haystack, provided we know what the needle looks like.

Detection Limit

We previously reported data for a series of test samples with different concentrations of vanillic acid, a marker for peonidin in grape wine.[43] There the ion signal was linear with concentration (r = 0.9994), allowing (a) quantitative measurements when using internal standards and (b) establishment of a lower limit of detection. The latter will differ from compound to compound because it depends on the ionization efficiency. In the case of vanillic acid with one color ionization at 289.192 nm, we obtained a detection limit at S/N = 3 of 60 picograms per laser shot. To put this limit in perspective, 250 pg of vanillic acid corresponds to a few microliters of modern wine and indeed we have detected vanillic acid in a 5 μL droplet of wine. Even if only 0.1% of the original peonidin content of the wine can be recovered and converted to vanillic acid, we would still only need a milliliter of residue, from for example an amphora, to be able to detect it. For the current study of methylated xanthines, a detection limit of 4 picograms per 10 laser shot average was determined. Theophylline ion signal desorbed from graphite substrate at quantities of 0.05, 0.5, 5, and 50 ng detected by 1C REMPI at 280.71 nm fit a linear regression of the form $\log y = m \log x + b$, where m is slope, x is concentration, b a fitting constant, and y is signal. Extrapolating this fit down to the signal limit, corresponding to the background signal of desorbed blank graphite sample, provided the limit of detection with a S/N of 3. This fit is shown in Figure S.1. If additional detection sensitivity is required, 2C REMPI is used. The ionization wavelength of 308 nm was found to maximize ionization efficiency and minimize fragmentation of the analytes, increasing signal by at least a factor of 2 (shown in Figure S.2). Substrate does have an effect on detection efficiency, and we have tested graphite bars,

gold plated bars, stainless steel pegs, and double sided tape. Of these, graphite bars provide the greatest detection sensitivity but they suffer from sample carryover due to graphite's ability to readily absorb either organic sample or organic solvated sample. We used new graphite bars to negate the possibility of sample contamination between runs, which we also controlled for by analysis of blanks.

Sample Preparation

We purchased standards of theobromine, theophylline, and caffeine from Sigma-Aldrich and used them without further purification. Standards are directly applied to graphite sample bars as a thin solid layer. The spectra for standards were collected using separate graphite bars to ensure each spectrum is free of any other standards.

We analyzed pottery samples directly from the pottery material and from extracts when concentration was necessary. The extracts are made by using a 3:1 mixture of acetone and water. Approximately 400 mg of ground pottery is added to 5 mL of solution and allowed to sit at room temperature for 72 h. The supernatant liquid is then filtered by a Whatman 13 mm GD/X disposable filter, polypropylene filter media with polypropylene housing, 0.45 mm pore size. The extract is then concentrated by gentle heating (25–35 °C) under dry nitrogen flow. The extracts are concentrated approximately 5-fold then deposited dropwise on the ends of 0.75 mm diameter disposable stainless steel pegs mounted to the sample bar. Gentle heating (35–45 °C) is used to speed up evaporation of solvent. The dried, concentrated extracts are then immediately inserted into the instrument for analysis. Direct desorption analysis of the samples is done by applying small amounts (0.5–1.0 mg) of either ground or surface pieces of pottery material to double-sided tape mounted on gold sample bars. A new, clean disposable razor blade was used to scrape sherd fragments directly onto the tape for each sherd tested. Direct desorption does not lend itself to samples in need of

concentration; however, it does allow for the most immediate and unaltered analysis of a sample's composition, avoiding possible unintended chemical rearrangements that can occur in an extraction, condensation, or solvated separation step. Direct analysis also makes it possible to separately sample different parts, for example, to compare surface versus inside areas.

Results

We previously reported the detailed REMPI spectra of all three molecular markers,[44] identifying unique resonances for the selective ionization of each of the markers. The left-hand side of Figure 2 shows the REMPI spectra obtained from each standard. The wavelength range marked by a black box indicates the part of the spectra used for subsequent sample analysis. In order to optimize conditions for each target methylxanthine, we chose a wavelength correlating to a strong REMPI transition and unique to each to perform optically selected mass spectrometry. Figure 2 shows mass spectra obtained at the resonant ionization wavelengths indicated in the figure with asterisks, clearly determining the parent mass with virtually no fragmentation. The peak at mass 40 is from the argon carrier gas of the molecular beam. When comparing theobromine and theophylline signal directly from the same sample, we scanned the wavelength range indicated by the black box. This small part of the spectrum contains distinct and spectrally well separated peaks of each of these compounds.

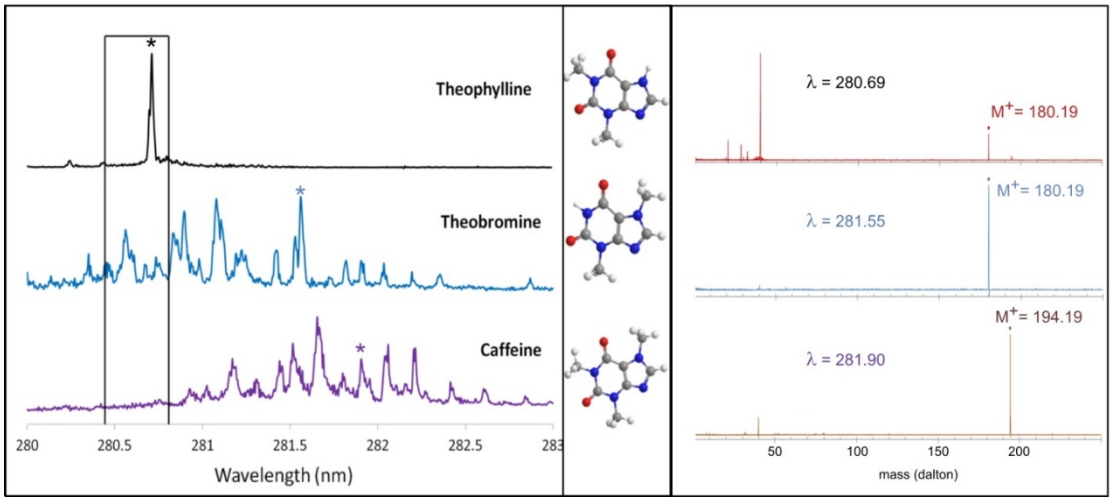

Figure 2. Spectra of methylxanthine standards. Left panel: REMPI spectra recorded on the parent mass, indicated in the right panel. Black box marks the region scanned for the pottery sherds. Right panel: mass spectra recorded at the indicated resonant wavelength, marked for each compound with an asterisk in the left panel. *Y*-axis for both panels in arbitrary units of ion intensity.

We examined samples from three different archeological sites:

(1) A Puerto Escondido vessel extract which has previously tested positive for theobromine by HPLC–MS (Provided by Dr. Patrick McGovern from the Molecular Archaeology lab at the University of Pennsylvania Museum.).

(2) Thirteen base sherds of unique Late Classic period (~600–900 CE) Maya vessels from the El Pilar area, located on the border of Guatemala and Belize.

(3) Seven sherds from the early Mississippian period (~1100–1200 CE) vessels, located from the Central Illinois River Valley in Fulton County, Illinois.

Puerto Escondido Extract

We analyzed extracts provided by Dr. McGovern from theobromine using 2C-REMPI (resonant excitation at 281.55 nm, ionization at 308.00 nm). We detected theobromine in each of these extracts confirming previously published findings.[2]

Maya Sherds

Thirteen samples from different ranked Maya archeological dig sites were analyzed. Rank houses may be associated with different social strata in different areas of the Maya settlement.[45] The data from the analysis of extract revealed some levels of all three methylxanthines in each sherd, excluding sherd one from a small rank house, which tested negative for all three markers. The sherds from the Small Rank and High Rank House show much lower levels of theobromine than theophylline, with caffeine being the most abundant of the three markers. Samples from a median rank house and from a small center exhibit more theobromine relative to the other samples.

In order to investigate the potential of directly desorbing from sherd material, we examined scrapings of the sherds for methylxanthines. The large amount of material required for extraction (≈400 mg) often prevents any analysis of pottery sherds, as many of these items are essentially priceless. In addition, solubility differences can impact the rate at which each respective molecule is extracted from the sherd matrix. Figure 3 shows REMPI spectra, collected at *m*/*z* 180, obtained directly off scrapings from two different sherds, a cylindrical vessel from a minor center and a pedestal base vessel from a median rank house. For comparison, Figure 3 shows pure control samples of theobromine and theophylline which have been scaled in relative intensity to represent equimolar quantities. It is clear that the sherd samples exhibit different theobromine to theophylline residue ratios. This observation suggests a different history for these vessels. The presence of both dimethylxanthine isomers with a relatively high theobromine abundance is a positive indication of cacao present in the cylindrical but not the pedestal base vessel.

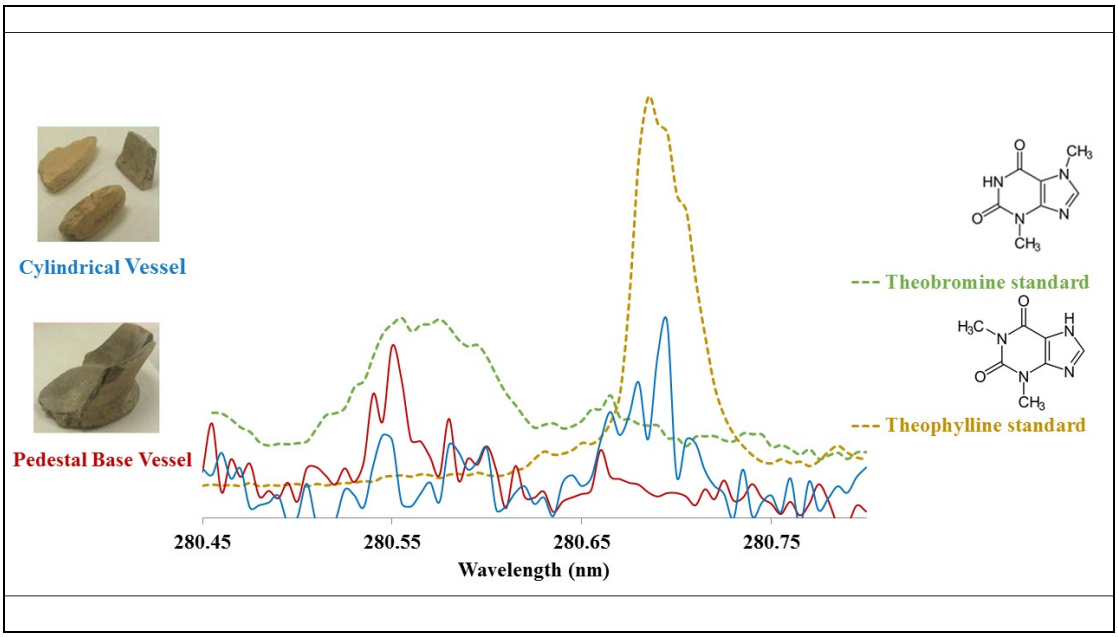

Figure 3. REMPI spectra of two different vessels (cylindrical vessel, blue trace, and pedestal vessel, red trace) performed directly on sherd material. Dotted lines are REMPI spectra of pure standards of theobromine (green trace) and theophylline (yellow trace). Standard spectra have been scaled to represent equimolar intensities (*y*-axis is ion signal in arbitrary units).

Mississippi Sherds

We analyzed seven sherds from what is present day Fulton County, Illinois, collected from bluff tops on the western side of the Central Illinois River Valley flood plain. The sherds originated from a Mississippian culture and date back to between 1100 and 1200 CE. We analyzed these samples using the same procedures established with the Maya sherds but only using direct desorption from sherd material. All seven of these samples showed a strong presence of caffeine and theophylline, while six displayed the presence of some theobromine. The presence of all three methylxanthenes from these Northern American findings suggest the presence of various plant residues. The presence of theophylline could argue against “black” beverage, which would be based on holly native to the area. This conclusion would not be in agreement with past studies except two recent research studies

suggesting the presence of cacao residue in vessels obtained north of Mesoamerica and possibly indicating a previously unknown trade network.[7,29]

Conclusion

The attribution of the geo-cultural origins of pottery sherds is a very complex task, requiring a deep understanding of numerous factors that can affect the presence of certain organic residues. Some of these factors are unavoidable, e.g., physical and biological environmental impacts, solubility differences leading to different leaching rates over time, various clays impacting the affinity for long-term storage of organic molecules, but others are manageable. For example, the initial washing and storage process can be controlled. To preserve water-soluble markers, it can be helpful to avoid the use of water. To minimize the risk of cross contamination sherds can be collected in individual containers. The metabolic n-demethylation of these methylxanthines by soil bacteria can be identified by the products paraxanthine and 7-methylxanthine,[28,46] molecules well suited to REMPI analysis, which we have shown previously in publishing the REMPI spectrum of 7-methylxanthine.[44] The ubiquity of the compounds used as biomarkers in museum, laboratory, and storage spaces can be controlled for by the use of blanks both during analysis and in predictive in situ monitoring of an object's journey from excavation to storage.[28]

We present a new method for analysis of molecular markers of stimulant containing beverages. Pottery sherds from both Central and North America tested positive for all three xanthine alkaloids: caffeine, theobromine, and theophylline. Although the method is not yet quantitative, relative amounts of caffeine to theobromine or caffeine to theophylline are consistent throughout the data set at their respective resonant wavelengths for the direct desorption method. This method is more sensitive than previous methods by identifying all

three xanthine stimulants in multiple samples, requiring much smaller sample sizes. The three major advantages of this technique are reduced sample sizes needed for positive identification, the ability to directly analyze samples in complex matrixes such as clay from pottery without extraction, and simultaneous positive identification both my mass and spectral signature. We are undertaking a systematic study of a larger set of pottery samples to evaluate if it will be possible to derive conclusions about their use from this type of measurement.

Supporting Information

Theophylline ion signals at quantities of 0.05, 0.5, 5.0, and 50.0 ng detected by 1C REMPI at 280.71 nm and desorbed from graphite substrate and example of ionization efficiency at different wavelength combinations for theobromine

Acknowledgment

This material is based upon work supported by the National Science Foundation under Grant CHE-1241779 and Grant CHE-1018804.

References

1. Shillito, L. M.; Almond, M. J.; Wicks, K.; Marshall, L. J. R.; Matthews, W. Spectrochim. Acta, Part A 2009, 72, 120– 125 DOI: 10.1016/j.saa.2008.08.016
2. Henderson, J. S.; Joyce, R. A.; Hall, G. R.; Hurst, W. J.; McGovern, P. E. Proc. Natl. Acad. Sci. U. S. A. 2007, 104, 18937– 18940 DOI: 10.1073/pnas.0708815104
3. Reber, E. A.; Kerr, M. T. J. Archaeol. Sci. 2012, 39, 2312– 2319 DOI: 10.1016/j.jas.2012.02.008
4. Naik, J. P. J. Agric. Food Chem. 2001, 49, 3579– 3583 DOI: 10.1021/jf000728z
5. Guasch-Jane, M. R.; Ibern-Gomez, M.; Andres-Lacueva, C.; Jauregui, O.; Lamuela-Raventos, R. M. Anal. Chem. 2004, 76, 1672– 1677 DOI: 10.1021/ac035082z
6. Mottram, H. R.; Dudd, S. N.; Lawrence, G. J.; Stott, A. W.; Evershed, R. P. J. Chromatogr. A 1999, 833, 209– 221 DOI: 10.1016/S0021-9673(98)01041-3

7. Crown, P. L.; Gu, J.; Hurst, W. J.; Ward, T. J.; Bravenec, A. D.; Ali, S.; Kebert, L.; Berch, M.; Redman, E.; Lyons, P. D.; Merewether, J.; Phillips, D. A.; Reed, L. S.; Woodson, K. Proc. Natl. Acad. Sci. U. S. A. 2015, 112, 11436– 11442 DOI: 10.1073/pnas.1511799112

8. Arrowsmith, P.; de Vries, M. S.; Hunziker, H. E.; Wendt, H. R. Appl. Phys. B: Lasers Opt. 1988, 46, 165– 173 DOI: 10.1007/BF00686471

9. Meijer, G.; de Vries, M. S.; Hunziker, H. E.; Wendt, H. R. Appl. Phys. B: Lasers Opt. 1990, 51, 395– 403 DOI: 10.1007/BF00329101

10. Nir, E.; Hunziker, H. E.; de Vries, M. S. Anal. Chem. 1999, 71, 1674– 1678 DOI: 10.1021/ac981383a

11. de Vries, M. S.; Elloway, D. J.; Wendt, H. R.; Hunziker, H. E. Rev. Sci. Instrum. 1992, 63, 3321– 3325 DOI: 10.1063/1.1142546

12. Mahajan, T. B.; Plows, F. L.; Gillette, J. S.; Zare, R. N.; Logan, G. A. J. Am. Soc. Mass Spectrom. 2001, 12, 989– 1001 DOI: 10.1016/S1044-0305(01)00279-3

13. Gillette, J. S.; Ghosh, U.; Mahajan, T. B.; Zare, R. N.; Luthy, R. G. Isr. J. Chem. 2001, 41, 105– 110 DOI: 10.1560/6APH-95X3-JF61-MKAP

14. Mahajan, T. B.; Ghosh, U.; Zare, R. N.; Luthy, R. G. Int. J. Mass Spectrom. 2001, 212, 41– 48 DOI: 10.1016/S1387-3806(01)00470-5

15. Boesl, U.; Zimmermann, R.; Weickhardt, C.; Lenoir, D.; Schramm, K. W.; Kettrup, A.; Schlag, E. W. Chemosphere 1994, 29, 1429– 1440 DOI: 10.1016/0045-6535(94)90276-3

16. Hafner, K.; Zimmermann, R.; Rohwer, E. R.; Dorfner, R.; Kettrup, A. Anal. Chem. 2001, 73, 4171– 4180 DOI: 10.1021/ac010244h

17. Ogata, N. Lowland Maya Area: Three Millennia at the Human-Wildland Interface; The Haworth Press Inc.: Binghamton, NY, 2003; pp 415– 438.

18. Hurst, W. J.; Tarka, S. M.; Powis, T. G.; Valdez, F.; Hester, T. R. Nature 2002, 418, 289– 290 DOI: 10.1038/418289a

19. Brunetto, M. a. d. R.; Gutiérrez, L.; Delgado, Y.; Gallignani, M.; Zambrano, A.; Gómez, Á.; Ramos, G.; Romero, C. Food Chem. 2007, 100, 459– 467 DOI: 10.1016/j.foodchem.2005.10.007

20. Hall, G. D.; Tarka, S. M.; Hurst, W. J.; Stuart, D.; Adams, R. E. W. Am. Antiq. 1990, 55, 138– 143 DOI: 10.2307/281499

21. Hurst, W. J.; Martin, R. A.; Tarka, S. M.; Hall, G. D. J. Chromatogr. 1989, 466, 279– 289 DOI: 10.1016/S0021-9673(01)84623-9

22. Lo Coco, F.; Lanuzza, F.; Micali, G.; Cappellano, G. J. Chromatogr. Sci. 2007, 45, 273– 275 DOI: 10.1093/chromsci/45.5.273

23. Ashihara, H.; Kato, M.; Crozier, A. In Methylxanthines; Springer: Berlin, Heidelberg, Germany, 2011; pp 11– 31.

24. Edwards, A. L.; Bennett, B. C. Econ. Bot. 2005, 59, 275– 285 DOI: 10.1663/0013-0001(2005)059[0275:DOMCII]2.0.CO;2

25. Saldaña, M. D. A.; Mohamed, R. S.; Baer, M. G.; Mazzafera, P. J. Agric. Food Chem. 1999, 47, 3804– 3808 DOI: 10.1021/jf981369z

26. Meinhart, A. D.; Bizzotto, C. S.; Ballus, C. A.; Rybka, A. C. P.; Sobrinho, M. R.; Cerro-Quintana, R. S.; Teixeira, J.; Godoy, H. T. J. Agric. Food Chem. 2010, 58, 2188– 2193 DOI: 10.1021/jf903781w

27. Schimpl, F. C.; da Silva, J. F.; Gonçalves, J. F. d. C.; Mazzafera, P. J. Ethnopharmacol. 2013, 150, 14– 31 DOI: 10.1016/j.jep.2013.08.023

28. Washburn, D. K.; Washburn, W. N.; Shipkova, P. A.; Pelleymounter, M. A. J. Archaeol. Sci. 2014, 50, 191– 207 DOI: 10.1016/j.jas.2014.07.011

29. Washburn, D. K.; Washburn, W. N.; Shipkova, P. A. J. Archaeol. Sci. 2011, 38, 1634–1640 DOI: 10.1016/j.jas.2011.02.029

30. Meijer, G.; Devries, M. S.; Hunziker, H. E.; Wendt, H. R. Appl. Phys. B: Lasers Opt. 1990, 51, 395– 403 DOI: 10.1007/BF00329101

31. Meng, C. S.; Janssen, M. H. M. Rev. Sci. Instrum. 2015, DOI: 10.1063/1.4913251

32. Irimia, D.; Kortekaas, R.; Janssen, M. H. M. Phys. Chem. Chem. Phys. 2009, 11, 3958–3966 DOI: 10.1039/b822960k

33. Li, L.; Lubman, D. M. Rev. Sci. Instrum. 1988, 59, 557– 561 DOI: 10.1063/1.1139832

34. Weyssenhoff, H. V.; Selzle, H. L.; Schlag, E. W. Z. Naturforsch. 1985, 40a, 674– 676

35. Meijer, G.; de Vries, M. S.; Hunziker, H. E.; Wendt, H. R. J. Phys. Chem. 1990, 94, 4394– 4396 DOI: 10.1021/j100374a006

36. Anex, D. S.; de Vries, M. S.; Knebelkamp, A.; Bargon, J.; Wendt, H. R.; Hunziker, H. E. Int. J. Mass Spectrom. Ion Processes 1994, 131, 319– 334 DOI: 10.1016/0168-1176(93)03874-L

37. Nir, E.; Grace, L. I.; Brauer, B.; de Vries, M. S. J. Am. Chem. Soc. 1999, 121, 4896–4897 DOI: 10.1021/ja984088g

38. Cohen, R.; Nir, E.; Grace, L. I.; Brauer, B.; de Vries, M. S. J. Phys. Chem. A 2000, 104, 6351– 6355 DOI: 10.1021/jp000413m

39. Nir, E.; Imhof, P.; Kleinermanns, K.; de Vries, M. S. J. Am. Chem. Soc. 2000, 122, 8091– 8092 DOI: 10.1021/ja000502c

40. Nir, E.; Muller, M.; Grace, L. I.; de Vries, M. S. Chem. Phys. Lett. 2002, 355, 59– 64 DOI: 10.1016/S0009-2614(02)00180-X

41. Zandee, L.; Bernstein, R. B. J. Chem. Phys. 1979, 70, 2574– 2575 DOI: 10.1063/1.437721

42. Imasaka, T.; Moore, D. S.; Vo-Dinh, T. Pure Appl. Chem. 2003, 75, 975– 998 DOI: 10.1351/pac200375070975

43. Callahan, M. P.; Gengeliczki, Z.; de Vries, M. S. Anal. Chem. 2008, 80, 2199– 2203 DOI: 10.1021/ac7022469

44. Callahan, M. P.; Gengeliczki, Z.; Svadlenak, N.; Valdes, H.; Hobza, P.; de Vries, M. S. Phys. Chem. Chem. Phys. 2008, 10, 2819– 2826 DOI: 10.1039/b719874d

45. Ford, A.; Fedick, S. J. Field Archaeol. 1992, 19, 35– 49 DOI: 10.1179/009346992791549012

46. Summers, R. M.; Louie, T. M.; Yu, C. L.; Subramanian, M. Microbiology 2011, 157, 583– 592 DOI: 10.1099/mic.0.043612-0

II. Sub-Micron Proximal Probe Thermal Desorption and Laser Mass Spectrometry On Painting Cross-Sections

Shawn C. Owens [a], Jacob A. Berenbeim [a], Catherine Schmidt Patterson [b], Eoghan P. Dillon [c] and M. S. de Vries*[a]

[a]University of California Santa Barbara, Department of Chemistry and Biochemistry, Santa Barbara, CA, USA. E-mail: devries@chem.ucsb.edu; Fax: +1 805 893 4120; Tel: +1-805-893-4720

[b]Getty Conservation Institute, 1200 Getty Center Drive, Suite 700, Los Angeles, CA, USA. E-mail: cpatterson@getty.edu; Fax: +1 310 440 7711; Tel: +1 310 440 6232

[c]Anasys Instruments, 325 Chapala St, Santa Barbara, CA, USA. E-mail: eoghan@anasysinstruments.com; Fax: +1 805 730 3300; Tel: +1 805 730 3310

DOI: 10.1039/C4AY00919C (Paper) Anal. Methods, 2014, **6**, 8940-8945

Abstract

We demonstrate sub-micron, atomic force microscopy (AFM) proximal probe desorption of organic dyes, and subsequent detection via laser mass spectrometry. A nanothermal analysis (nano-TA) probe tip in contact with a surface is heated (10 000 °C s^{-1}) to induce thermal desorption, creating depression sizes ranging from 360–1500 nm in diameter and 20–100 nm in depth. Desorbed material is drawn through a heated capillary via vacuum, and deposits onto a graphite sample bar. Laser desorption, followed by supersonic jet-cooling and either resonant two-photon ionization (R2PI) or non-resonant ionization mass spectrometry is used to characterize the transferred material. Individual, microscopic layers of organic dyes within painting cross-sections were successfully analyzed using this new approach. Separating the AFM thermal desorption step from the detection step allows for the use of analytical techniques appropriate for individual samples of material, desorbed with high spatial resolution.

Introduction

The analysis of cultural heritage materials presents a number of challenges that limit the range of analytical techniques available for use, these obstacles include: limited and extremely small samples, complexity of sample structure, the importance of maintaining spatial integrity and, most notably, the rarity of the samples. These limitations present unique challenges for the identification of organic dyes, particularly in paintings that may have multiple paint layers due to the artist's technique as well as subsequently applied restoration layers. These materials are often examined by analysis of microscopic painting cross-sections in which complex mixtures and thin (often only a few microns) layers of organic material are commonly encountered. Elucidating the nature of these organic

compounds with high spatial resolution may help clarify aspects of a painting's history; and can assist in the painting's conservation since these molecules are often prone to degradation from moisture, light, or other environmental conditions. Therefore, there is a need for analytical techniques that can provide spatially resolved, molecularly-specific, and unambiguous identification of organic compounds in cultural heritage materials.

A number of analytical techniques have been used to identify the materials in painting cross-sections. A variety of spatially resolved spectroscopic and mass spectrometric techniques developed to identify elements and general functional groups are well established and extensively used in cultural heritage science,[1,2] but they are not optimized for detailed analysis of molecular composition. For example, secondary ion mass spectrometry (SIMS) can attain spatial resolutions on the order of 10–50 nm for elemental analysis, and has also been extended to some organic colorants as well.[3,4] Due to the inherent fragmentation of organics with SIMS, many organic pigments that have similar molecular weights or structures can be difficult to distinguish from each other. Scanning electron microscopy/energy dispersive X-ray spectroscopy (SEM-EDS) provides high spatial resolution, but being an elemental analysis technique it is better suited to the identification of inorganic species than organic components.[5] Micro X-ray fluorescence (μ-XRF) is a commonly used, often mobile, instrument capable of ~65–100 μm spatial resolutions,[6,7] but is also limited to elemental analysis. Molecular identification of organic molecules can be accomplished using spectroscopic techniques-such as a recent example combining laser ablation and surface-enhanced Raman spectroscopy (SERS)[8] but, relatively broad fluorescence signals masking organic bands in complex mixtures of natural organic dyes can often limit identification to broad classes of organic components. In addition, a spatial

resolution of ~10 μm limits its use in many paint cross-section applications. Raman microscopy and Raman mapping can also provide spatially resolved (~1–2 μm) molecularly specific identification, but still has difficulty to differentiate spectroscopically similar molecules that are common in organic colorants.[9,10] Fourier transform infrared spectroscopy (FTIR) microscopy can provide specific identification of both organic and inorganic compounds, and the continued development of attenuated total reflection (ATR) FTIR (~6 μm),[11] synchrotron-based FTIR (<1 μm),[12,13] and FTIR imaging techniques (~10–15 μm)[14,15] have begun to address the challenges of thin layers and the need for spatial specificity. Still, FTIR either lacks the spatial or spectroscopic resolution for organic containing cross-sections, or requires the use of synchrotron facilities. An additional possibility is a form of laser desorption mass spectrometry (LDMS) that avoids many problems associated with analyzing complex mixtures, and is a valuable tool in the identification of several organic pigments.[16] However, fragmentation caused by LDMS can complicate categorical identification of certain pigments in addition to being limited by a spatial resolution of ~2–4 μm.[17] Ultimately, none of these techniques maintain both high spatial resolution and high selectivity.

Recently, Berkel and coworkers reported nanometer scale atomic force microscopy (AFM) proximal probe thermal desorption (AFM-TD) (Anasys Instruments, Santa Barbara) of organic molecules, and subsequent detection via electrospray ionization mass spectrometry (ESI-MS).[18] Additionally, the Zenobi group developed an active plasma source allowing for ambient pressure ionization mass spectrometry on direct analysis of desorbed material.[19] We further extend this combination of AFM proximal probe AFM-TD and MS by decoupling the AFM step from the MS step. In our approach we collect sub-

micron size samples through AFM proximal probe AFM-TD, followed by separate analysis with resonant two photon ionization (R2PI) coupled with mass spectrometry. While ESI-MS is well suited for mass spectrometry of unknown compounds, R2PI can identify and selectively ionize specific molecules. So, when particular compounds can be targeted, R2PI is well suited for the complicated samples typically present in cultural heritage artifacts. We note that the inherent optical resolution in low temperature laser spectroscopy such as R2PI can often be much higher than the mass resolution in a typical mass spectrometer (MS).[20] We also employ non-resonant LDMS to demonstrate the flexibility created by decoupling AFM-TD and MS. Our approach consists of a two-step process: (1) sample collection, in which an AFM-mounted microscope is used to identify features, proximal probe AFM-TD is performed at selected locations and desorbed material is transferred to a sample bar through a capillary, and (2) sample analysis, in which the bar with desorbed material is transferred to the laser mass spectrometer for laser desorption of molecules, followed by jet cooling of the desorbed molecules, R2PI and finally detection in a time-of-flight MS. While normally the spatial resolution of laser desorption is limited by the laser spot size of approximately 1 μm,[17] the combination with the preceding AFM-TD sampling step makes it possible to reach a spatial resolution of ~0.5 μm.

Experimental

Solvents and chemicals

The dye alizarin crimson dark (Kremer Pigment 2361), and the synthetic organic pigments PV19 (Pigment Violet 19, Ciba) and PO43 (Pigment Orange 43, Clariant) were obtained from the Getty Conservation Institute's Reference Collection. Alizarin 97% pure was obtained from ACROS Organics. Binding media used for paint samples were egg yolk

for alizarin crimson, and multi-purpose white glue (Elmer's Glue) for the synthetic organic pigments. Egg yolks were taken from whole chicken eggs obtained indiscriminately from the grocery store. Technovit 2000 LC light curing resin (Heraeus Kulzer GmbH & Co. KG) was used for the preparation of painting cross-section samples. Caffeine (anhydrous) was obtained from Sigma Aldrich to prepare a sample to test the analytical method prior to cross-section analysis. HPLC grade methanol was obtained from Fischer Chemical.

Sample preparation

Two methods are employed to make samples; thin film deposition on a silica wafer and resin embedding of painting cross-sections. Using a home-built spin coater, a 0.3–0.5 mL aliquot of 0.02 M caffeine in methanol is deposited onto a silica substrate by a syringe and spun off at 5000 rpm for 1 s. To prepare samples from which a cross-section could be made, individual layers of paint (arbitrary thickness) are applied to a modern gesso-prepared board (Ampersand gesso board, acrylic gesso surface) and allowed to dry. Incisions are made using a scalpel in the dried paint to reveal and remove a piece of the painted surface in cross-section, before embedding in resin and curing under blue light. These samples are dry-polished iteratively by hand (Micro-Mesh, Micro Surface Finishing Products, Inc).

Instrumentation

The atomic force microscopy-thermal desorption (AFM-TD) experiments are carried out using an Anasys Instruments afm+®. The system allows for high spatial resolution nanothermal analysis (nanoTA), achieved by the use of Thermalever™ AFM probes. These probes are batch-fabricated silicon AFM probes with a resistive heater element integrated into the end of the cantilever, allowing for the controlled heating of the probe. Initial

nanoTA ramps were performed within each homogeneous sampling area to determine a voltage ramp profile, and to indicate the thermal transitions of the material being sampled. A maximum probe temperature defines the voltage ramp profile and is set to a corresponding bulk phase transition. The probe is ramped to the nanoTA maximum temperature at a rate of 10 000 °C s^{-1} and a typical maximum desorption temperature of 400 °C can be reached in tens of μs. The probe is calibrated by increasing the voltage to the probe while on the surface of three polymeric materials with known melting temperatures: PCL, PE and PET. At each material's melting point, the probe penetrates into the sample surface and the voltage value can then be converted to °C, as the melt temperatures of these polymers have been well characterized. For the samples analyzed, spot sampling time is determined by a ramp rate of 100 V s^{-1}, but is typically in the range of 25–50 ms. Material is repeatedly desorbed from the sample surface at a sequence of different spots within each sample or layer within a sample (Table 1).

Table 1 AFM-TD Sample Characteristics

Molecule	Molecular weights (g mol^{-1})	TD events	Crater diameter (nm)	Crater depth (nm)	Crater volume (nm^3)
Caffeine	194.19	55–85	360	20–200	6.8×10^5–6.8×10^6
Alizarin	240.21	15	750	700	1.0×10^8
PV19	312.32	10	750–1500	800–1000	1.2×10^8–5.9×10^8

Molecule	Molecular weights (g mol^{-1})	TD events	Crater diameter (nm)	Crater depth (nm)	Crater volume (nm^3)
PO43	412.41	10	800–1000	200–400	3.4×10^7–1.0×10^8

As shown in Fig. 1, the resulting desorption plume is drawn via vacuum through a stainless steel (SS) capillary, and into an isolated sample collection box, where it deposits onto a graphite sample bar. For caffeine sampling a SS 6″ × 0.05″ OD × 0.03″ ID capillary is pumped at a flow rate of ~150 mL s^{-1}. For pigments, a SS 6″ × 0.05″ OD × 0.033″ ID capillary is pumped at a flow rate of ~215 mL s^{-1}. The larger diameter capillary served to increase the flow rate. The capillary is heated to 90 °C to reduce condensation of the desorbed material during the transfer. The capillary is positioned approximately 200–500 μm from the AFM tip in order to maximize the amount of desorbed material drawn through the capillary and onto the graphite sample bar; limiting this distance avoids interference from mechanical vibrations caused by the continuous pumping of the sample collection box. Since the analysis step is separated from the analysis step, it is possible to optimize the sampling geometry and conditions for maximum collection. In real time direct inlet mass spectrometry, for example, this is harder to achieve because the flow rate affects the ionization efficiency. Numerous desorption spots from the same local area (e.g. paint layer) are deposited additively onto the graphite bar in order to maximize sample material transfer ensuring enough material for subsequent mass spectral analysis. The graphite bar can be translated allowing deposition of different spots across the bar. The entire sample collection box is on a 3-axis stage to give full movement for positioning the capillary nearest the AFM tip.

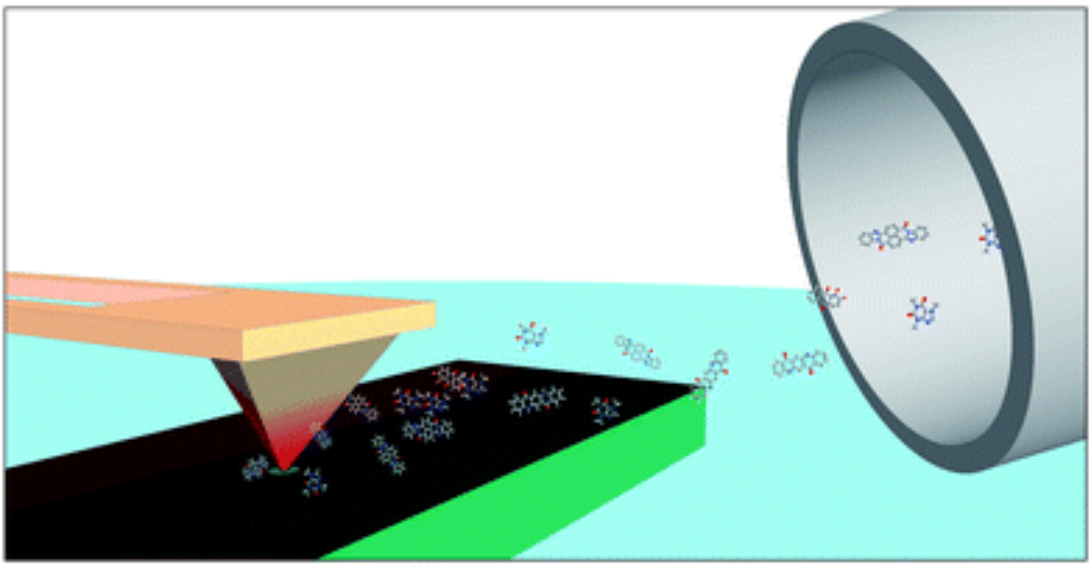

Fig. 1 Representation of AFM-TD process and resulting plume being drawn into the capillary.

The experimental setup for mass spectrometry has been described elsewhere.[20] The sample bar is loaded into a high vacuum chamber, where it is positioned directly in front of a pulsed nozzle. The sample bar can be translated for successive laser shots on different locations. Material is laser desorbed from the sample bar by light from a Continuum MiniLite 1064 nm Nd:YAG laser, which is attenuated to minimize fragmentation and focused to a slit approximately 1 × 5 mm, within 5 mm of the nozzle. The desorbed material is entrained in a pulsed supersonic argon stream controlled by an ACPV2 pulsed cantilever piezovalve[21] with an opening diameter of 300 μm and an concave conical shape with a full angle of 40°, at a backing pressure of 6 bar. The Ar molecular beam is skimmed before entering a source region where it is intersected by laser beam(s) and photo-ionized.

Two ionization techniques are employed: resonance enhanced two photon ionization (R2PI) and non-resonant ionization. R2PI uses a first photon from a Lumonics tunable dye

laser to resonantly excite a molecule to an electronic excited state, followed immediately by a second photon from either the same or a different dye laser which ionizes the molecule. We have previously reported the spectroscopy of caffeine,[11] which allows tuning the dye laser to a specific resonance in order to selectively ionize it and record the mass spectrum. The R2PI of caffeine was carried out with a set wavelength of 281.635 nm (1.1 mJ per pulse). Non-resonant ionization was carried out for all pigments using a 193 nm excimer laser (~4 mJ per pulse). All ions are characterized in a reflectron time-of-flight mass spectrometer. Typical mass resolution (m/Δm) is 700 or higher. The duty cycle of the experiment is 10 Hz.

Results and discussion

A topographic image was taken before and after each experiment to investigate the AFM-TD depression sizes as well as any other changes to the morphology of the sample. Table 1 lists the complete set of molecules that were successfully transferred and identified, along with the number of times the tip was heated to induce desorption (AFM-TD Events) for each sample, as well as desorption depression characteristics. Successful AFM-TD appeared to be dependent on the thermal characteristics of the binding medium, as opposed to the pigment within that binding medium.

To determine the viability of separate AFM-TD and mass spectrometric steps, caffeine served for initial experiments as we have previously reported laser desorption jet-cooling R2PI-MS of caffeine, and the R2PI spectroscopy of this molecule is well known.[22] Generally R2PI mass spectral analysis is only possible with prior knowledge of the R2PI spectrum for the jet-cooled molecule. Since the spectroscopic peaks are dependent on, and extremely sensitive to, structure this technique allows for indisputable identification of

molecules by simultaneous spectroscopic and fragment-free mass spectrometric characterization. Fig. 2a shows the R2PI spectrum of caffeine obtained by scanning the tunable excitation laser.[22] The photo-ionization step adds significantly to the molecular selectivity of the analysis, the strong absorption at 281.635 nm was used for R2PI-MS experiments.

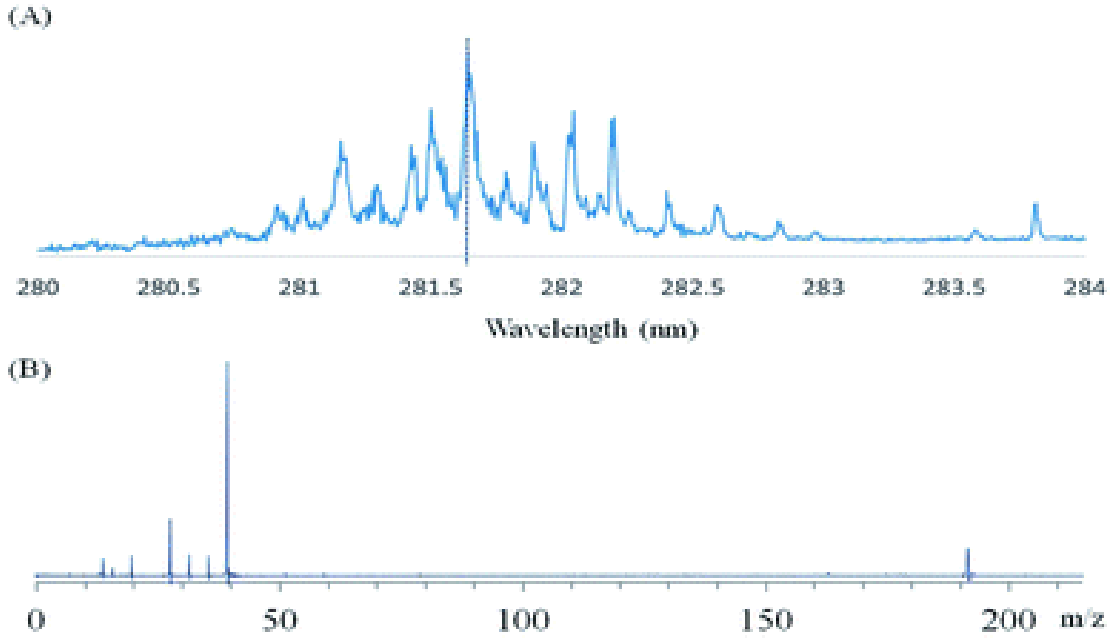

Fig. 2 (A) R2PI spectrum of caffeine, dashed line corresponds to 281.635 nm (B) R2PI mass spectrum of caffeine, parent peak located at m/z 194.19.

A number of AFM-TD events from a caffeine-coated silica wafer were transferred to a graphite sample bar as 3 separate spots (AFM-TD events on each spot: (1) 55 (2) 75 (3) 85). Fig. 2b illustrates the R2PI-MS corresponding to material from spot 1 on the sample bar. The parent peak of caffeine is seen at m/z 194, indicating a successful transfer of the sample following AFM-TD (Ar, the carrier gas, can be seen at m/z 40). Note the absence of unrelated peaks observed from either AFM-TD fragmentation or the laser desorption of the

graphite matrix, illustrating the highly selective nature of R2PI-MS. To verify caffeine was present in each spot on the sample bar, the signal of caffeine (i.e. the intensity at m/z 194.19) was monitored as the sample bar was translated, in order to laser desorb from each of the 3 spots. Fig. 3 shows a back and forth scan. After spot 3 was analyzed, the direction of the bar was reversed in order to laser desorb again from same spots 2 and 1. The signal spike seen in spot 3 is due to an increase in the bar speed reversing directions, exposing fresh sample at a faster rate and resulting in a slight signal increase. The rate was returned to a slower speed after the increased signal seen in spot 3.

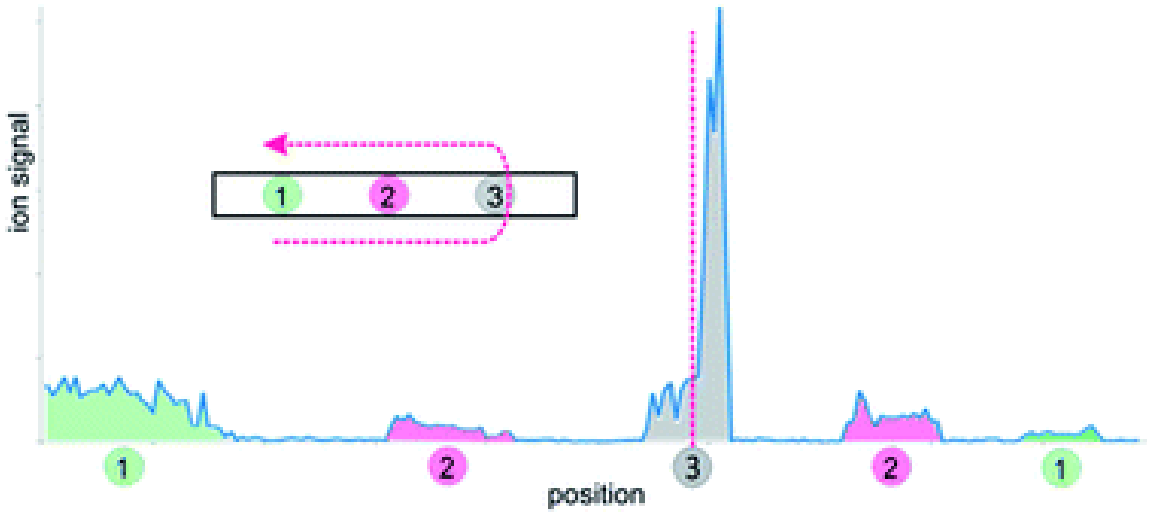

Fig. 3 Caffeine parent peak intensity monitored while translating sample bar back and forth over three spots in order 1-2-3-2-1. Colored peaks correspond to deposited spots on sample bar from AFM-TD. The red dashed-line represents the point at which the direction of the sample bar translation was reversed.

The fact that signal from spots 2 and 1 can be detected on the second pass demonstrates that complementary analytical techniques can be performed on the same sample spot more than once.

Following successful application to the well-characterized caffeine system, the AFM-TD technique was next applied to more challenging samples – a traditional organic colorant and modern synthetic pigments prepared as mounted cross-sections – in order to determine whether the overall approach is reasonable for samples of these types.

Fig. 4a shows a microscope image of a cross-section containing the traditional red organic colorant alizarin crimson. Following AFM-TD of the alizarin layer, we performed laser desorption mass spectrometry using a 193 nm excimer laser for ionization. The parent peak corresponding to the alizarin chromophore can be seen at m/z 240.21. Several other species also appear, indicative of the complex nature of these natural organic dyes. Analogous non-resonant laser ionization experiments with standard alizarin crimson dye (without the AFM-TD step) were performed to determine whether additional fragments were created in the AFM-TD heating step. The results indicated that though some additional fragmentation did occur, the vast majority of the mass peaks were identical. The limited additional fragmentation was likely due to thermal fragmentation during the relatively slow heating rate of the AFM-TD process. Nonetheless, in each case, intact molecules were successfully thermally desorbed, transferred, and detected in a mass spectrometer. As evident by the small size of the sampling depressions (750 nm diameter), several samples within even the thinnest paint layers could be obtained while maintaining the bulk of the cross-sections for further analytical work.

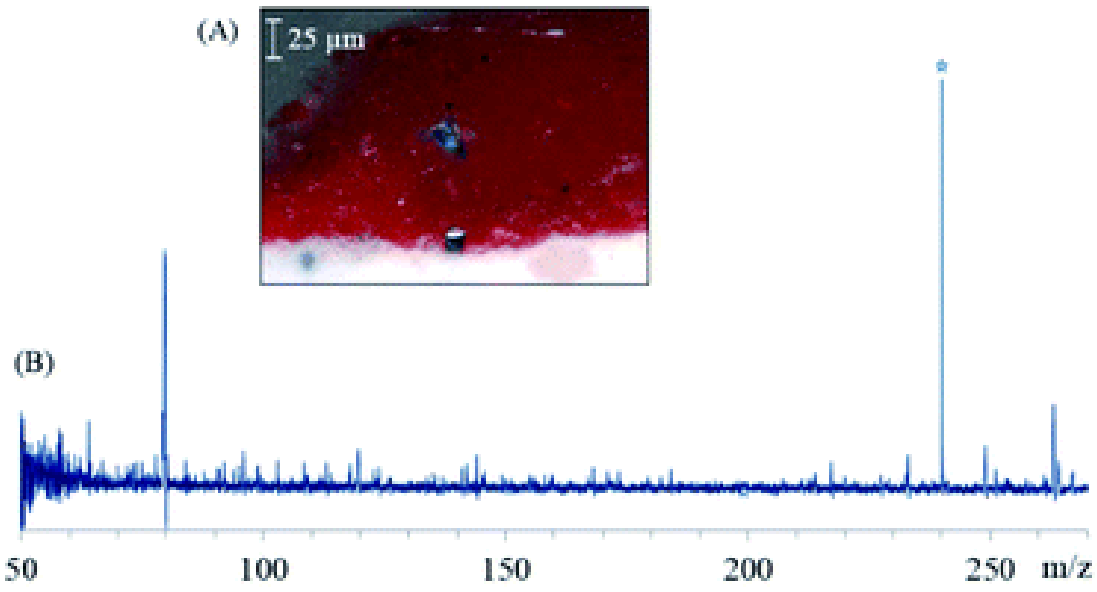

Fig. 4 (A) Microscope image of alizarin crimson dye layer, with white substrate below (B) non-resonant ionization mass spectrum from alizarin dye layer. Star denotes parent mass peak.

To complement work done on the natural organic dye, we performed additional experiments using modern synthetic pigments PV19 and PO43. Fig. 5a shows a microscope image of a cross-section consisting of a sequence of layers (from bottom to top: titanium white, PV19, PO43, PY151, PR254). Fig. 5b shows the mass spectrum produced from the layer of PV19, where the parent peak is visible at m/z 312.32. Fig. 5c shows the mass spectrum of the PO43 layer. The parent peak of PO43 can be seen at m/z 412.41. There was little indication of any fragmentation in the modern synthetic pigments, although it is worth noting these were pure standards. In contrast, traditional colorants such as alizarin crimson are complex mixtures of molecules because they are often obtained through plant and animal matter, and consequently have complex spectra. Desorption depression sizes in the modern synthetics ranged from 750–2500 µm, likely due to melting of the paint medium (Elmer's Glue) by the radiant heat from the probe tip. There was no indication of any PV19

desorption or detection in the PO43 layer, nor vice versa, demonstrating the absence of cross contamination and confirming the high spatial resolution.

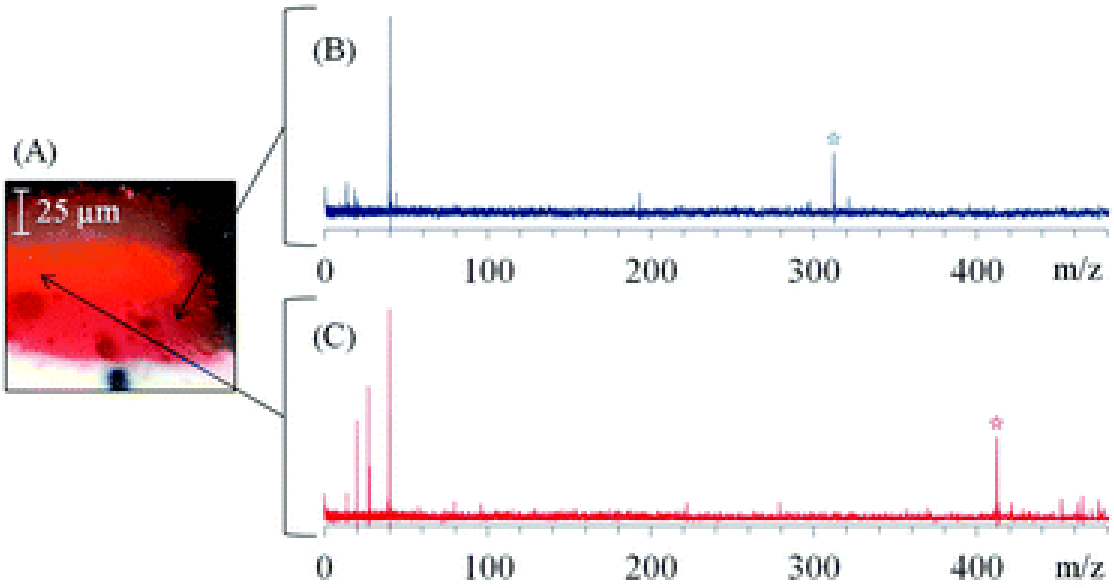

Fig. 5 (A) Microscope image of synthetic dye cross section. The sequence of layers from bottom to top: PV19, PO43, PY151 and PR254. (B) Mass spectrum (non-resonant) obtained from PV19 dye layer and (C) non-resonant ionization mass spectrum (non-resonant) from PO43 dye layer. Stars denotes parent mass peaks.

Conclusions

We have demonstrated a new approach for coupling proximal probe AFM-TD and subsequent chemical analysis in separate steps. This approach allows the use of a diverse set of techniques adapted to the characteristics of each individual sample on a case by case basis. By using R2PI mass spectrometry for the separate analysis step, this new sample collection method provides a format for unambiguously identifying specific organic colorants. This approach should be particularly well-suited for samples in which the spatial

resolution of other available analytical techniques is insufficient to probe, such as thin layers or small inclusions of an unknown organic material. Further work is needed to catalogue the response of different target compounds of interest in the sampling step as well as their spectra for R2PI analysis. Forthcoming work will be extended to identify different binding media, including oil, gum, varnishes and more complex mixtures of organic and inorganic pigments, as these are more representative of authentic cultural heritage artifacts. This method can also be extended to other fields of research which face similar challenges in spatially resolved organic analysis.

Acknowledgements

The authors thank Dr Karen Trentelman and Alan Phenix for their exceptional contributions to this work. We are also grateful to Kevin Kjoller, Roshan Shetty and Anasys Instruments for the generous donation of their time and research facilities. This material is based upon work supported by the National Science Foundation under CHE 1301305 and CHE 1018804.

Notes and references

1. G. Spoto, A. Torrisi and A. Contino, Chem. Soc. Rev., 2000, 29, 429–439.
2. G. Spoto and G. Grasso, TrAC, Trends Anal. Chem., 2011, 30, 856–863.
3. A. Adriaens and M. G. Dowsett, Appl. Surf. Sci., 2006, 252, 7096–7101.
4. C. S. Deroo and R. A. Armitage, Anal. Chem., 2011, 83, 6924–6928.
5. C. Genestar and C. Pons, Anal. Bioanal. Chem., 2005, 382, 269–274.
6. G. Vittiglio, S. Bichlmeier, P. Klinger, J. Heckel, W. Fuzhong, L. Vincze, K. Janssens, P. Engström, A. Rindby, K. Dietrich, D. Jembrih-Simbürger, M. Schreiner, D. Denis, A. Lakdar and A. Lamotte, Nucl. Instrum. Methods Phys. Res., Sect. B, 2004, 213, 693–698.

7. K. Trentelman, M. Bouchard, M. Ganio, C. Namowicz, C. Schmidt and M. Walton, X-Ray Spectrom., 2010, 159–166.

8. P. S. Londero, J. R. Lombardi and M. Leona, Anal. Chem., 2013, 85, 5463–5467.

9. G. Paternoster, R. Rinzivillo, F. Nunziata, E. M. Castellucci, C. Lofrumento, A. Zoppi, A. C. Felici, G. Fronterotta, C. Nicolais, M. Piacentini, S. Sciuti and M. Vendittelli, J. Cult. Herit., 2005, 6, 21–28.

10. P. Vandenabeele, B. Wehling, L. Moens, H. Edwards, M. De Reu and G. Van Hooydonk, Anal. Chim. Acta, 2000, 407, 261–274.

11. S. Prati, E. Joseph, G. Sciutto and R. Mazzeo, Acc. Chem. Res., 2010, 43, 792–801.

12. G. D. Smith, J. Am. Inst. Conserv., 2003, 42, 399–406.

13. J. Mass, J. Sedlmair, C. S. Patterson, D. Carson, B. Buckley and C. Hirschmugl, Analyst, 2013, 138, 6032–6043.

14. E. Joseph, S. Prati, G. Sciutto, M. Ioele, P. Santopadre and R. Mazzeo, Anal. Bioanal. Chem., 2010, 396, 899–910.

15. E. Joseph, C. Ricci, S. G. Kazarian, R. Mazzeo, S. Prati and M. Ioele, Vib. Spectrosc., 2010, 53, 274–278.

16. D. P. Kirby, N. Khandekar, K. Sutherland and B. A. Price, Int. J. Mass Spectrom., 2009, 284, 115–122.

17. L. I. Grace, A. Abo-Riziq and M. S. deVries, J. Am. Soc. Mass Spectrom., 2005, 16, 437–440.

18. O. S. Ovchinnikova, M. P. Nikiforov, J. A. Bradshaw, S. Jesse and G. J. Van Berkel, ACS Nano, 2011, 5, 5526–5531.

19. M. M. Nudnova, L. Zhu and R. Zenobi, Rapid Commun. Mass Spectrom., 2012, 26, 1447–1452.

20. G. Meijer, M. S. Devries, H. E. Hunziker and H. R. Wendt, Appl. Phys. B: Photophys. Laser Chem., 1990, 51, 395–403.

21. D. Irimia, D. Dobrikov, R. Kortekaas, H. Voet, D. A. van den Ende, W. A. Groen and M. H. M. Janssen, Rev. Sci. Instrum., 2009, 80.

22. M. P. Callahan, Z. Gengeliczki, N. Svadlenak, H. Valdes, P. Hobza and M. S. de Vries, Phys. Chem. Chem. Phys., 2008, 10, 2819–2826.

Appendix

I. Picosecond System Notes ps Pump Laser and ps OPG laser

PL2251A – PS Pump Laser

1) Low Power: This could be any number of the below items. If E1 is < 100% then see the regenerative amplifier. If 355 nm pulse energy is below 8.5 mJ at 40% amplification see SHG and THG conversion. Otherwise check flash lamps and flash lamp voltage. Make small changes during any adjustments and before pumping on the OPG check divergence. Check for divergence and convergence by comparing burn spots (1 shot, 100% amplifier) both directly in front of the laser and ~5 meters away. If the beam is converging absolutely do not send it into the OPG.

2) Regenerative Amplifier: When the power is low, as read by E1 (100% = 900 uJ), adjust with mirrors M8 and M9. Begin by checking seed vs regen overlap in the near and far field (using sensitive IR card), which is good confirmation of M1/M2 alignment.

*__Before__ adjusting any alignment screws check by lightly pushing mirror mount M9 in all directions and watch for power improvements

It may also be necessary to increase the current on the regenerative amplifier pump diode. This requires ADVANCED permission access in CAN browser. Turn up the current (under LDMA150A) slowly. As you go up in small ~1% steps, check the energy to see if it also increases. If after say a 5% increase the energy has not gone up, go back to the original value and contact EKSPLA or ALTOS.

*The factory sets the current at a factor of 2 below the maximum limit of the diode. Approaching this limit can cause the diode to fail, i.e. melt. More than 20% above factory settings is unknown territory.

Afterwards, you may need to slightly adjust M3 or M4 to restore amplifier beam profile, but likely no adjustment will be needed.

3) SHG and THG conversion: Best optimization of THG is when the 532 is slightly detuned. Turn amplifier to 30% to find global maximum rotation angle, this low power will minimize signal from any local maximum.

<u>*Only</u> adjust SHG crystal in the horizontal direction and THG crystal in the vertical. See the manual for explanation.

4) Changing Flash Lamp: See updated manual on next page. Flash lamps are recommended to last 15 to 25 million shots. It is normal to have to adjust the flash lamp voltage slowly as the lamps age to compensate for breakdown of the metallic components.

1. Water lines unscrew with CW rotation and are finger tight, tools shouldn't be necessary. Also, the water will drain quickly back down the lines. Dab dry with paper towel to prevent moisture getting on nearby optics.

2. The chamber must be lifted straight up taking care that remaining water inside does not get on Nd:YAG rod. Carefully empty the water into the sink.

3. Loosen screws on the flash lamp pressure plates but don't remove them. This should relieve enough tension on the pressure washers to exchange the new lamps.

4. The initial flash lamp voltage should be set at 1470 V on the power supply. Use the wheel to scroll and pushing in the wheel in for making selections. New lamps actually have a “burn-in” period at the beginning where the required voltage may change quickly. After that, though, it’s a gradual adjustment. Burn-in is about 1.5 million shots. Be sure to increase slowly and check for divergence or convergence of the output beam profile.

5) Power Stability: Instability out of the pump laser is ~1% or less. Check manual. Using the energy meter, record 200 shots of 355 nm 40% amplification (8.5 mJ) 1 shot average on the meter and 1 shot per point in LabView. Instability is best calculated as (Standard Deviation / Root Mean Square) x 100 and best checked over 10, 20, 50, 100, 200 shots. Lower stability seems to be caused by poor aligment through the power amplifier but mainly stability increases as the power amplifier increases.

6) Beam profile: Using the photographic burn paper, determine whether the beam is misaligned through the power amplifier. Asymmetric contrast of the concentric ring profiles can be fixed by adjusting mirror M3/M4. Left is left, etc. Be sure to make very small changes to the adjustment screws and record a new singlae-shot burn mark for comparison after each iterative change.

7) Ext trigger: TTL pulse, high-Z, pulse width >17.5 us, 4.5 V. Time between ps sync out and optical pulse ~ 609 us.

CAN Browser

The CAN browser password is not in the manual – it is given out as-needed for "qualified" customers. (Congratulations – you've been deemed "qualified"!)

password for CAN Browser: lIhh67o

[lima Indigo hotel hotel six seven oscar], case sensitive.

When the password is entered, don't change any settings you don't understand, and change back to the lower security level when done so other users don't accidentally change critical settings.

PG-401 SH – PS OPG Laser:

1) Low Power – EM1 may be miscalibrated to high bias limiting pump power, see below. Most likely the pump beam needs realignment into the OPG and this is done by the outer two 355 nm dichroic mirrors between Pump and OPG lasers. Use the energy meter in front of the OPG, setting the meter to single shot and plotted live with LabView through the GPIB. Make small horizontal changes to both mirrors until power has been maximized with OPG at 532.1 nm. Vertical alignment shouldn't be necessary.

2) Power Instability - EM1 may be miscalibrated to high bias causing low pump power which causes higher instability, see below. Pump with at least 8 mJ. Check that beam profile of the pump laser is optimal.

3) EM1 Miscalibrated – EM1 is a photodiode with a series of six filters; 1. black filter – 2. metal mesh – 3. black filter – 4. neutral density filter – 6. neutral density filter (the last being nearest the Si diode). These filters attenuate the photo induced response down to some appropriate range to monitor the pump power within a calibration factor defined by PGSoft, this factor is between 1 and 2. Check the pump power in front of the OPG entrance mirrors with a 355 nm dichroic and compare this value to what the controller says.

If the EM1 value doesn't closely match the energy meter begin by attempting to recalibrate the sensor with PGSoft. When connected you must choose Adjustment -> Calibration of sensors -> OPG sensor or similar and then choose According to real energy. Measure how much you get in front of PG unit and enter that value. After that you will need to Program controller. Close the input shutter, because you will be asked to restart PG after that, so motors will move and beam could hit the mounts.

The range in PGSoft is limited though and you may need to modify the filters.

For high bias:

- Small high bias can be fixed by arranging the position of each NDF further away from the Si diode, increasing the effect of scattering light away from the sensor.

- Large high bias, additional filtering is required. Teflon tape can be used very close to the Si diode. Also, additional metal mesh screens can be placed in the original order. Rotation between two screens should modulate the transmitted light. Buy the mesh at a hardware store and rinse with hexane to remove any oils.

For low bias: Remove previously added or original filters.

***Be mindful** of low bias and test at low pump powers. The OPG will become damaged if pump pulse energy is > 10mJ.

4) Beam walk: This is reference to any change in beam spot position with respect to wavelength as seen in the horizontal direction. Open UniPG PgSoftw.exe as administrator. Connect and then right click PG_CAN and “get program from controller”. Make corrections to PB (pellin broca) calibration factors or add new ones. The fewer the factors the better. When done, write program to save these new factors. Close the shutter between the pump and OPG lasers before allowing the controller to restart in order to prevent damage to optics.

5) OPG Pulse energy is low due to misalignment, e.g. the PG stage is aligned while the amplifier stage is misaligned. ****Read the Ultimate Guide Supplement for the OPG.** This becomes obvious when using the 50 mm beam guide on the beam traversing the PG stage verse what is split in the beginning to pump the amp stage. Take off the side cover (on the beam machine 2 side, or left side in direction of the exiting beam). Put a 355 dichroic on a small stand between M1 and M8 (recommend using a small ziptie around the dichroic to avoid a large optic mount, clip the tie and thread it into a low profile post mount). From here you can see whether the two stage beams are divergent in the verticle/horizontal directions. Make small adjustment on BS1 until beams match in vertical direction and check output power. Note: Prior to adjusting beams splitter, use external M1 to match retroreflective spot and that the PG goes through the pinhole after the grating.

II. Desorption laser (M.L.) Cavity Alignment Notes

Symptoms: The M.L. had been developing two ghost spots, like the sketch below, and a small damage on the output coupler (OC). Significant drop in pulse energy.

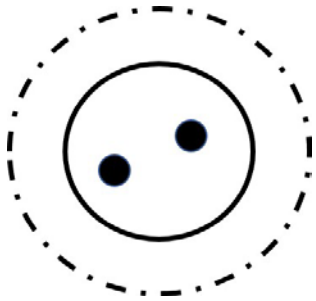

Figure 1 Ghost spots visible in burn images

Alignment Procedure:

1) Helium neon (HeNe) laser through the back of the laser [see Figure 2]
2) Remove Q-Switch (QS). Place card behind rear mirror and align HeNe to steer R1 onto P1, using P1 and P2 as near field and far field adjust R1 through pinholes 1 and 2. *Pin holes further back the better (> 3-4 m)
3) When HeNe is aligned onto rear mirror check retroreflections from NDYAG rod off of polarizer (retro 2a.2b). If not aligned on these reflections (near) and HeNe in far field, pay close attention to spot quality and differences, especially in ring patterns.
    a. Realign rear mirror retroreflection to center of pinhole
    b. Realign OC retroreflection to center of pinhole
4) Turn on laser (blocking HeNe) and tweak O.C alignment until lasing on IR card, then into power meter, should approach 50 mJ. *This is in long pulse mode because PC is out.
5) Put PC back in and tweak PC alignment (where screws are tightest is near proper alignment). Pulse power should reach ~15 mJ)
6) Now tweak OC and power should approach nominal ~40 mJ.
7) Check pulse on photodiode response, should be one pulse

8) Check burn spot for ‘hot’ spots (bad) and ‘cold’ spots (harmless)

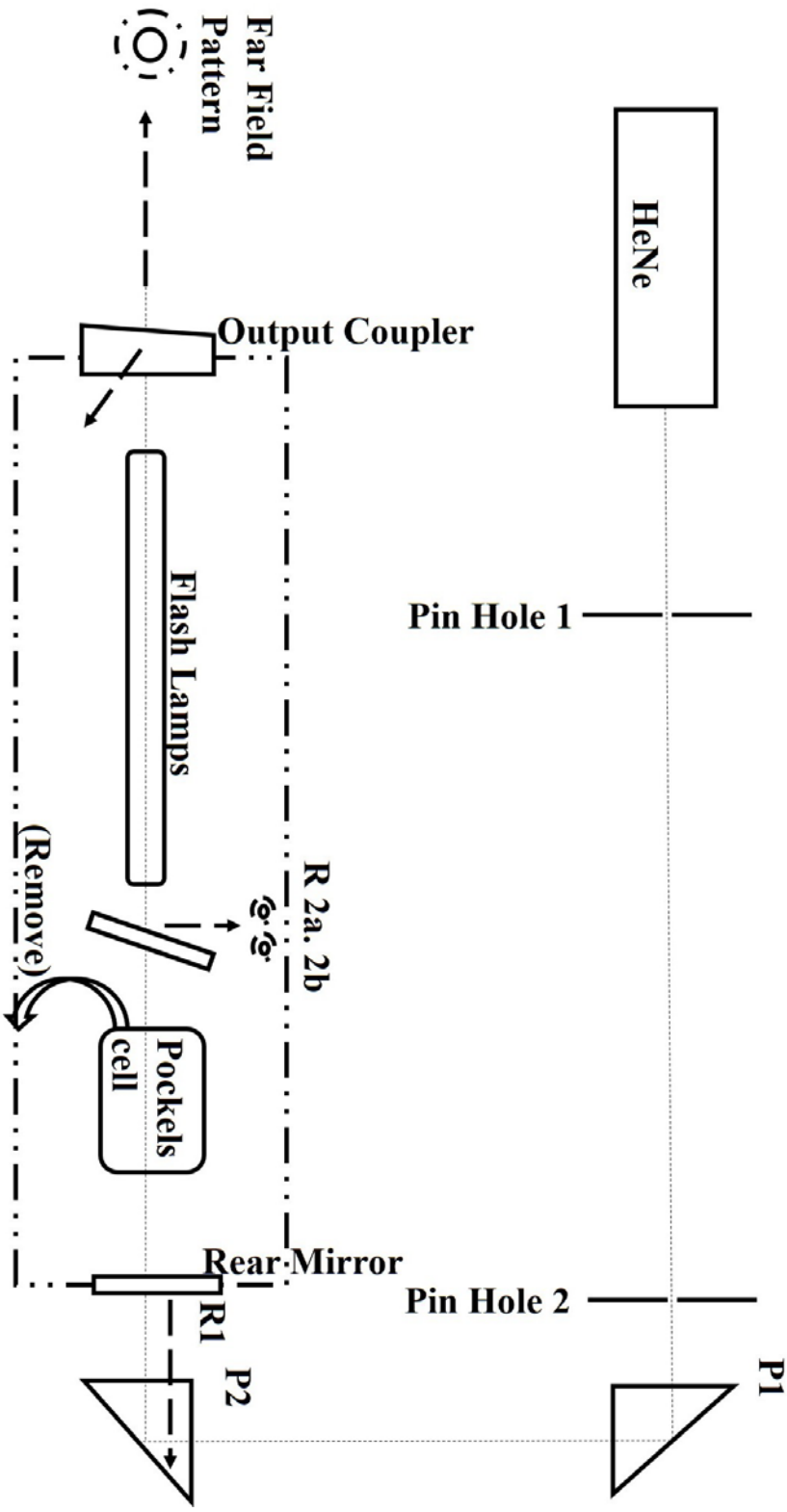

Figure 2 HeNe and External Optics and ML laser Cavity (Dotted Box).

III. Main Instrument Optical Setup for 1C-R2PI, 2C-R2PI, IR-UV, and UV-UV

Figure 1 below is the general optics setup for most R2PI and double resonant experiments. Notes:

1) Due to the jitter with the excimer, I've shown the location of photo-diode 1 (PD1) which ought to be used as T_0 for any experiments to reduce mass peak drift. The use of $PD2_{a/b}$ is for R2PI (not pump-probe) experiments to plot on an auxiliary scope the response of the excitation laser with respect to PD1. Do this after temporal overlap and if the signal ever drifts during an experiment you know the excimer has drifted and to restart the scan after redoing time overlap. Run the excimer at full power using pin-hole five (PH5) to control beam shape and attenuate when non-resonant signal is a problem, typically UV active molecules not VIS active.
2) Alignment of the excimer is best by P2 on in the near field on the TOF entrance guide, and by M_{193} in the far field according to Figure 2 (centering the beam in the "hat" projection. The project is due to the electrode stack within the ion source.

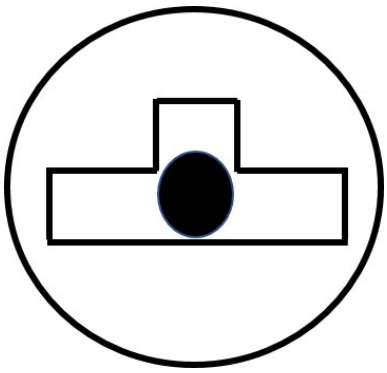

Figure 2 Excimer beam centered on projected source image, easily viewable on card.

3) For ns R2PI with 193/158 nm as the second color you can use either optical path from the ps table or ns table, collineated or opposing. The first is much easier to align with M1b and M2b. The second should be done with a reduction of beam size with PH2 and overlap mainly of the excimer onto the excitation beam, not necessarily strait through the source due to dependence on max IR signal.
4) PH1 - 3 are for initial alignment of the IR OPO/OPG beam and then overlap with the ps or ns trees. This way realignment of the IR is minimized while allowing for flexibility to run any number of ps or ns R2PI experiments in the meantime.
5) Alignment of the IR is best done first with the IR lens stage removed, using the top of the IR tree for near field and the bottom for far field, first PH1 as near and PH2 as far, and then PH1 or 2 as near and PH3 as far. Then install the IR lens stage and use is to align to PH3 and the top mirror of the IR tree on PH1 or 2.

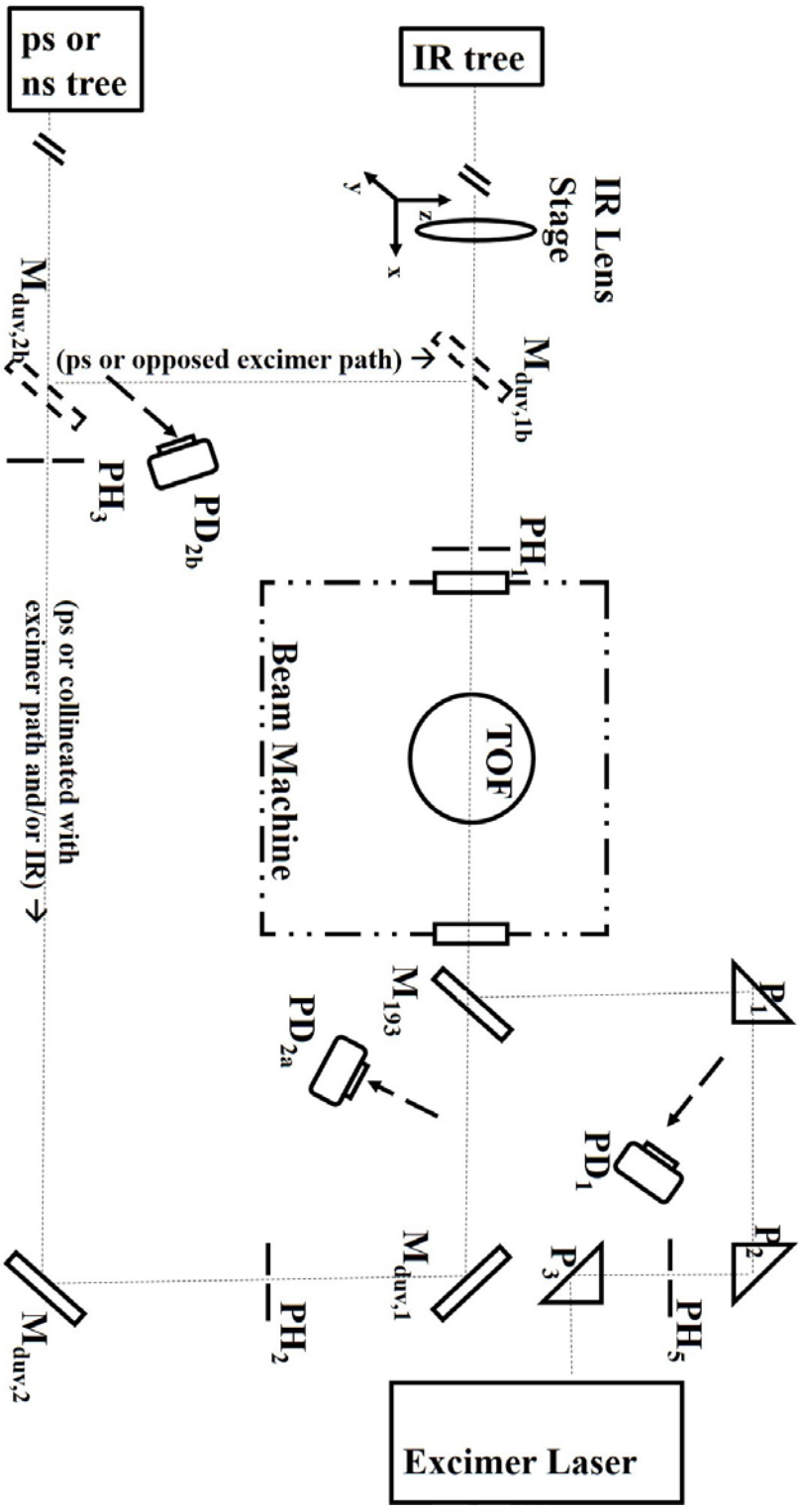

Figure 1 General optics setup for most R2PI and double resonant experiments including PD positions for triggering off jittering excimer pulse.

IV. Picosecond Optical Setup Emphasizing the Harmonic Generation and Time Delay Stage